

$\text{Al}_x\text{In}_{1-x}\text{As}_y\text{Sb}_{1-y}$ Digital Alloy Avalanche Photodiodes for Low-Noise Applications

A Dissertation

Presented to
the faculty of the School of Engineering and Applied Science
University of Virginia

in partial fulfillment
of the requirements for the degree

Doctor of Philosophy

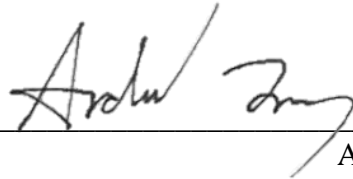
by

Andrew H. Jones

May 2020

APPROVAL SHEET

This dissertation
is submitted in partial fulfillment of the requirements
for the degree of
Doctor of Philosophy

Author Signature:  _____
Andrew H. Jones

This dissertation has been read and approved by the examining committee:

Advisor: Dr. Joe C. Campbell

Committee Member: Dr. Andreas Beling

Committee Member: Dr. Art W. Lichtenberger

Committee Member: Dr. Kyusang Lee

Committee Member: Dr. Olivier Pfister

Accepted for the School of Engineering and Applied Science:



Craig H. Benson, School of Engineering and Applied Science

May 2020

Copyright © by
Andrew H. Jones
All rights reserved
May 2020

To my mother who taught me to read

To my father who taught me to work

To my wife who taught me to dream

Acknowledgements

I would like to express my immense thanks for the leadership and support of my advisor Joe C. Campbell during my graduate work. From his first extension of a graduate research position to me until now, I have been continuously impressed with his kindness, generosity, and patience. I hope to take Professor Campbell's passion for his research with me for the rest of my career.

I would like to thank my committee for their time and support, as well as their teaching moments in the clean room, the classroom, and elsewhere.

I would like to thank our collaborators at the University of Texas at Austin, without whom I would have been unable to complete this research. Specifically, I would like to thank Stephen March for his hard work in growing the majority of my sample wafers, for his excellent communication, and for his perseverance through discouraging results and broken equipment.

I would like to thank my research group for their companionship and support, namely in practicing for presentations and answering difficult (or simplistic) questions.

I would like to thank the individuals who have maintained the clean room at UVA, specifically Mike Stogoski, Alex Lobo, and Joe Beatrice. Their commitment to the maintenance and repair of the equipment there enabled me to continue fabrication and processing in a timely manner.

Lastly, I would like to thank my family for their support, principally my wife Katie, who stuck with me through many late night absences, inexplicable bad moods, and regular distractions. Her loving support was indispensable in my ability to pursue this degree.

Abstract

Avalanche photodiodes (APDs) are used in a wide variety of light-detecting applications due to their internal gain mechanism. Compared to traditional photodiodes, APDs can achieve higher optical sensitivity by multiplying the photogenerated electrical carriers. APDs achieve this multiplication gain through impact ionization, wherein high energy carriers collide with surrounding electrons in the crystalline lattice and set them free. While advantageous for sensitivity, the stochasticity of the impact ionization process introduces additional electronic noise to the system. Reducing this noise, therefore, is paramount in high-performance APD design.

Together with the University of Texas at Austin, I further investigated the characteristics of APDs in the $\text{Al}_x\text{In}_{1-x}\text{As}_y\text{Sb}_{1-y}$ materials system and developed several new APD architectures which take advantage of its qualities. My work began by characterizing the temperature stability of simple PIN $\text{Al}_x\text{In}_{1-x}\text{As}_y\text{Sb}_{1-y}$ homojunction APDs. After demonstrating extraordinarily high temperature stability, I worked in characterizing wide-bandgap $\text{Al}_{0.8}\text{In}_{0.2}\text{As}_y\text{Sb}_{1-y}$ APDs and further improving fabrication processing techniques for the $\text{Al}_x\text{In}_{1-x}\text{As}_y\text{Sb}_{1-y}$ materials system.

My proposed thesis projects were twofold. First was designing and demonstrating a separate absorption, charge, and multiplication (SACM) APD for 2- μm applications. To create an effective design and layer structure for this project, I needed to perform numerous band structure and electric-field simulations. I created an $\text{Al}_x\text{In}_{1-x}\text{As}_y\text{Sb}_{1-y}$ material macro in APSYS Crosslight which I was able to tune to the required bandgaps for this project. After successful simulation, the designed layer structure was grown at the University of Texas at Austin and fabricated and tested at the University of Virginia. I successfully demonstrated a low-noise,

temperature-stable SACM APD for 2- μm applications with comparable dark current densities to state-of-the-art HgCdTe APDs while operating at temperatures 75 to 95 K higher.

My second project was demonstrating multiple-step staircase APDs. Although the first operational 1-step staircase APD had been previously demonstrated in the $\text{Al}_x\text{In}_{1-x}\text{As}_y\text{Sb}_{1-y}$ materials system, increasing the number of steps and therefore the gain was necessary to prove the viability of the staircase APD. While the University of Texas at Austin led the design and crystal growth of these devices, I successfully fabricated and characterized both 2-step and 3-step staircase APDs at the University of Virginia. Furthermore, through investigation into the relative noise power of these devices, promising new noise characteristics were identified.

Table of Contents

Acknowledgements	i
Abstract	ii
List of Figures	vi
1 Introduction	1
1.1 Motivation	1
1.2 APD Noise	3
1.3 Dark Current and Gain	8
1.4 Quantum Efficiency	10
1.5 Bandwidth	12
1.6 Material Growth and Fabrication	16
1.7 Thesis Organization	19
2 $\text{Al}_x\text{In}_{1-x}\text{As}_y\text{Sb}_{1-y}$ Temperature Stability	21
3 $\text{Al}_{0.8}\text{In}_{0.2}\text{As}_y\text{Sb}_{1-y}$ APDs	24
4 $\text{Al}_x\text{In}_{1-x}\text{As}_y\text{Sb}_{1-y}$ SACM APDs for 2- μm Detection	31
4.1 Device Design	33
4.2 Device Characterization	36
5 $\text{Al}_x\text{In}_{1-x}\text{As}_y\text{Sb}_{1-y}$ Staircase APDs	43
5.1 Multi-Step Staircase APDs	45
5.2 Improved Dark Current	51
5.3 Staircase APD Noise	54
6 Future Work	61
6.1 $\text{Al}_x\text{In}_{1-x}\text{As}_y\text{Sb}_{1-y}$ MWIR SACM APDs	61
6.2 $\text{Al}_x\text{In}_{1-x}\text{As}_y\text{Sb}_{1-y}$ nBn Detectors	63
6.3 Improved $\text{Al}_x\text{In}_{1-x}\text{As}_y\text{Sb}_{1-y}$ Staircase APDs	64
6.4 Extended Staircase APDs	64
Publications	67
Journals	67
Conferences & Abstracts	68
Works Cited	70
Appendix 1: Crosslight Code	81

1.1	$\text{Al}_x\text{In}_{1-x}\text{As}_y\text{Sb}_{1-y}$ Material Macro	81
1.2	$\text{Al}_x\text{In}_{1-x}\text{As}_y\text{Sb}_{1-y}$ Material Macro Parameters	84
1.3	$\text{Al}_x\text{In}_{1-x}\text{As}_y\text{Sb}_{1-y}$ 2- μm 30-50-70 SACM .layer File	85
1.4	$\text{Al}_x\text{In}_{1-x}\text{As}_y\text{Sb}_{1-y}$ 2- μm Graded SACM .layer File	86
Appendix 2: Fabrication Recipes		87
2.1	Photolithography	87
2.1.1	HMDS	87
2.1.2	AZ5214 Positive Photoresist	87
2.1.3	nLoR 2020 Negative Photoresist	87
2.1.4	AZ4330 Positive Photoresist	87
2.1.5	Lift-off Resist (LOR) 10B	88
2.1.6	SU-8 2000.5	88
2.2	Etching	88
2.2.1	Hydrochloric Acid - HCl	88
2.2.2	Phosphoric Acid - H_3PO_4	89
2.2.3	Sulfuric Acid - H_2SO_4	89
2.2.4	Citric Acid - $\text{C}_6\text{H}_8\text{O}_7$	89
2.2.5	Bromine - Br	90
2.2.6	Developer	90
2.2.7	Reactive Ion Etching with Inductively Coupled Plasma - RIE/ICP	90
2.3	Passivation	91
2.4	Contacts	92
Appendix Works Cited		94

List of Figures

Figure 1-1. Comparison of a PIN photodiode ($M = 1$) to APDs with various k factors.	2
Figure 1-2. Illustration of impact ionization for $k = 1$ (a) and $k = 0$ (b) for single electron injection.....	4
Figure 1-3. k factor for various materials systems.....	5
Figure 1-4: Block diagram of noise measurement setup.	8
Figure 1-5: Typical APD I-V curve.	10
Figure 1-6. Block diagram of EQE setup.....	12
Figure 1-7: Bandwidth as a function of gain for varying k values. ¹³ Here k is denoted by (β/α) . 15	
Figure 1-8: TEM cross section of $\text{Al}_x\text{In}_{1-x}\text{As}_y\text{Sb}_{1-y}$. ³⁵	16
Figure 1-9: EQE of $\text{Al}_x\text{In}_{1-x}\text{As}_y\text{Sb}_{1-y}$ APDs ($x = 0.3-0.7$). ³⁸	17
Figure 1-10: Cutoff wavelength and bandgap energy as a function of Al fraction.	18
Figure 1-11: Fabrication process flow.	19
Figure 2-1: Breakdown voltage as a function of temperature for the indicated $\text{Al}_x\text{In}_{1-x}\text{As}_y\text{Sb}_{1-y}$ devices.....	22
Figure 2-2: $\Delta V_{\text{bd}}/\Delta T$ for PIN APDs as a function of multiplication layer thickness.....	23
Figure 3-1: Excess noise as a function of gain for an $\text{Al}_{0.8}\text{In}_{0.2}\text{As}_y\text{Sb}_{1-y}$ APD. ⁴⁷	25
Figure 3-2: I-V characteristic of an improved $\text{Al}_{0.8}\text{In}_{0.2}\text{As}_y\text{Sb}_{1-y}$ APD. ³⁷	26
Figure 3-3: Absorption coefficient of $\text{Al}_{0.8}\text{In}_{0.2}\text{As}_y\text{Sb}_{1-y}$, ³⁷ $\text{Al}_{0.7}\text{In}_{0.3}\text{As}_y\text{Sb}_{1-y}$, ⁴⁸ and silicon. ⁴⁹	27
Figure 3-4: Measured gain curves under different illumination with fitted values from the impact ionization coefficients.	28
Figure 3-5: Calculated impact ionization coefficients of $\text{Al}_{0.8}\text{In}_{0.2}\text{As}_y\text{Sb}_{1-y}$ and $\text{Al}_{0.7}\text{In}_{0.3}\text{As}_y\text{Sb}_{1-y}$	29
Figure 3-6: Calculated receiver sensitivity at 10 Gb/s and 25 Gb/s.	30
Figure 4-1: Cross section and electric field profile of an SACM APD.	32
Figure 4-2: Epitaxial layer design of the $\text{Al}_x\text{In}_{1-x}\text{As}_y\text{Sb}_{1-y}$ 2- μm SACM APDs.	34
Figure 4-3: $\text{Al}_x\text{In}_{1-x}\text{As}_y\text{Sb}_{1-y}$ SACM APD energy band diagrams illustrating how the conduction band barrier is lowered with applied bias.	35

Figure 4-4: Changes in the conduction band of device A with increased reverse bias. A small barrier is present as carriers drift into the multiplication layer.	36
Figure 4-5: C-V curves for both 2- μm SACM APDs measured from 150- μm -diameter devices.	37
Figure 4-6: EQE of both 2- μm SACM APDs without AR enhancement measured from 200- μm -diameter devices.	38
Figure 4-7: I-V and gain curves for device A and B measured from 80- μm -diameter devices at room temperature under 2- μm illumination.	39
Figure 4-8: Dark current as a function of device diameter for each device at 10 V (left) and 35 V (right) reverse bias. Measurements are at room temperature. Linear fits are shown, indicating that surface leakage dominates.	39
Figure 4-9: Excess noise of device A and B measured at room temperature under 2- μm illumination.	40
Figure 4-10: Dark current density of device A and B as a function of temperature. That of state-of-the-art HgCdTe APDs is also included. ⁷⁹	41
Figure 4-11: $\Delta V_{\text{bd}}/\Delta T$ as a function of depletion width / multiplication layer thickness for InP SAM (red squares), InAlAs SAM (blue triangles), and $\text{Al}_x\text{In}_{1-x}\text{As}_y\text{Sb}_{1-y}$ SACM (black diamonds) APDs. A linear best-fit curve is included for each materials system. References are included above data points.	42
Figure 5-1: Band diagram of a staircase APD under zero bias (a) and low reverse bias (b). ²⁹	44
Figure 5-2: 1, 2, and 3-step staircase band structures under 4, 5, and 6 V reverse bias, respectively.	46
Figure 5-3: 543-nm photoabsorption within the staircase APD layer structure.	47
Figure 5-4: Photocurrent of 2-step staircase and 2-step control APDs under 543-nm illumination.	48
Figure 5-5: Gain curve comparison of 1, 2, and 3-step staircase APDs under 543-nm illumination.	49
Figure 5-6: Comparison of impact ionization probability for 1, 2, and 3-step staircase APDs based on equation (5.1).	49
Figure 5-7: C-V curves for 2 and 3-step staircase APDs.	50
Figure 5-8: Dark current density of 2-step (a) and 3-step (b) staircase APDs as a function of temperature.	51
Figure 5-9: Room-temperature dark current density comparison of 1-step staircase APD designs.	53

Figure 5-10: Dark current density of a 1-step staircase design with a 7%-Al narrow-bandgap region as a function of temperature.	53
Figure 5-11: Calculated excess noise factor of 1, 2, and 3-step staircase APDs as a function of gain.....	55
Figure 5-12: Calculated excess noise factor of 1, 2, and 3-step staircase APDs as a function of impact ionization probability.	56
Figure 5-13: Noise power ratio of staircase to control APDs as a function of gain for 1 (a), 2 (b), and 3-step (c) devices.....	59
Figure 5-14: Normalized noise power comparison of 1, 2, and 3-step staircase APDs to PMT noise theory, the model described above, and Monte Carlo simulation results.....	60
Figure 6-1. I-V characteristic of a potential 3- μm SACM APD.....	62
Figure 6-2: Conceptual design of an SACM staircase APD.....	66

1 Introduction

1.1 Motivation

Light detection plays a vital role in modern society, from applications in spectroscopy and imaging to transportation and telecommunications.¹ In each of these fields, sensitivity is a primary limiting factor in detector performance. For example, higher sensitivity in a telecommunications receiver enables longer transmission distances for unrepeated signals,² and the higher sensitivity of a photodetector-based camera allows for detailed high-speed imaging.³

Although various photodetector architectures exist, semiconductor photodiodes provide a platform for chip-level integration while taking advantage of microscopic footprints. These detectors utilize the photoelectric effect, whereby a photon is absorbed into the semiconductor crystal to create a free-carrier electron-hole pair. These charged particles are collected in the form of photocurrent, thereby completing the optoelectronic detection process.

In order to accurately read the electrical signal from a low-intensity optical input, the electrical photocurrent must be amplified. There are two primary methods of doing this. The first involves using an electronic amplifier in conjunction with a photodetector, commonly a simple photodiode with an electronic amplifier. Other than the need for two-element integration, the primary disadvantage of this approach is the added circuit noise of the amplifier.² Receiver sensitivity is directly related to the signal-to-noise ratio (SNR) of the system,⁴ which can be intuitively understood by considering that the low-power signals from low-intensity inputs must remain distinguishable from the magnitude of the noise. This means that even for ultra-low-noise

photodiodes, the additional noise component from the amplifier must be considered, which unavoidably reduces the SNR.

The second solution for increasing the photocurrent is found in the avalanche photodiode (APD). APDs take advantage of the physical phenomena known as impact ionization to multiply the photogenerated carriers. If the energy of carriers is sufficiently increased, their collisions with surrounding electrons enables them to excite a bound electron in the valence band to the conduction band, creating an electron-hole pair. The energy of these liberated carriers is subsequently increased, enabling the process to repeat. This chain reaction, or avalanche, provides the internal gain mechanism by which the electrical signal is amplified. As long as the total APD noise is lower than the sum of the photodiode and amplifier noise, APDs provide a distinct advantage in optical sensitivity. For this reason, APDs have been widely used in telecommunications,⁵ data centers,⁶ spectroscopy,^{7,8} imaging,⁹ LIDAR,¹⁰ and quantum applications.^{11,12} Figure 1-1 illustrates this sensitivity advantage by comparing a PIN photodiode to five APDs of varying noise levels, as indicated by the k factor, the ratio of the hole to electron impact ionization coefficients, described below.

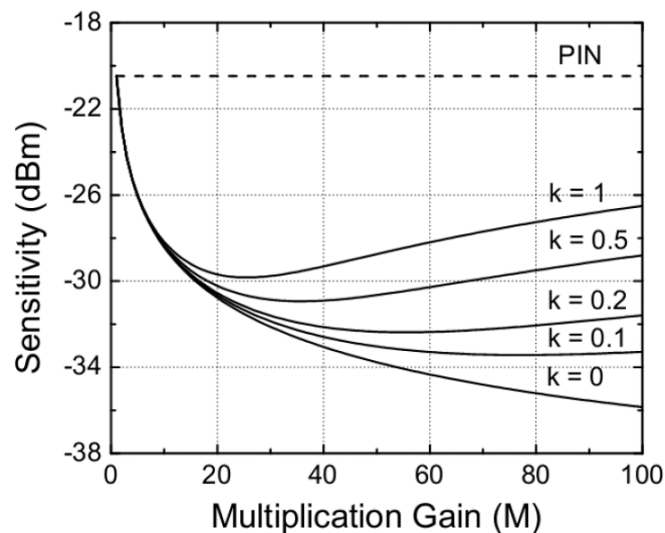


Figure 1-1. Comparison of a PIN photodiode ($M = 1$) to APDs with various k factors.

Impact ionization in an APD varies slightly from event to event. In other words, the number of multiplied photogenerated carriers originating from one photon may be different from those originating from another photon. This variance in the gain ultimately increases the APD shot-noise current, which diminishes the sensitivity, SNR, and device bandwidth.¹³ Identifying means by which to control and diminish the noise-contributing mechanisms in the avalanche process is vitally important to improving APD performance in most applications.

1.2 APD Noise

The stochastic nature of impact ionization creates variations in the amplified signal and thereby creates excess noise, which is quantified by an excess noise factor, $F(M)$

$$F(M) = \frac{\langle M^2 \rangle}{\langle M \rangle^2} = 1 + \frac{\text{var}(M)}{\langle M \rangle^2} \quad (1.1)$$

where M is the multiplication factor (gain).¹⁴ Spatial and temporal variance in the impact ionization process also contribute to the excess noise. For conventional APDs, $F(M)$ is described by the McIntyre local field model¹⁵

$$F(M) = kM + (1 - k) \left(2 - \frac{1}{M} \right) \quad (1.2)$$

where k is the ratio of the electron (α) and hole (β) impact ionization coefficients, such that $k < 1$. These impact ionization coefficients represent the inverse of the mean distance traveled within a material before their respective carriers impact ionize. Suppressing one of these carriers and thereby decreasing k results in making the multiplication process more deterministic and

reducing the excess noise factor. Figure 1-2(a) illustrates an impact ionization process with equal contributions from both electrons and holes ($k = 1$) and Fig. 1-2(b) illustrates a hole-suppressed impact ionization process ($k = 0$).

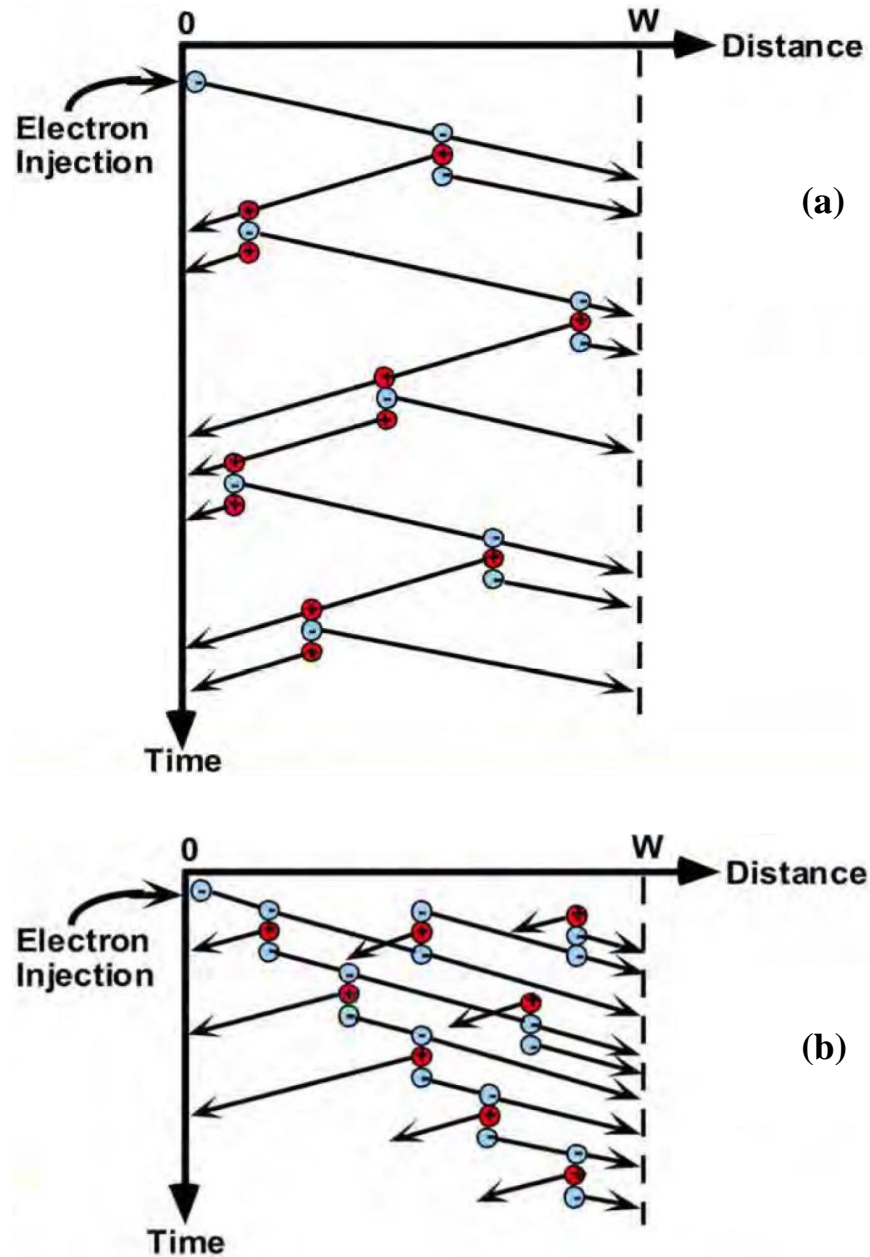


Figure 1-2. Illustration of impact ionization for $k = 1$ (a) and $k = 0$ (b) for single electron injection.

The mean-squared APD shot noise current is scaled to the excess noise factor by:

$$\langle i_{shot}^2 \rangle = 2qM^2(I_{ph} + I_d)F(M)\Delta f \quad (1.3)$$

where q is the charge of an electron, Δf is the bandwidth, and I_{ph} and I_d are the photocurrent and dark current, respectively. While the excess noise factor itself increases with the gain at a rate determined by the k factor, the magnitude of the shot noise current is then scaled to the excess noise factor and the gain squared, meaning that even a small increase in the k factor contributes to a much larger increase in the shot noise current. Engineering the impact ionization to reduce its excess noise contribution is the primary focus in designing low-noise APDs.

There are two approaches in designing low-noise APDs—reducing the k factor, and engineering the multiplication layer band structure to make impact ionization more deterministic. The k factor is largely determined by the material used for avalanche multiplication. As shown in Figure 1-3, this value has been well characterized for many semiconductor materials, a champion of which is silicon with $k = 0.01$ - 0.02 .¹⁶

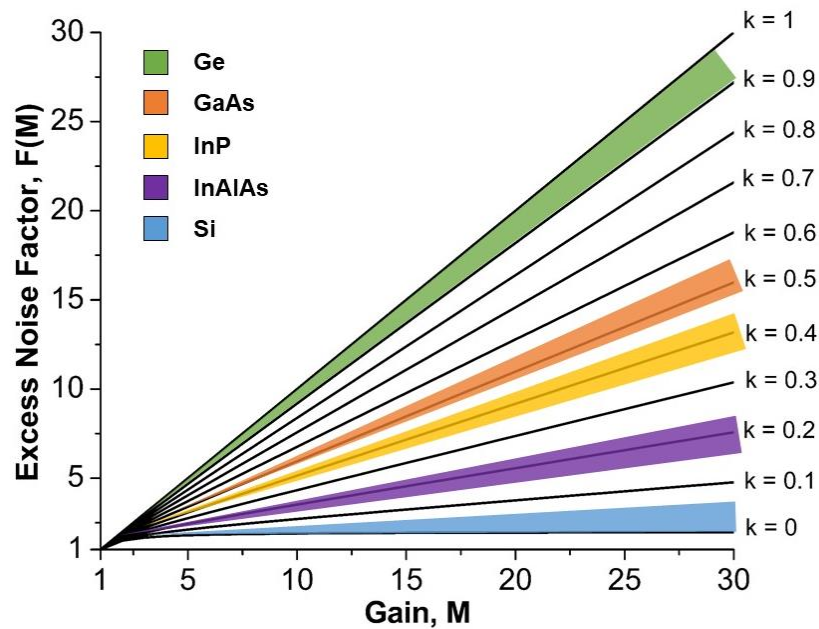


Figure 1-3. k factor for various materials systems.

In order to reduce the overall APD excess noise, materials must be chosen for the APD multiplication region that have a low k factor. This severely limits the materials that can be considered for a device, as other material parameters such as lattice matching and optical cutoff wavelength must take precedence. An abundance of research has gone into the design of superlattice materials which attempt to capture these desirous materials properties simultaneously.^{17–20}

As an additional consideration, it should be noted that k tends to increase in high electric fields, meaning that in the case of traditional APDs, high gain signifies noisier performance. An exception to this behavior is in APDs with thin multiplication layers. A reduced multiplication layer thickness necessitates that a higher electric field must be applied in order to achieve similar gain to that of a thicker multiplication layer. Due to this increased electric field, the excess noise would intuitively be higher as well; however, this is not the case. For multipliers with thicknesses comparable to the required distance for a carrier to impact ionize, the probability for gain fluctuations within the region is reduced, resulting in suppressed excess noise.^{21–23} This phenomenon, known as the dead-space effect, has been employed in top-illuminated APDs for telecommunications and LIDAR applications in order to provide high-speed performance with reduced excess noise.^{24,25}

The other method for designing low-noise APDs involves multiplication layer band engineering. This approach seeks to reduce the stochasticity of the impact ionization process by localizing the events to specific locations, similar to dynodes in a photomultiplier tube (PMT). In one instance, materials with lower impact ionization thresholds can be used to replace sections of a material with a higher threshold within the multiplication layer, localizing the impact ionization events to the lower threshold locations.²⁶ This can be accomplished, for example, by creating a

series of heterojunctions in the AlGaAs/GaAs materials system.^{27,28} As before, the resulting reduction in the gain variance serves to lower the excess noise. Another instance of engineering the band structure involves designing abrupt discontinuities in the conduction band energy to induce impact ionization.^{29,30} This “staircase” structure, which is the subject of section 5, offers the potential for discrete multiplication gain and exceptionally low noise.

In this work, I measured APD noise power with a noise figure analyzer (NFA) relative to a calibrated noise source. To extract the excess noise figure, $F(M)$, we solve the local field model of noise power spectral density (S)

$$S_N = 2qIRM^2F(M) \quad (1.4)$$

where R is the total impedance of the measurement setup. At unity gain, $F(M)$ is unity, and equation (1.4) becomes:

$$S = S_0 = 2qIR \quad (1.5)$$

By taking subsequent measurements where $M > 1$, the excess noise factor can be solved by equation (1.6). Practically, noise power measurements are made under dark and illuminated conditions at a given frequency. These values in their absolute form are subtracted from one another, resulting in a photo-noise value N_p , at the measurement frequency.

$$F(M) = \frac{S_N}{S_0M^2} = \frac{N_{p,N}}{N_{p,0}M^2} \quad (1.6)$$

$F(M)$ can then be plotted as a function of M similar to Figure 1-3, from which the approximate k value according to equation (1.2) can be determined.

My setup for measuring noise power and excess noise is shown in Figure 1-4. The DUT is coupled to a source meter and the NFA through an RF bias tee. Care must be taken to avoid illuminating the APD mesa sidewall, which can result in inaccurate measurements.

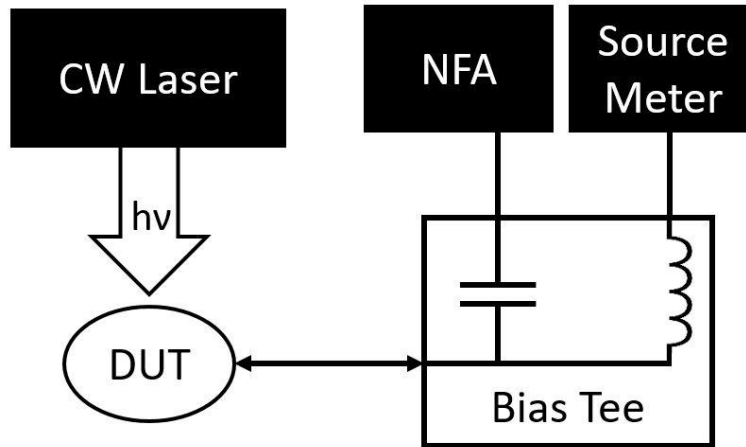


Figure 1-4: Block diagram of noise measurement setup.

1.3 Dark Current and Gain

Ideally, dark current in reverse bias is the saturation diffusion current. Realistically however, various mechanisms induce additional flow of carriers, resulting in higher dark current. Dark current is inherently deleterious, as it contributes to increasing the shot noise and decreasing both the SNR and bandwidth.

Three mechanisms are responsible for dark current: diffusion, recombination-generation, and band-to-band tunneling. Diffusion current, which is a result of carrier motion due to their non-equilibrium distribution, can be suppressed through device cooling and using wider-bandgap materials. Recombination-generation current is caused by the capture and emission of electrons and holes by deep-level trap states in the semiconductor bandgap. As such, this component of the

dark current can be reduced by improving material quality to reduce defects and trap states as well as by using wider-bandgap materials. Surface passivation can be used to diminish this mechanism on the APD mesa sidewalls by removing dangling bonds caused during the material etching process. As its name indicates, band-to-band tunneling current is caused by carriers quantum-mechanically tunneling through the narrow potential barrier presented by the semiconductor bandgap. Likewise, in some materials, defect energy states in the bandgap can lead to trap-assisted tunneling. Tunneling is mostly prevalent in high electric fields or in materials with small electron effective mass and narrow bandgaps. Tunneling-dominated current is negligibly affected by device cooling and must be primarily reduced by widening the semiconductor bandgap or reducing the electric field.

The desired current from an APD is that which results from the photogenerated carriers, known as photocurrent (I_{ph}). Due to the presence of dark current, however, the current directly measured from an illuminated device (I_{total}) is a combination of the two:

$$I_{total} = I_{ph} + I_d \quad (1.7)$$

The above values are best shown plotted as a function of the bias (voltage) applied to the APD in what is known as a current-voltage (I-V) curve. Figure 1-5 illustrates a typical photocurrent I-V curve for a traditional PIN APD. Under positive bias, current should freely flow through the device, resembling a short circuit behavior. Under reverse bias, however, the intrinsically doped region will first deplete, as indicated by a small increase in photocurrent. After full depletion, the photoresponse is relatively independent of bias, characteristic of a traditional PIN photodiode. At a sufficiently higher bias, which corresponds to a high electric field in this region, carriers begin to gain enough energy to impact ionize, leading to an abrupt increase in photocurrent.

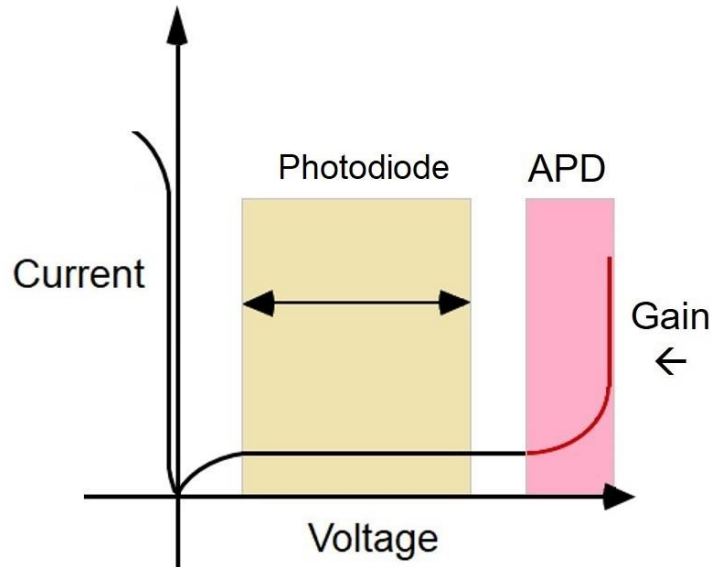


Figure 1-5: Typical APD I-V curve.

Gain results from the impact ionization occurring in this high-bias region of the I-V curve and is calculated as the ratio of the impact-ionizing photocurrent to the photocurrent in the “photodiode” region. This can be expressed as

$$M = \frac{I_{ph}}{I_{ph,0}} = \frac{I_{total} - I_d}{I_{total,0} - I_{d,0}} \quad (1.8)$$

where the 0 values represent those measured in the non-impact-ionizing “photodiode” region, or at unity gain.

1.4 Quantum Efficiency

Quantum efficiency measures the ability of an APD to convert each incident photon into an electron-hole pair and is typically characterized as either internal or external. Internal quantum efficiency measures the ratio of collected electrons to photons that have entered the semiconductor solid by

$$\eta_{int} = \zeta(1 - e^{-\alpha x}) \quad (1.9)$$

where ζ is the fraction of electron-hole pairs which contribute to the photocurrent without recombining, α is the material absorption coefficient, and x is the thickness of the absorbing material. External quantum efficiency (EQE) accounts for the quantity of photons which do not enter the material and is defined as the ratio of collected electrons to photons incident on the device. This quantity allows for a more “black box” approach to optoelectronic conversion:

$$\eta_{ext} = (1 - R)\zeta(1 - e^{-\alpha x}) \quad (1.10)$$

Here R is the surface reflectivity of the semiconductor. EQE can also be written in terms of easily measurable device parameters or responsivity, which is defined as the ratio of photocurrent (A) to incident optical power (W)

$$R_{esp} = \frac{q}{h\nu} (1 - R)\zeta(1 - e^{-\alpha x}) = \eta_{ext} \frac{q}{h\nu} \quad (1.11)$$

where q is the elementary charge, h is the Planck constant, and ν is the optical frequency.

In this work, I measured EQE values using the setup in Figure 1-6. For these measurements, I used a high-pressure xenon gas laser-driven lamp as a stable, broad-spectrum light source. By using a monochromator with internal diffraction gratings of various groove densities and spectral blazes, I was able to isolate narrow-band regions of this spectrum for the measurements. The output of the monochromator was focused through a chopper and long-pass filter onto the DUT, whereby a lock-in amplifier measured the device photocurrent. The EQE of the DUT was calculated by comparing the output of the DUT with that of a photodiode with known responsivity:

$$EQE_{DUT} = EQE_{known} \frac{I_{photo,DUT}}{I_{photo,known}} \quad (1.12)$$

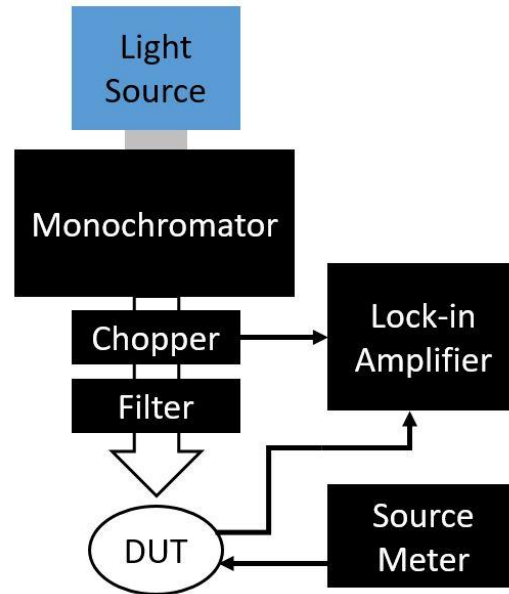


Figure 1-6. Block diagram of EQE setup.

The resulting EQE values are typically plotted as a function of wavelength for the full spectrum of measurement.

1.5 Bandwidth

Bandwidth is a measure of the speed of a device, or specifically, how quickly an APD can respond to input signals. Higher bandwidth indicates a device's ability to operate faster, which is a critical component in applications such as telecommunications and data communications where speed is directly related to data throughput. 3dB bandwidth, which is a common figure of merit, describes the frequency at which the RF output power has decreased by 3dB, or approximately 50%.

The two limiting factors in APD bandwidth are the RC time constant and the carrier transit time. It is well established that the RC time constant of a PIN junction is the inverse of $2\pi RC$, or more specifically

$$f_{RC} = \frac{1}{2\pi RC} = \frac{d}{2\pi(R_s + R_L)\epsilon A} \quad (1.13)$$

where d is the depletion region thickness, A is the device area, ϵ is the dielectric constant of the material, and R_s and R_L are the series and load resistances of the device, respectively. As in most RF applications, R_L is typically 50Ω . The transit-time bandwidth is given by

$$f_{transit} = \frac{v_s}{2d} \quad (1.14)$$

where v_s is the average saturation velocity of electrons and holes in the material. These two bandwidth components can be combined to calculate the approximate 3dB bandwidth of the device:

$$f_{3dB} \cong \left(\frac{1}{f_{RC}^2} + \frac{1}{f_{transit}^2} \right)^{-\frac{1}{2}} \quad (1.15)$$

Since a longer time is required for carriers to move a longer distance, it follows that to reduce the transit-time bandwidth, a thinner device is required. However, according to equation (1.10), higher EQE requires a thicker device. Herein lies the weakness of top-illuminated PIN APDs, as high performance of one of these factors implies low performance of the other. Likewise, a tradeoff exists between the RC bandwidth and the transit-time bandwidth, due to

their opposing relation to depletion region thickness, d . Various physical architectures, such as waveguide structures, have been designed to overcome these limitations.^{31–33}

While transit-time typically cannot be modified without changing the multiplication layer geometry, there are several methods for improving the RC bandwidth component. Primarily, devices with a smaller area and a lower capacitance value will increase the bandwidth. Additionally, the resistive component can be reduced by addressing R_s , which is the sum of both the contact resistance and the sheet resistance. Ohmic contacts, having Schottky barriers ≤ 0 eV, provide the least resistance, meaning careful attention must be given to the contact metal work function and Fermi pinning at the metal-semiconductor interface. Contact annealing has often been used to improve contact resistance. Sheet resistance indicates the resistivity of the semiconductor itself and is highly dependent on material properties such as mobility and dopant concentration.

Both contact resistance and sheet resistance can be easily characterized through I-V measurements of transmission line structures on a device, which are metal contacts on the semiconductor separated by varying known distances. The resulting resistance values (R) calculated by Ohm's law can be linearly fit as a function of distance (x) as

$$R = \frac{R_{sheet}}{w}x + 2R_{contact} \quad (1.16)$$

where w is the width of the contact.

The bandwidth of APDs is also related to the excess noise factor and therefore k .¹³ By definition, APDs with $k > 0$ experience impact ionization of both electrons and holes. The dual-carrier interaction creates a feedback cycle within the multiplication process, increasing the

amount of time needed for the avalanche to accumulate. This limitation, known as the avalanche build-up time, is highly affected by the feedback cycle and therefore sensitive to small changes in k . Figure 1-7 is a plot of APD bandwidth as a function of gain for varying k values according to the local field model.^{13,15} This figure signifies that for devices with very low k values, bandwidth is nearly independent of the operating gain. However, as k increases, the 3dB bandwidth is severely restricted at higher gains, indicating that APDs with higher excess noise are limited to operating at low gain in order to achieve comparable bandwidth. This inverse relation between k and bandwidth further emphasizes the value of low-noise APDs.

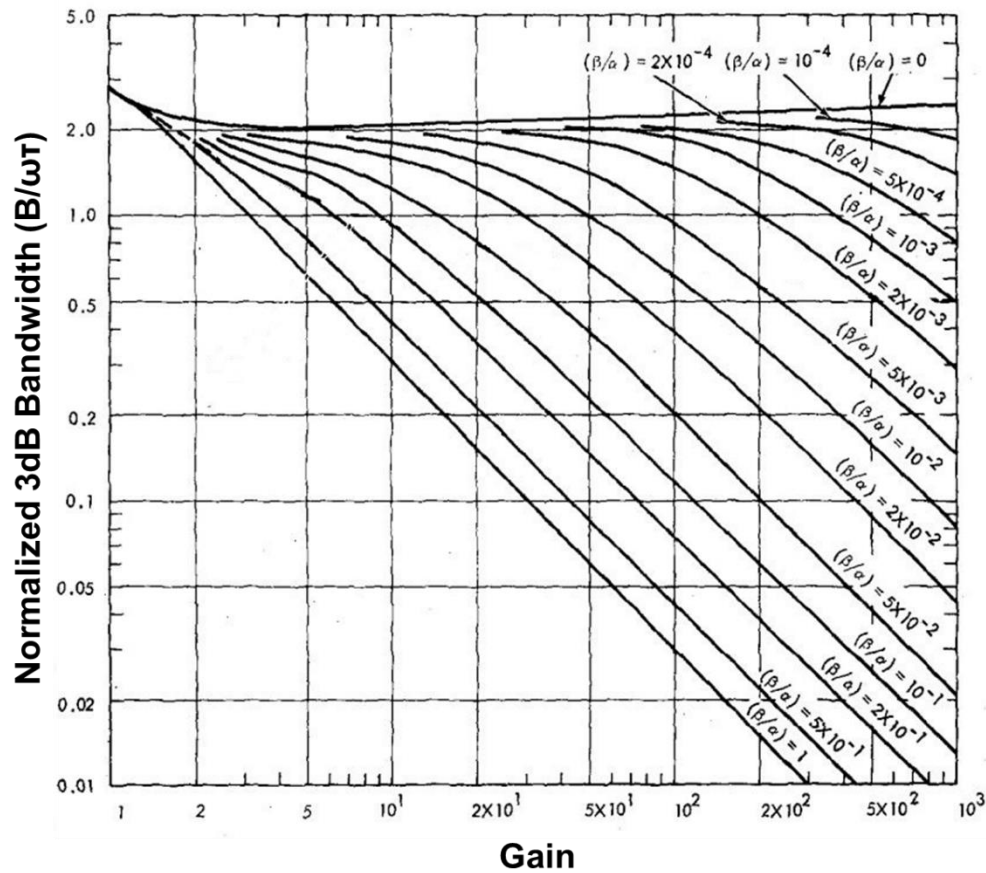


Figure 1-7: Bandwidth as a function of gain for varying k values.¹³ Here k is denoted by (β/α) .

1.6 Material Growth and Fabrication

The $\text{Al}_x\text{In}_{1-x}\text{As}_y\text{Sb}_{1-y}$ materials system lattice matched to GaSb has been traditionally grown as a bulk quaternary material limited to ($x \approx 0.3$) due to a miscibility gap. The University of Texas at Austin recently demonstrated a digital alloy growth technique to overcome this miscibility gap and enable aluminum concentrations up to $x = 0.8$.³⁴ This material is grown by molecular beam epitaxy (MBE) using a series of repeating shutter sequences to form thin layers of the constituent binaries AlSb, AlAs, InSb, and InAs. A TEM image of the resulting $\text{Al}_x\text{In}_{1-x}\text{As}_y\text{Sb}_{1-y}$ material is shown in Figure 1-8.³⁵ Be and Te are used as p-type and n-type dopants, respectively.

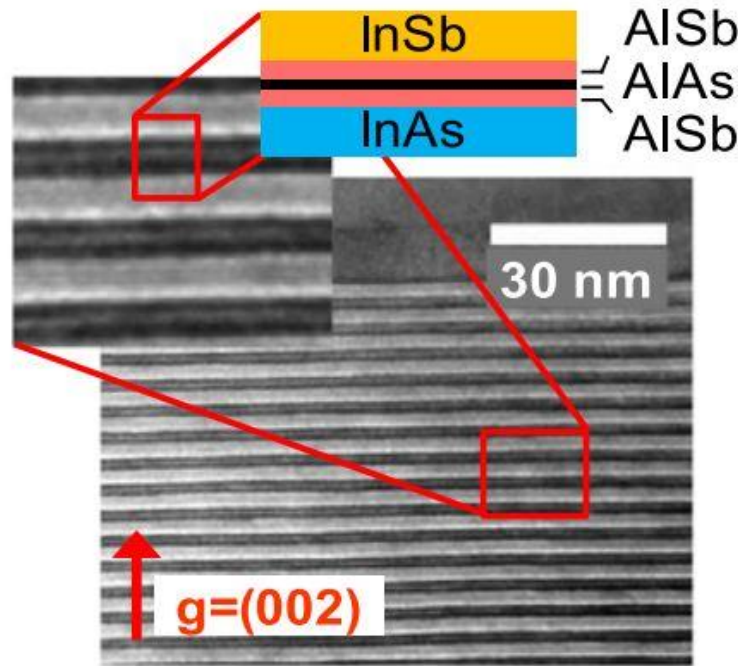


Figure 1-8: TEM cross section of $\text{Al}_x\text{In}_{1-x}\text{As}_y\text{Sb}_{1-y}$.³⁵

$\text{Al}_x\text{In}_{1-x}\text{As}_y\text{Sb}_{1-y}$ has demonstrated champion APD qualities in temperature stability, dark current, and excess noise.^{36–38} Furthermore, it has been shown that the $\text{Al}_x\text{In}_{1-x}\text{As}_y\text{Sb}_{1-y}$ bandgap decreases proportionally to Al content but primarily by reducing the conduction band edge,

resulting in the potential to design complex APD structures while maintaining low-noise characteristics.^{35,39} This bandgap change fundamentally affects the spectral absorption cutoff, meaning that $\text{Al}_x\text{In}_{1-x}\text{As}_y\text{Sb}_{1-y}$ APDs with lower Al concentrations are able to absorb longer photon wavelengths. Figure 1-9 illustrates this through the spectral response of various $\text{Al}_x\text{In}_{1-x}\text{As}_y\text{Sb}_{1-y}$ APDs.³⁸ The optical cutoff wavelength increases from approximately 1 to 5 μm as the Al fraction decreases from $x = 0.8$ to 0. Photoabsorption is directly linked to the bandgap energy, which is related to the Al fraction (x) according to the following equation:³⁴

$$E_g(x) = 0.247 + 0.97x + 0.47x^2 \quad \text{eV} \quad (1.17)$$

The bandgap energy and optical cutoff wavelength are plotted as functions of the Al concentration in Figure 1-10.

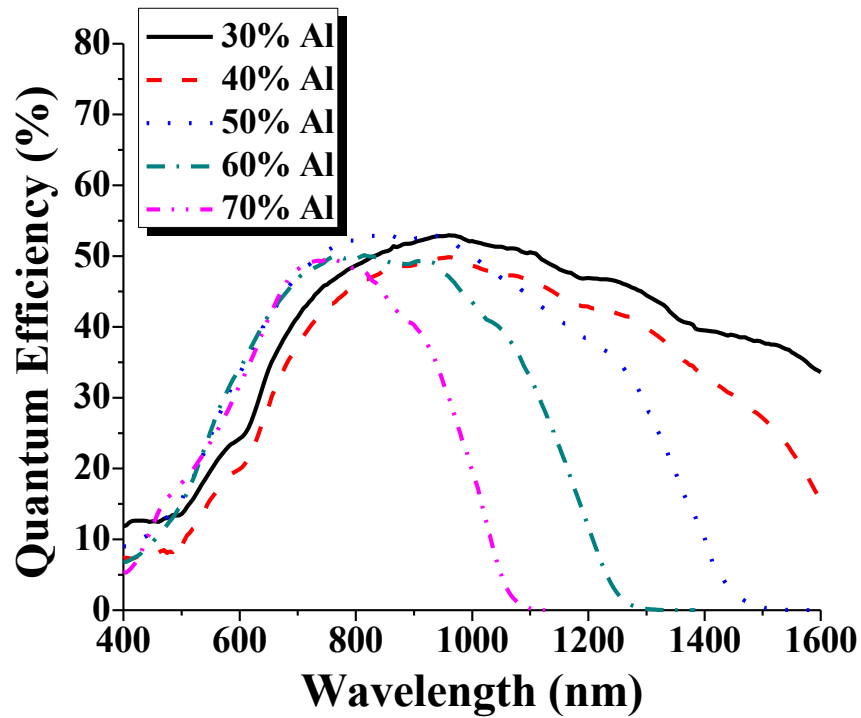


Figure 1-9: EQE of $\text{Al}_x\text{In}_{1-x}\text{As}_y\text{Sb}_{1-y}$ APDs ($x = 0.3-0.7$).³⁸

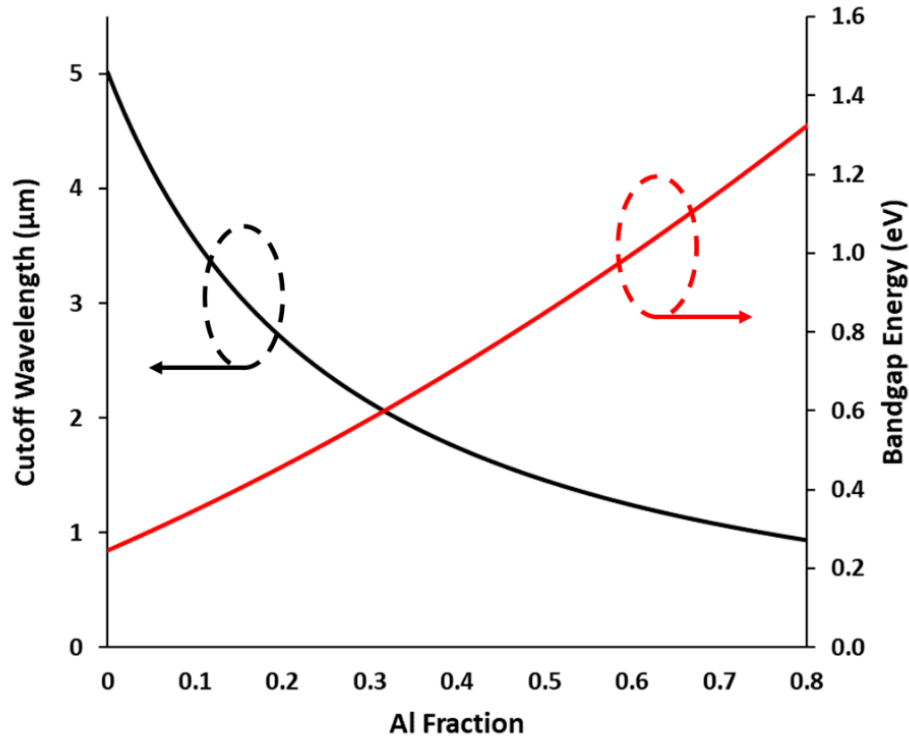


Figure 1-10: Cutoff wavelength and bandgap energy as a function of Al fraction.

After material growth, APDs must be fabricated from the epitaxial wafer. While there are many complex physical architectures and processes for fabricating APDs, the simplest of these is the vertically-illuminated APD, which was the design primarily used throughout my studies. The process for fabricating this type of APD is described below.

Figure 1-11 illustrates the fabrications process. Once the wafer sample (a) has been thoroughly cleaned, photolithography is used to define mesa locations (b). Following this, the mesas are etched into the epitaxial layers either chemically or by reactive ion etching (RIE) (c). The remaining photoresist is then removed (d), and a new pattern is defined for metal contacts (e). Contacts are deposited either through electron-beam evaporation or plating (f), and the remaining metal is removed in a lift-off process (g). Finally, a passivation coating such as SU-8 is spun onto the device (h), and the contacts and top surface reopened (i).

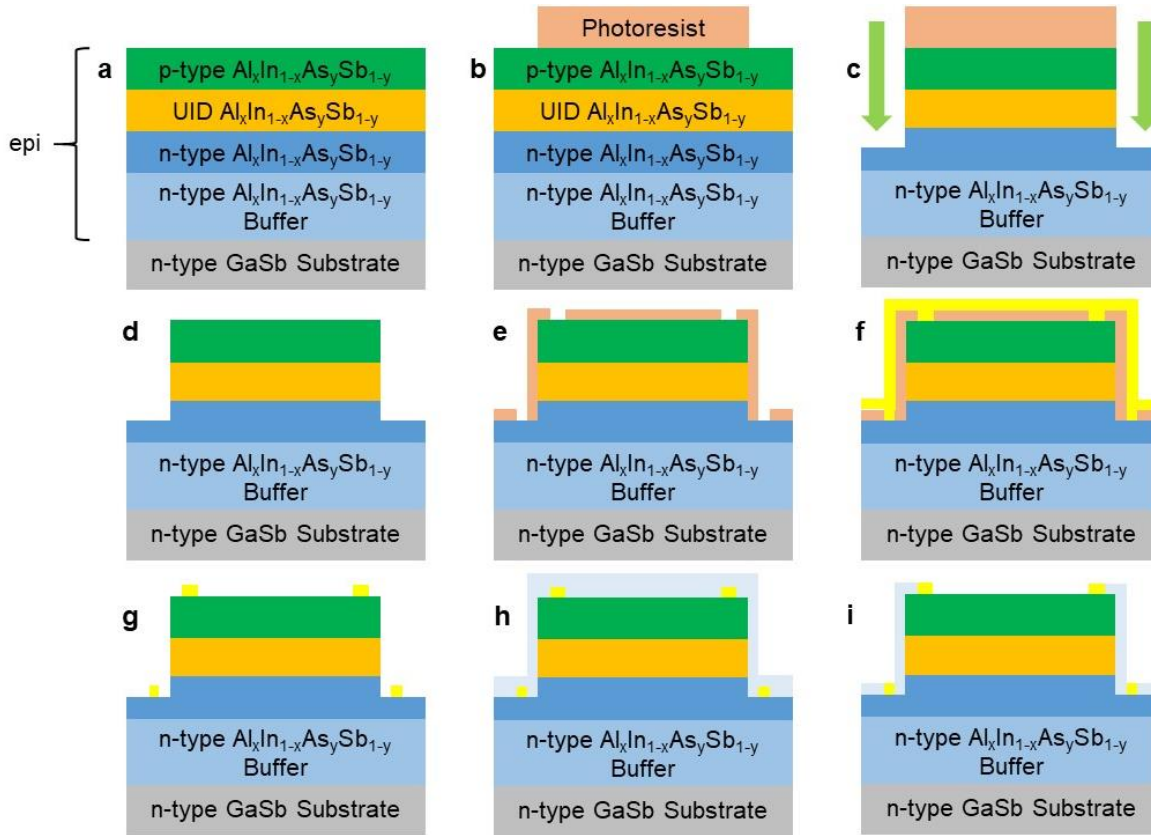


Figure 1-11: Fabrication process flow.

Detailed fabrication processes are included in appendix 2.

1.7 Thesis Organization

This thesis describes my work in developing innovative low-noise APDs in the $\text{Al}_x\text{In}_{1-x}\text{As}_y\text{Sb}_{1-y}$ materials system. Chapter 1 describes the motivation for this research and the figures of merit that play a key role in characterizing these APDs. Chapter 2 details my early work with $\text{Al}_x\text{In}_{1-x}\text{As}_y\text{Sb}_{1-y}$ APDs as I characterized their temperature stability. Chapter 3 discusses the significance of $\text{Al}_{0.8}\text{In}_{0.2}\text{As}_y\text{Sb}_{1-y}$ APDs and my involvement in their development and characterization. In chapter 4, I begin discussion of the topics presented in my dissertation

proposal, namely $\text{Al}_x\text{In}_{1-x}\text{As}_y\text{Sb}_{1-y}$ separate absorption, charge, and multiplication (SACM) APDs for mid-wave infrared (MWIR) applications. Two architectures that utilize $\text{Al}_{0.3}\text{In}_{0.7}\text{As}_y\text{Sb}_{1-y}$ absorbers specifically for 2- μm detection are presented in this section. Continuing with my dissertation proposal topics, chapter 5 introduces the staircase APD, an architecture originally described by Federico Capasso and collaborators in 1982.²⁹ Here both 2 and 3-step $\text{Al}_x\text{In}_{1-x}\text{As}_y\text{Sb}_{1-y}$ staircase APDs are presented, as well as a 1-step design with improved dark current. Chapter 5 also briefly discusses the groundbreaking noise power performance measured in $\text{Al}_x\text{In}_{1-x}\text{As}_y\text{Sb}_{1-y}$ staircase APDs. Chapter 6 concludes with proposed future research topics and improvements to the aforementioned APDs. Two appendices have been included in this document which contain details of device simulation and fabrication.

2 $\text{Al}_x\text{In}_{1-x}\text{As}_y\text{Sb}_{1-y}$ Temperature Stability

APDs typically exhibit a proportional relationship between ambient temperature and the bias required to maintain a constant gain. This is due to a change in impact ionization efficiency with temperature. Phonon scattering increases with temperature, necessitating a higher electric field and hence a higher reverse bias to realize a given gain value. This gain-temperature relationship can be extended to the variation of breakdown voltage with temperature and is characterized by the breakdown voltage temperature coefficient $\Delta V_{\text{bd}}/\Delta T$.⁴⁰ APDs operated in Geiger mode, which is used for single photon detection, are even more susceptible to slight variations in temperature. As a result of this dependence, complex cooling circuits are required to maintain constant gain. APDs requiring only simple bias feedback circuits due to minimal values of $\Delta V_{\text{bd}}/\Delta T$ are desirable for such highly sensitive applications.

Another factor contributing to $\Delta V_{\text{bd}}/\Delta T$ is the APD multiplication layer thickness. It has been shown that as the thickness of this layer increases, $\Delta V_{\text{bd}}/\Delta T$ increases linearly for temperatures between 200 and 400 K, while at lower temperatures, $\Delta V_{\text{bd}}/\Delta T$ is minimized.^{40,41}

InP and InAlAs APDs are widely used due to their low dark current and compatibility with near-infrared (NIR) fiber optic telecommunications links.⁴² Silicon APDs are also widely used for their low-noise characteristics and compatibility with high-speed integrated circuitry, although owing to the bandgap energy of silicon, they cannot be used directly for NIR absorption. Extensive studies have categorized the temperature dependence of APDs designed in these material systems.^{40,41} More recently, thin $\text{Al}_{1-x}\text{Ga}_x\text{As}_{0.56}\text{Sb}_{0.44}$ APDs, which are lattice matched to InP, were also reported with exceptionally low $\Delta V_{\text{bd}}/\Delta T$ values.⁴³

To investigate the $\Delta V_{bd}/\Delta T$ of $Al_xIn_{1-x}As_ySb_{1-y}$, samples with $x = 0.6, 0.7$, and 0.8 were placed in a liquid-nitrogen cooled cryogenic chamber and illuminated with a fiber-coupled CW laser. Gain measurements were taken at 20-K temperature intervals, allowing the devices to equilibrate for a period of time after each change. The breakdown voltage was determined by extrapolating $1/M$ to zero, and the resulting values were plotted as a function of temperature, as shown in Figure 2-1. The slope of these lines indicates the $\Delta V_{bd}/\Delta T$ values.

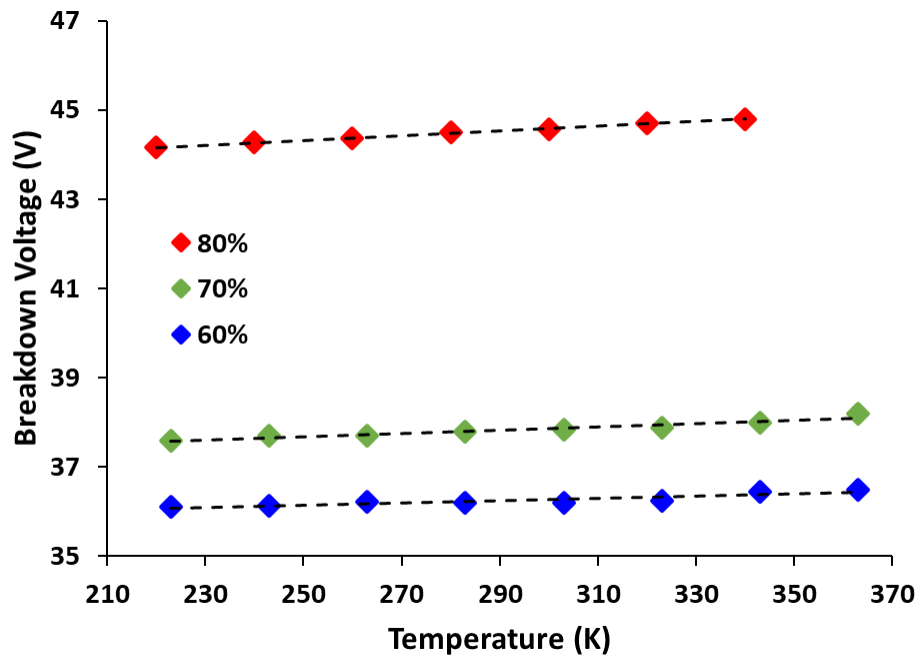


Figure 2-1: Breakdown voltage as a function of temperature for the indicated $Al_xIn_{1-x}As_ySb_{1-y}$ devices.

By comparing the extracted $Al_xIn_{1-x}As_ySb_{1-y}$ $\Delta V_{bd}/\Delta T$ values with those from APDs of other materials systems, it was determined that $Al_xIn_{1-x}As_ySb_{1-y}$ APDs offer exceptional temperature stability. Figure 2-2 shows $\Delta V_{bd}/\Delta T$ for $Al_xIn_{1-x}As_ySb_{1-y}$, InP, InAlAs, AlAsSb, Silicon, and $Al_{1-x}Ga_xAs_{0.56}Sb_{0.44}$ PIN APDs as a function of multiplication layer thickness.^{36,37,40,41,43,44} Additional temperature characterizations of $Al_xIn_{1-x}As_ySb_{1-y}$ SACM APDs are given in section 4. Since these devices are of a different architecture than the PIN devices discussed here, they are not included.

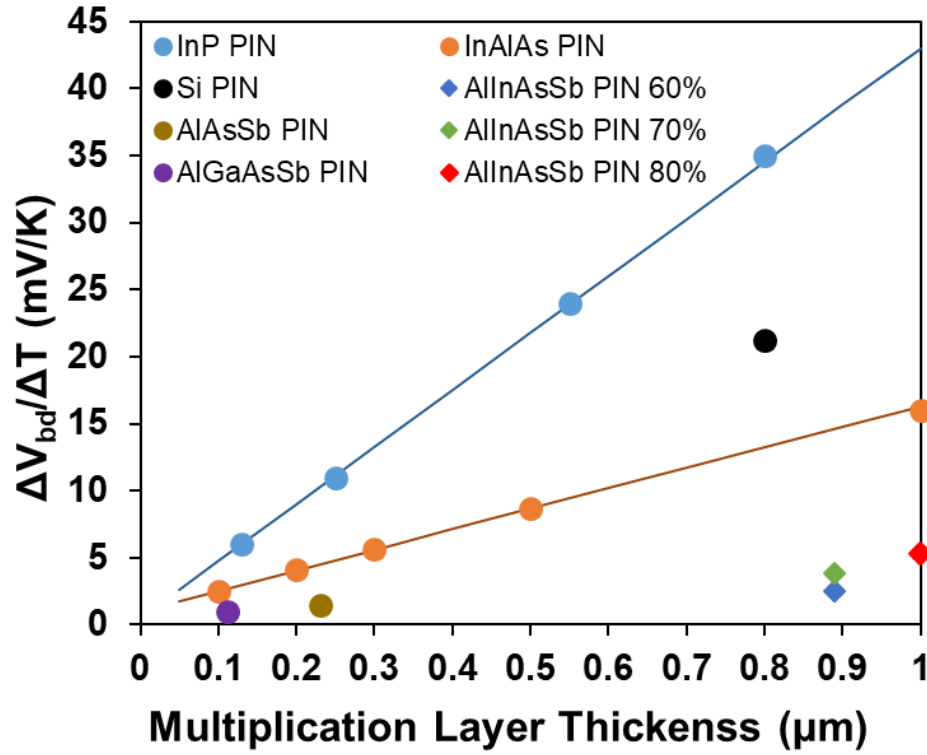


Figure 2-2: $\Delta V_{bd}/\Delta T$ for PIN APDs as a function of multiplication layer thickness.

It is theorized that the high temperature stability of $\text{Al}_x\text{In}_{1-x}\text{As}_y\text{Sb}_{1-y}$ APDs is directly linked to the digital alloy material. It has been shown that as the layer thicknesses of superlattices decrease, thermal conductivity is dominated by extrinsic processes and that the nature of phonon scattering transitions from particle-like to wave-like, allowing for destructive phonon interference within the material.^{45,46}

Studies with $\text{Al}_x\text{In}_{1-x}\text{As}_y\text{Sb}_{1-y}$ APDs over a wide range of ambient temperatures show superior $\Delta V_{bd}/\Delta T$ compared to APDs of conventional materials, demonstrating robust performance amid temperature fluctuations. Combined with the previously reported low-noise and high absorption efficiency characteristics of these devices,³⁵ $\text{Al}_x\text{In}_{1-x}\text{As}_y\text{Sb}_{1-y}$ APDs offer the potential for high-performance over a wide range of operating temperatures.

3 $\text{Al}_{0.8}\text{In}_{0.2}\text{As}_y\text{Sb}_{1-y}$ APDs

As previously mentioned, the digital alloy growth technique of $\text{Al}_x\text{In}_{1-x}\text{As}_y\text{Sb}_{1-y}$ allows for Al concentrations from $x = 0$ to 0.8. At this maximum, referred to as 80% Al, the energy band minimum begins to shift from a direct Γ -valley to an indirect X-valley bandgap.³⁴ Due to the wide-bandgap nature of this material, however, low dark current and high gain was expected.

Investigation of this 80% material began with measurement of the I-V characteristics, excess noise, and EQE. Unfortunately, these devices showed much higher dark current than anticipated, as well as a bias-dependent responsivity.⁴⁷ This was attributed to high background doping within the intrinsic region of the PIN structure as well as non-ideal fabrication techniques. Despite these drawbacks, reasonable gain and low excess noise were observed. Figure 3-1 shows the excess noise measurement for this $\text{Al}_{0.8}\text{In}_{0.2}\text{As}_y\text{Sb}_{1-y}$ sample, which indicates $k \approx 0.05$.

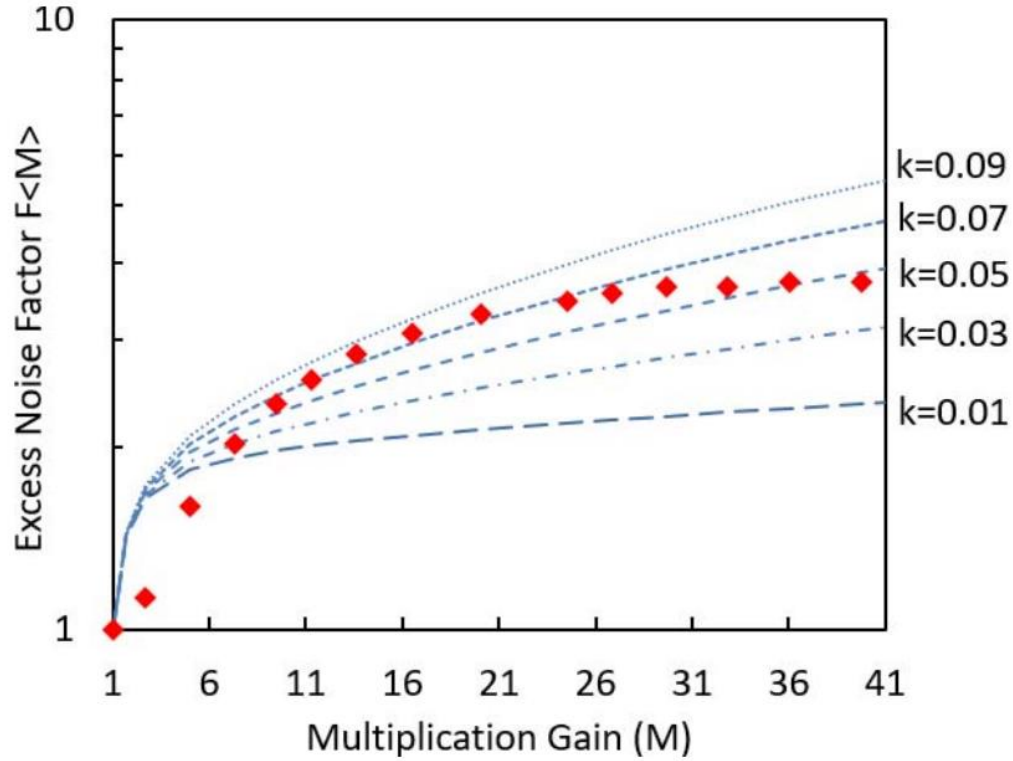


Figure 3-1: Excess noise as a function of gain for an $\text{Al}_{0.8}\text{In}_{0.2}\text{As}_y\text{Sb}_{1-y}$ APD.⁴⁷

In order to better characterize this material and eliminate the high background doping, a second sample was grown. Upon fabrication and testing, this new sample no longer exhibited the bias-dependent responsivity seen previously, signifying a lower background dopant concentration. In addition, I used a new citric-acid-based etching technique to improve the quality of the mesa sidewalls. Combined, these improvements enabled the measurement of much reduced dark current and gain > 1300 , as shown in Figure 3-2.³⁷

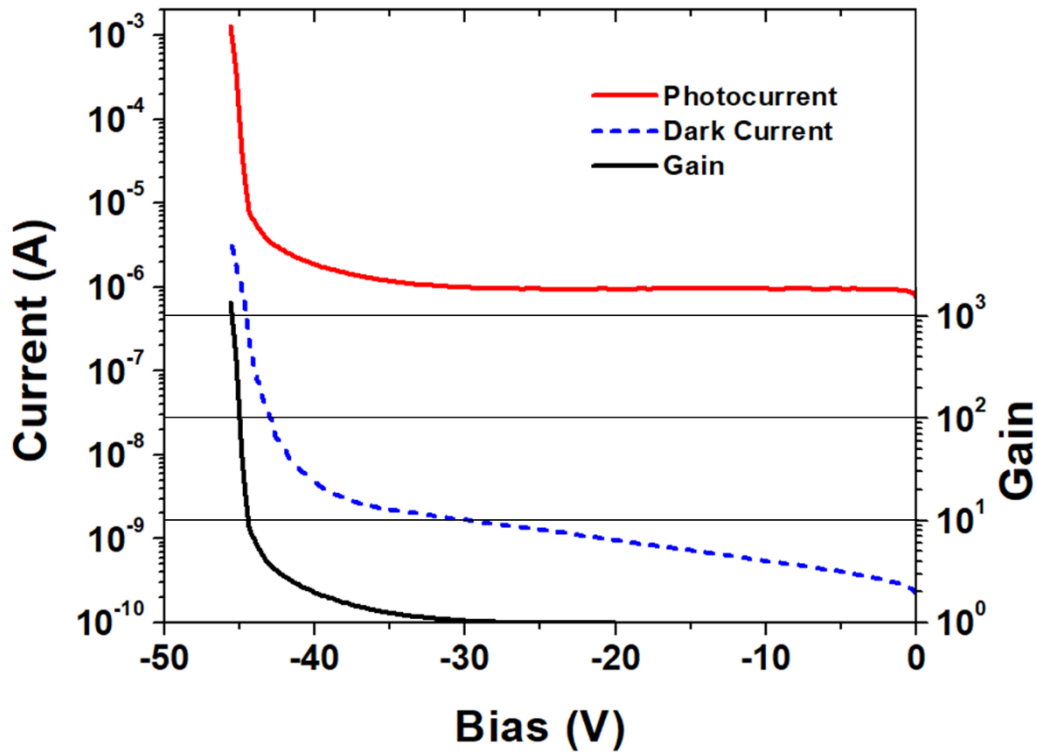


Figure 3-2: I-V characteristic of an improved $\text{Al}_{0.8}\text{In}_{0.2}\text{As}_y\text{Sb}_{1-y}$ APD.³⁷

Additionally, the absorption coefficient of $\text{Al}_{0.8}\text{In}_{0.2}\text{As}_y\text{Sb}_{1-y}$ was measured using spectroscopic ellipsometry. Figure 3-3 shows this data next to that of $\text{Al}_{0.7}\text{In}_{0.3}\text{As}_y\text{Sb}_{1-y}$ (70%),⁴⁸ which has a direct bandgap, and silicon,⁴⁹ which has an indirect bandgap. The absorption coefficient of $\text{Al}_{0.8}\text{In}_{0.2}\text{As}_y\text{Sb}_{1-y}$, is much greater than that of silicon and closer to that of $\text{Al}_{0.7}\text{In}_{0.3}\text{As}_y\text{Sb}_{1-y}$ in the visible and short-wave infrared spectrum, which may indicate that the $\text{Al}_{0.8}\text{In}_{0.2}\text{As}_y\text{Sb}_{1-y}$ bandgap remains direct or very close to direct.

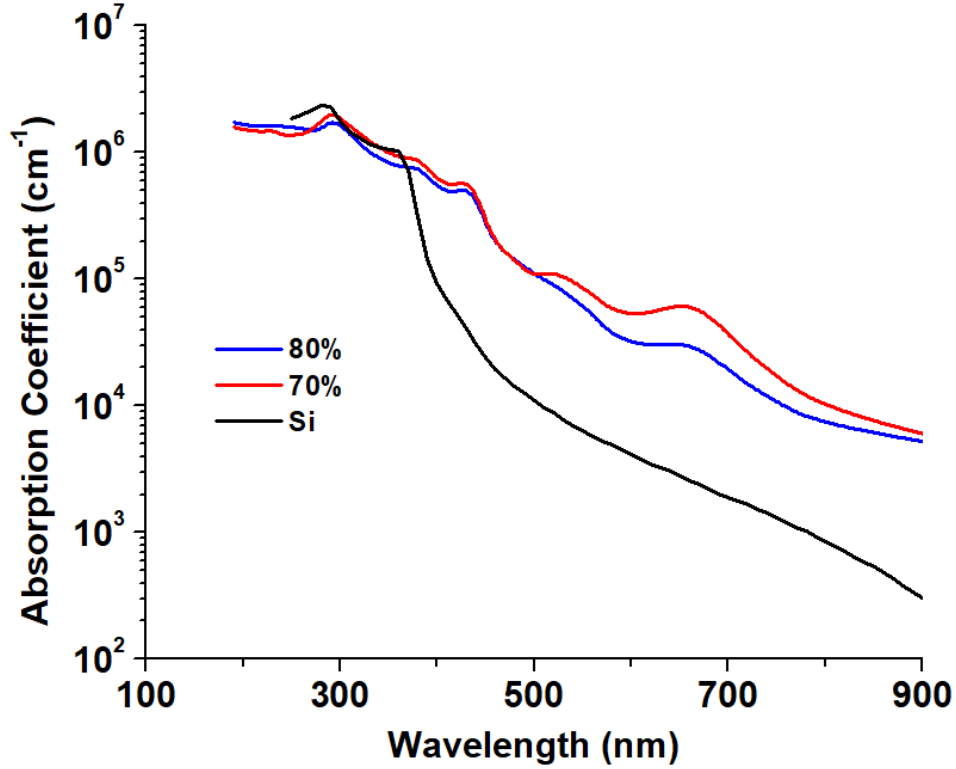


Figure 3-3: Absorption coefficient of $\text{Al}_{0.8}\text{In}_{0.2}\text{As}_y\text{Sb}_{1-y}$,³⁷ $\text{Al}_{0.7}\text{In}_{0.3}\text{As}_y\text{Sb}_{1-y}$,⁴⁸ and silicon.⁴⁹

To verify the previously measured low-noise characteristics of $\text{Al}_{0.8}\text{In}_{0.2}\text{As}_y\text{Sb}_{1-y}$, the impact ionization coefficients were extracted using the method described by Ng, *et al.*⁵⁰ This approach calculates the coefficients through gain measurements based on electron, hole, and mixed injection profiles using equations (3.1) through (3.3)

$$G(x) \propto e^{-\gamma x} \quad (3.1)$$

$$M(x) = \frac{(\alpha - \beta)e^{-(\alpha-\beta)x}}{\alpha e^{-(\alpha-\beta)w} - \beta} \quad (3.2)$$

$$M_{mix} = \frac{\int_0^w M(x)G(x) dx}{\int_0^w G(x) dx} \quad (3.3)$$

where $G(x)$ is the carrier generation rate, γ is the absorption coefficient, w is the width of the depletion region, and $M(x)$ is the gain for an electron-hole pair injected at position x . By combining these equations with gain measurements from different injection profiles as well as the measured absorption coefficient, α and β were calculated. Figure 3-4 shows gain curves under 543, 850, and 633 nm illumination, which represent approximate electron, hole, and mixed injection, respectively. The fit values from the extracted impact ionization coefficients are also shown, indicating good agreement with the results.

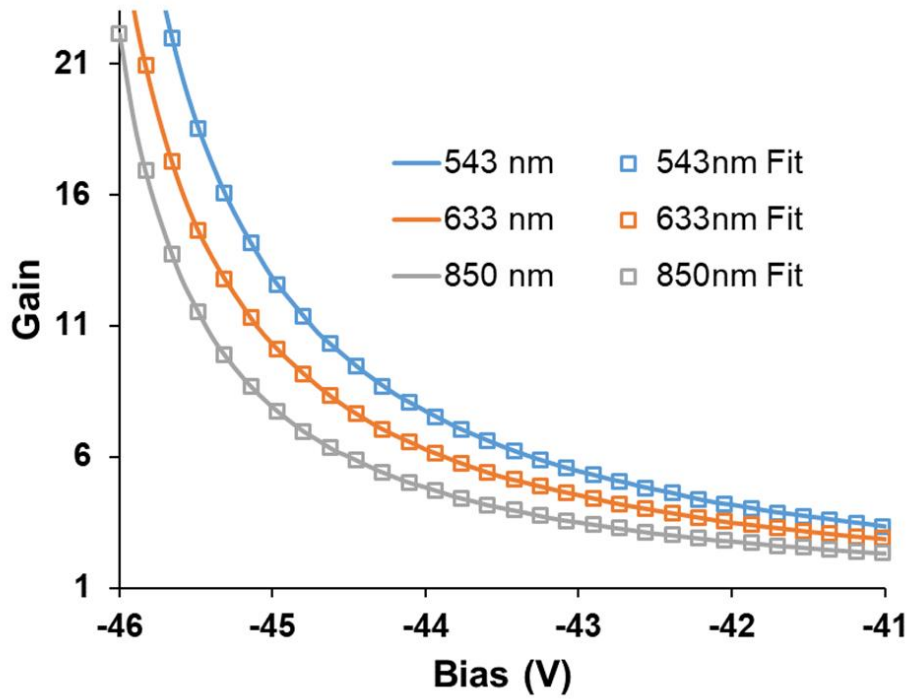


Figure 3-4: Measured gain curves under different illumination with fitted values from the impact ionization coefficients.

Figure 3-5 shows the calculated impact ionization coefficients of $\text{Al}_{0.8}\text{In}_{0.2}\text{As}_y\text{Sb}_{1-y}$ alongside those of $\text{Al}_{0.7}\text{In}_{0.3}\text{As}_y\text{Sb}_{1-y}$ ⁴⁸ for comparison. The reduced beta value for $\text{Al}_{0.8}\text{In}_{0.2}\text{As}_y\text{Sb}_{1-y}$ indicates even lower excess noise than $\text{Al}_{0.7}\text{In}_{0.3}\text{As}_y\text{Sb}_{1-y}$. This agrees with the theoretical findings that hole impact ionization in $\text{Al}_{0.7}\text{In}_{0.3}\text{As}_y\text{Sb}_{1-y}$ is suppressed by minibands

in the valence band,⁵¹ and may indicate a pronounced effect in the wider-bandgap $\text{Al}_{0.8}\text{In}_{0.2}\text{As}_y\text{Sb}_{1-y}$ material.

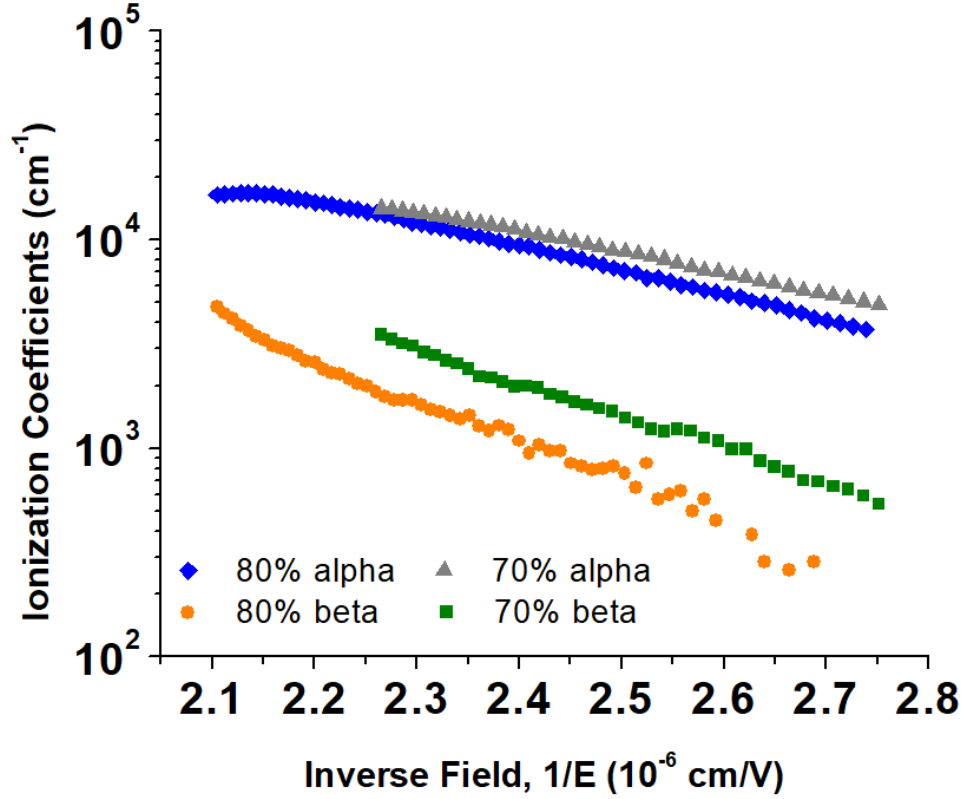


Figure 3-5: Calculated impact ionization coefficients of $\text{Al}_{0.8}\text{In}_{0.2}\text{As}_y\text{Sb}_{1-y}$ and $\text{Al}_{0.7}\text{In}_{0.3}\text{As}_y\text{Sb}_{1-y}$.

Due to the high performance measured above, equation (3.4) was used to estimate the overall sensitivity of a receiver using an $\text{Al}_{0.8}\text{In}_{0.2}\text{As}_y\text{Sb}_{1-y}$ APD:

$$P = 10 \log \left[\left(\frac{hv}{q\eta} \right) (Q \cdot 10^3) \left(\frac{\langle i^2 \rangle_c^{\frac{1}{2}}}{M} + qI_1 Q F(M) B \right) \right] \quad (3.4)$$

Here ν is the frequency, Q is the SNR, $\langle i^2 \rangle_c^{1/2}$ is the sum of the amplifier and dark current noise, I_1 is the normalized noise-bandwidth integral, and B is the bandwidth. The resulting calculation for 10 and 25 Gb/s bitrates is shown in Figure 3-6. We assume $Q = 6$ (10^{-9} bit error rate), $I_1 =$

0.5, and an amplifier input noise current of $0.8 \mu\text{A}$ at 10 Gb/s and $2.42 \mu\text{A}$ at 25 Gb/s, which were obtained from data sheets of commercially available amplifiers. We also assumed an external quantum efficiency increase to 45.6% from the addition of an approximately 99% anti-reflection (AR) coating. The maximum receiver sensitivities at 10 Gb/s and 25 Gb/s were calculated to be -31.3 dBm and -26.9 dBm, respectively. This calculation was made at an operational gain of $M = 41$. At this gain, the excess noise factor was approximately $F(M) = 3.7$.⁴⁷

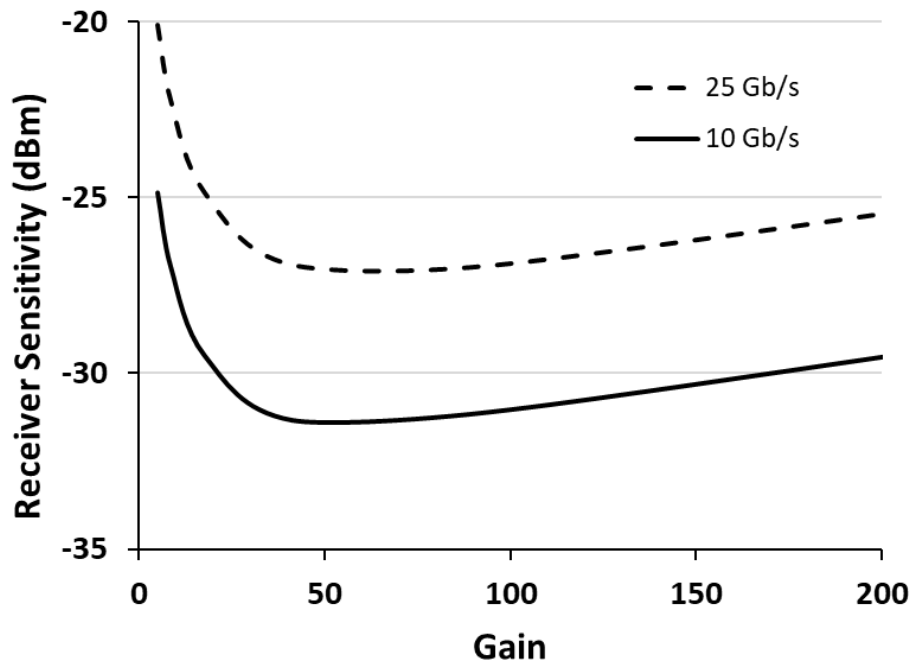


Figure 3-6: Calculated receiver sensitivity at 10 Gb/s and 25 Gb/s.

$\text{Al}_{0.8}\text{In}_{0.2}\text{As}_y\text{Sb}_{1-y}$ APDs demonstrate high gain, low dark current, low noise, and a low breakdown temperature coefficient. These characteristics in conjunction with the photoabsorption properties of $\text{Al}_{0.8}\text{In}_{0.2}\text{As}_y\text{Sb}_{1-y}$ make it an ideal materials system for highly sensitive visible and near-infrared applications. These properties also render $\text{Al}_{0.8}\text{In}_{0.2}\text{As}_y\text{Sb}_{1-y}$ a promising candidate as the high-field region of a separate absorption, charge, and multiplication (SACM) APD for longer wavelength applications.

4 $\text{Al}_x\text{In}_{1-x}\text{As}_y\text{Sb}_{1-y}$ SACM APDs for 2- μm Detection

Due to their narrow bandgaps, materials that absorb infrared light are susceptible to increased dark current. Since a high electric field is required to induce impact ionization, these materials are poorly suited for use in traditional PIN APDs where both absorption and multiplication occur in the same region. Initially, a solution to this problem was presented by introducing heterostructure APDs to spatially separate the absorption and multiplication regions.⁵² Another solution introduced a buffer layer between the regions to improve material quality and EQE.⁵³ Further improvements introduced a bandgap-grading layer between the absorber and multiplication region to allow photogenerated carriers to easily traverse the device. The resulting structure is known as the separate absorption and multiplication (SAM) APD.^{54,55} Ultimately, this grading layer was combined with a doping layer to control the electric field in the absorber and reduce tunneling dark current, which became known as the separate absorption, charge, and multiplication (SACM) APD.⁵⁶ The SACM design has revolutionized the use of APDs in infrared applications, as it has enabled multiplication gain with narrow-bandgap absorption without the negative effects of tunneling dark current.¹ It is a widely explored design for use in telecommunications and data communications, specifically with InGaAs absorbers and InP^{57–63} or InAlAs^{32,64–68} multiplication layers. In addition to III-V materials, the SACM architecture is also being used in silicon-germanium APDs.^{69–74}

Figure 4-1 illustrates how the electric field is controlled within the structure. First, the electric field builds up within the multiplication layer but is blocked from the absorber by the lightly-doped charge layer. As reverse bias is increased, and the charge layer begins to deplete,

the electric field will eventually reach through it into the absorber. This bias, known as the “punch-through” voltage, corresponds to the full depletion of the charge layer. Once the electric field has reached into the absorber, the photogenerated carriers are able to drift into the higher electric field of the multiplication layer and impact ionize, resulting in gain.

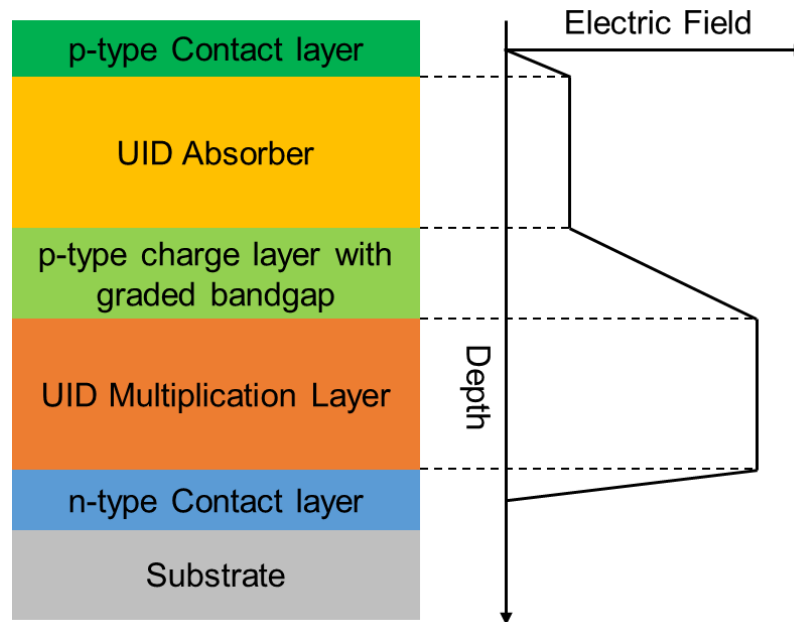


Figure 4-1: Cross section and electric field profile of an SACM APD.

Recently, with the advance of LIDAR systems in highly populated urban areas, eye safety has become a growing concern. In order to allow for longer range and higher resolution detection in the traditional telecommunication wavelength band, higher laser power must be used, which increases the potential for eye damage. To circumvent this problem, longer wavelength lasers can be employed which allow for higher power operation and thus better LIDAR imaging. The 2- μm window is ideal for LIDAR systems,⁷⁵ as it is considered eye-safe and effective in long-range detection.⁷⁶ In many LIDAR applications, highly sensitive detectors are required in order to detect the greatly attenuated optical signals reflected from distant objects.

As a result, low-noise 2- μm APDs present an ideal solution for compact, high-sensitivity LIDAR receivers.

For 2- μm APD applications, InAs,⁷⁷ InSb,⁷⁸ and HgCdTe^{79,80} have been the primary material candidates. Various superlattice^{81,82} and quantum-dot⁸³ architectures have also been demonstrated for mid-infrared applications. While these materials exhibit very low excess noise, they must be operated at cryogenic temperatures to reduce dark current. Such operating temperatures prohibit compact receiver production, as the required cryogenic system is both complex and many times larger than the detector itself.

Due to its wide bandgap tunability,^{34,39} $\text{Al}_x\text{In}_{1-x}\text{As}_y\text{Sb}_{1-y}$ is a promising candidate for SACM APDs. Compositions with lower aluminum concentrations can be used for the narrow-bandgap absorber, and compositions with higher aluminum concentrations can be used for the wide-bandgap multiplication region while maintaining lattice matching across the materials system. An SACM APD with an $\text{Al}_{0.4}\text{In}_{0.6}\text{As}_y\text{Sb}_{1-y}$ absorber and $\text{Al}_{0.7}\text{In}_{0.3}\text{As}_y\text{Sb}_{1-y}$ multiplication region was demonstrated for 1550-nm applications and exhibited low excess noise consistent with $\text{Al}_x\text{In}_{1-x}\text{As}_y\text{Sb}_{1-y}$ PIN devices.⁸⁴ The challenge in designing a 2- μm -compatible $\text{Al}_x\text{In}_{1-x}\text{As}_y\text{Sb}_{1-y}$ SACM APD was to further reduce the bandgap of the absorber while demonstrating low noise, high gain, and high temperature stability.

4.1 Device Design

Since the functionality of SACM APDs is highly dependent on controlling the electric field within the device, the 2- μm design needed to be rigorously simulated prior to crystal

growth. A difficulty in doing this for the $\text{Al}_x\text{In}_{1-x}\text{As}_y\text{Sb}_{1-y}$ materials system was that software models did not exist. I began my work by designing an $\text{Al}_x\text{In}_{1-x}\text{As}_y\text{Sb}_{1-y}$ material macro in APSYS Crosslight based on the existing model for AlGaAsSb and substituting material parameters of GaAs and GaSb for InAs and InSb, respectively. Various parameters of the model were then tested against the calculated $\text{Al}_x\text{In}_{1-x}\text{As}_y\text{Sb}_{1-y}$ bandgap energy³⁴ in order to recreate specific material compositions. The $\text{Al}_x\text{In}_{1-x}\text{As}_y\text{Sb}_{1-y}$ material macro and parameters for various compositions can be found in appendix 1.

Two 2- μm SACM APD designs were proposed, both employing an $\text{Al}_{0.3}\text{In}_{0.7}\text{As}_y\text{Sb}_{1-y}$ absorber and $\text{Al}_{0.7}\text{In}_{0.3}\text{As}_y\text{Sb}_{1-y}$ multiplication and charge layers. The first design (device A) included an intermediate-bandgap $\text{Al}_{0.5}\text{In}_{0.5}\text{As}_y\text{Sb}_{1-y}$ region as the grading layer, similar to the SAM APD design.⁵⁴ The second design (device B) included a linearly-graded region between the absorber and multiplication layers, akin to the previous $\text{Al}_x\text{In}_{1-x}\text{As}_y\text{Sb}_{1-y}$ SACM APD.⁸⁴ The epitaxial layer structure of the devices is shown in Figure 4-2, and the energy band structures of both devices at zero and -20 V bias are shown in Figure 4-3.

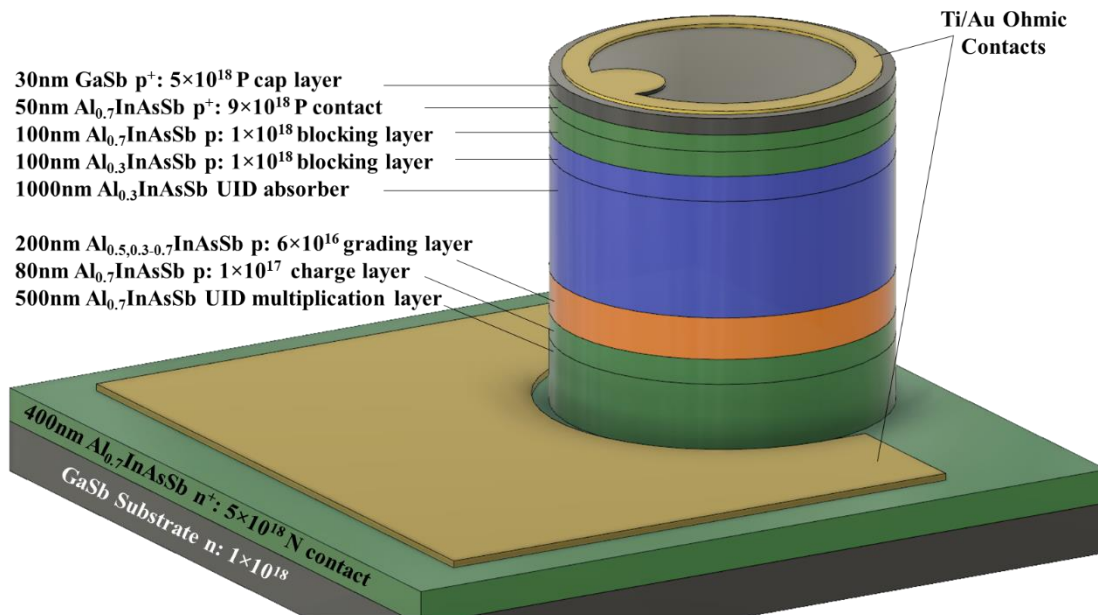


Figure 4-2: Epitaxial layer design of the $\text{Al}_x\text{In}_{1-x}\text{As}_y\text{Sb}_{1-y}$ 2- μm SACM APDs.

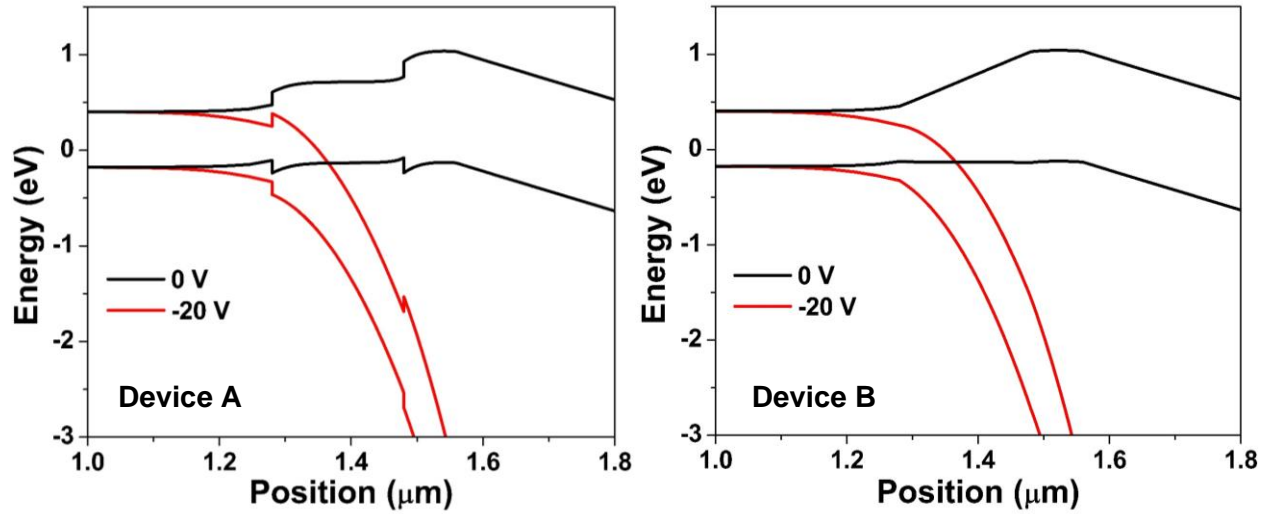


Figure 4-3: $\text{Al}_x\text{In}_{1-x}\text{As}_y\text{Sb}_{1-y}$ SACM APD energy band diagrams illustrating how the conduction band barrier is lowered with applied bias.

Due to the large conduction band offset in the $\text{Al}_x\text{In}_{1-x}\text{As}_y\text{Sb}_{1-y}$ material, special care was given to design the SACM APDs in order to avoid charge trapping in the conduction band. As a result of the abrupt band discontinuities in device A, small traps appear as the conduction band energy decreases, as illustrated in Figure 4-4 for the $\text{Al}_{0.5}\text{In}_{0.5}\text{As}_y\text{Sb}_{1-y}$ to $\text{Al}_{0.7}\text{In}_{0.3}\text{As}_y\text{Sb}_{1-y}$ interface. At higher reverse bias, a similar trap will form at the $\text{Al}_{0.3}\text{In}_{0.7}\text{As}_y\text{Sb}_{1-y}$ to $\text{Al}_{0.5}\text{In}_{0.5}\text{As}_y\text{Sb}_{1-y}$ interface. This finding led to the incorporation of light doping in the grading layers in addition to higher doping in the charge layers, ensuring that the full conduction band barrier lowers at the punch-through voltage. The advantage of device B, of course, is that there are no conduction band discontinuities, thereby removing the potential for charge trapping.

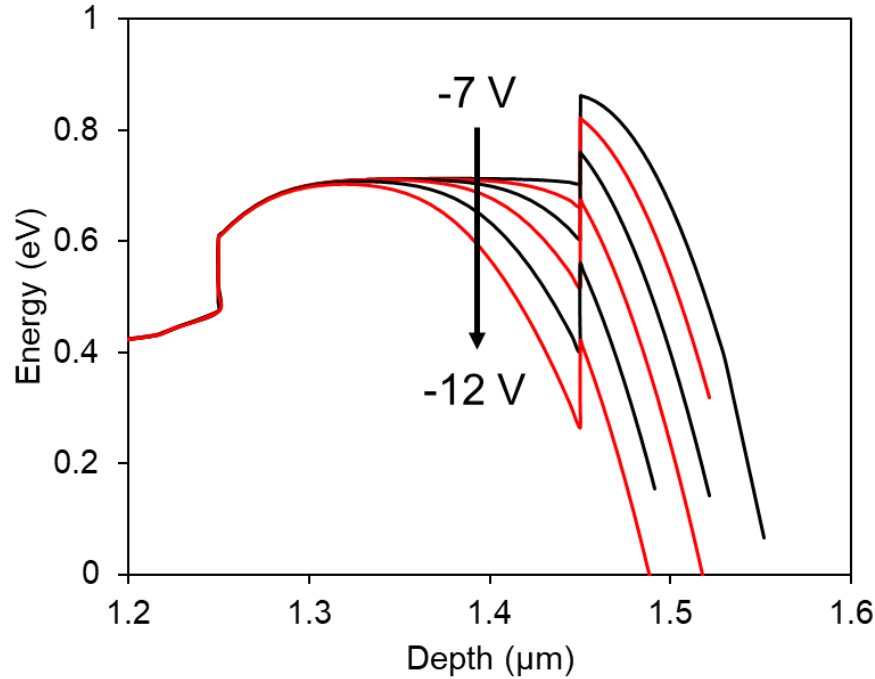


Figure 4-4: Changes in the conduction band of device A with increased reverse bias. A small barrier is present as carriers drift into the multiplication layer.

4.2 Device Characterization

Both the device designs listed above were grown by Stephen March at the University of Texas at Austin. They were fabricated at the University of Virginia using standard photolithography techniques. The device mesas were etched using reactive ion etching with inductively coupled plasma (RIE/ICP) and finished with a dilute bromine-methanol solution to smooth the sidewalls. Contacts were deposited via electron-beam evaporation, and the devices were passivated with SU-8 epoxy photoresist.

For SACM APDs, it is important to ascertain the punch-through voltage, since device parameters are characterized above this operating point. A capacitance-voltage (C-V) curve indicates the punch through by a sharp drop in capacitance, since capacitance is described by:

$$C = \frac{\epsilon A}{d} \quad (4.1)$$

where ϵ is the dielectric constant of the material, A is the area and d is the thickness. At punch through, the charge layer has fully depleted, effectively increasing the full depletion width, d , of the device and lowering the capacitance. Figure 4-5 shows the C-V curves for devices A and B, indicating punch-through voltages of approximately -27 and -23 V, respectively.

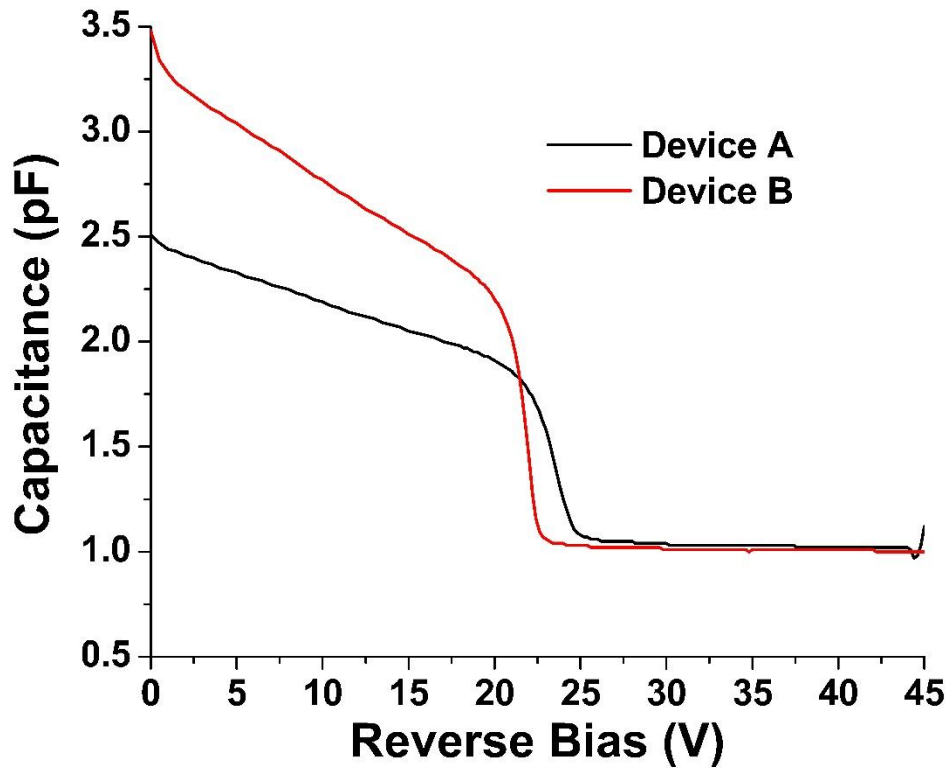


Figure 4-5: C-V curves for both 2- μm SACM APDs measured from 150- μm -diameter devices.

The EQE of each device was measured based on the observed punch-through voltage. Figure 4-6 indicates that at 2 μm , the EQE for device B is approximately 20%, while device A is slightly lower. The spectral cutoff for both devices is $> 2.1 \mu\text{m}$. Furthermore, due to the absence of an AR coating on either device, it is estimated that with the addition of a 1%-reflectivity

coating, the 20% EQE could be increased to approximately 30% based on the reported reflectivity of GaSb at 2 μm .⁸⁵

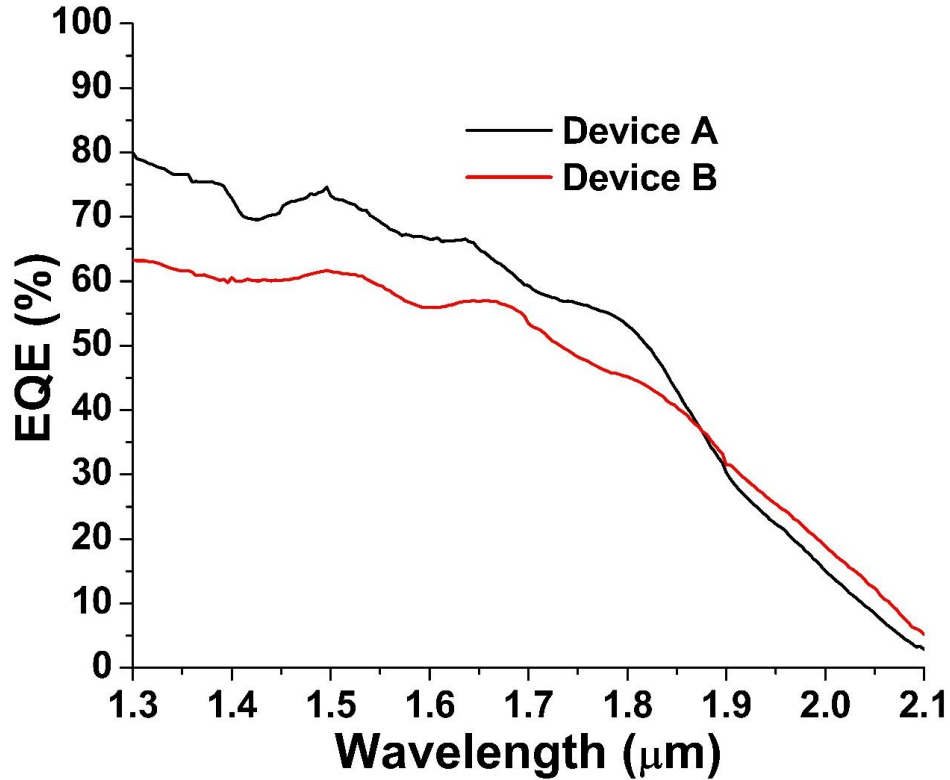


Figure 4-6: EQE of both 2- μm SACM APDs without AR enhancement measured from 200- μm -diameter devices.

Although the punch-through voltage indicates that the charge layer is fully depleted, this does not mean the electric field magnitude in the multiplication region is at the impact ionization threshold. In fact, the electric field could be above or below this threshold, meaning $M > 1$ or $M = 1$ at the punch-through voltage, respectively. In the former case, there is an excess of electric field in the multiplication region, meaning that there is significant impact ionization at punch-through and the true unity gain is at a slightly lower reverse bias. In the latter case, higher electric field is required in the multiplication region before impact ionization can occur, i.e., unity gain is at a higher reverse bias than the punch-through voltage. For this reason, the unity gain point must be determined by another factor that scales with the gain, the excess noise. In

this work, the unity gain point was determined by computationally fitting the measured excess noise to the change in photocurrent.⁸⁶

Figure 4-7 shows the current-voltage characteristics for each device under 2- μm illumination. The gain calculated in relation to the punch-through voltage was adjusted according to the excess noise fit and included in the figure. As shown in Figure 4-8, dark current scales linearly with device diameter, indicating that surface leakage is the limiting factor.

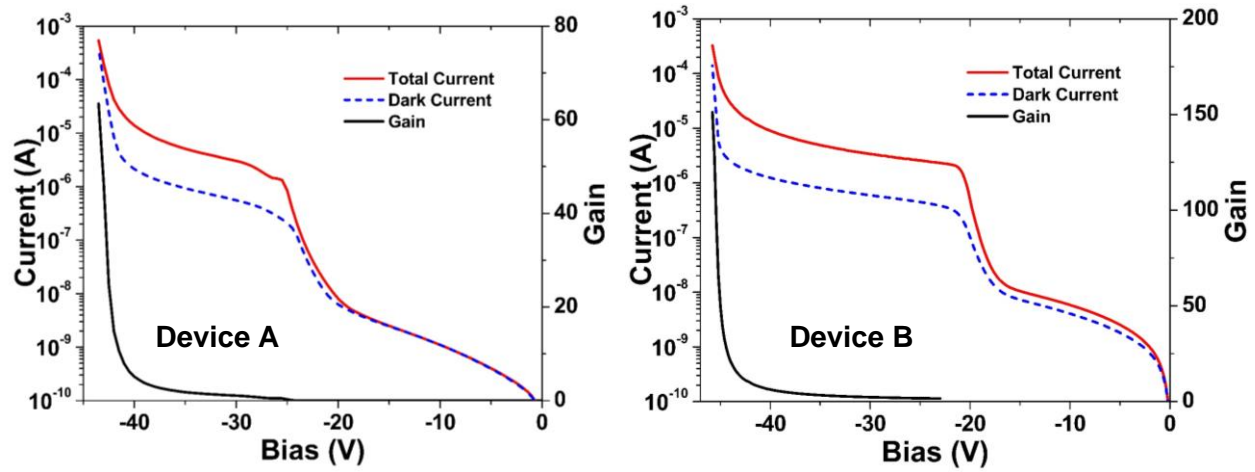


Figure 4-7: I-V and gain curves for device A and B measured from 80- μm -diameter devices at room temperature under 2- μm illumination.

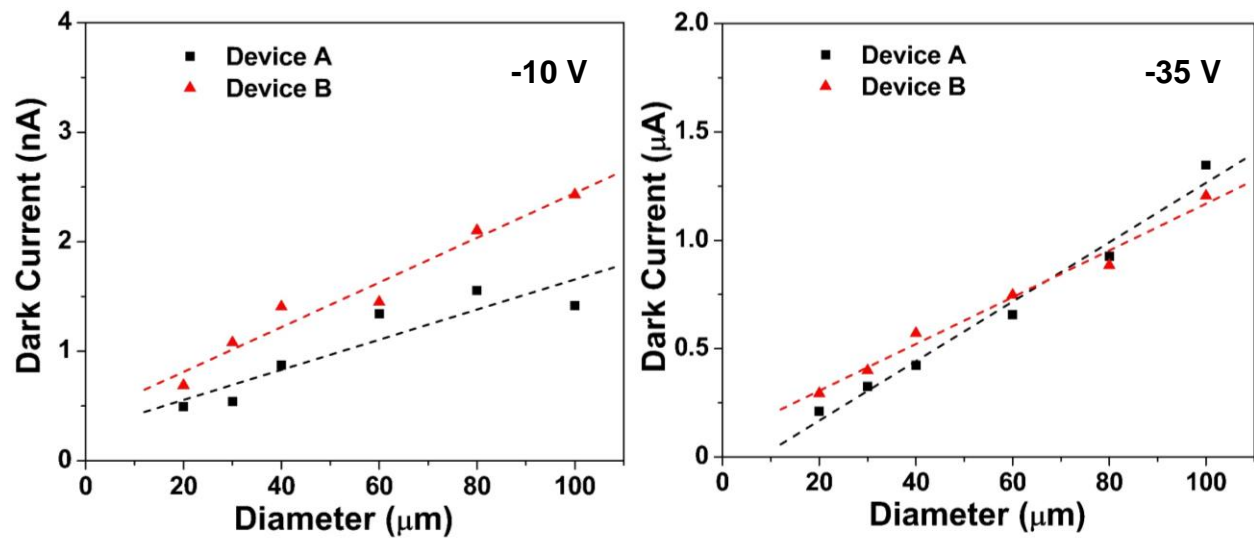


Figure 4-8: Dark current as a function of device diameter for each device at 10 V (left) and 35 V (right) reverse bias. Measurements are at room temperature. Linear fits are shown, indicating that surface leakage dominates.

Figure 4-9 shows the excess noise of both devices as a function of gain alongside plots of the excess noise for k factors ranging from 0 to 0.1 using the local-field model.¹⁵ Under 2- μm illumination, both designs exhibit extremely low excess noise, characterized by $k \approx 0.01$. This is consistent with previously measured $\text{Al}_x\text{In}_{1-x}\text{As}_y\text{Sb}_{1-y}$ devices^{35,87} and comparable to that of silicon in the visible and near infrared.¹⁶

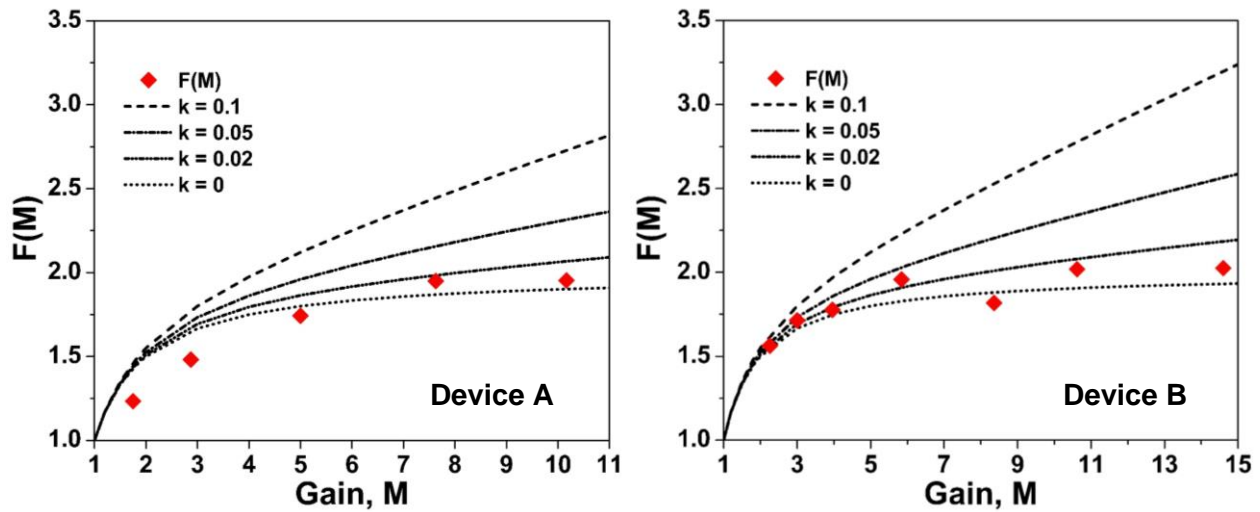


Figure 4-9: Excess noise of device A and B measured at room temperature under 2- μm illumination.

In order to accurately compare the dark current to that of HgCdTe, the dark current density (J_{dark}) of each device was measured as a function of temperature from 180 to 320 K in increments of 20 K. State-of-the-art HgCdTe detectors used for 2- μm and mid-infrared detection have $J_{\text{dark}} = 3 \times 10^{-4} \text{ A/cm}^2$ at $M = 10$ while operating at 125 K.⁷⁹ Figure 4-10 indicates that at 240 K, the $\text{Al}_x\text{In}_{1-x}\text{As}_y\text{Sb}_{1-y}$ SACM APDs do not reach this J_{dark} magnitude until after the punch-through voltage. Furthermore, at 180 K, the J_{dark} of these devices only reaches this magnitude near the avalanche breakdown voltage. Based on the measurements used for the $\Delta V_{\text{bd}}/\Delta T$ characterization below, device B shows comparable J_{dark} to HgCdTe between 200 and 220 K. The activation energy of each device was extracted from the Figure 4-10 measurements at -10 V (below punch-through) and -35 V (above punch-through) for each device. At these respective

biases, they are approximately 0.31 eV and 0.22 eV for device A and 0.23 eV and 0.26 eV for device B.

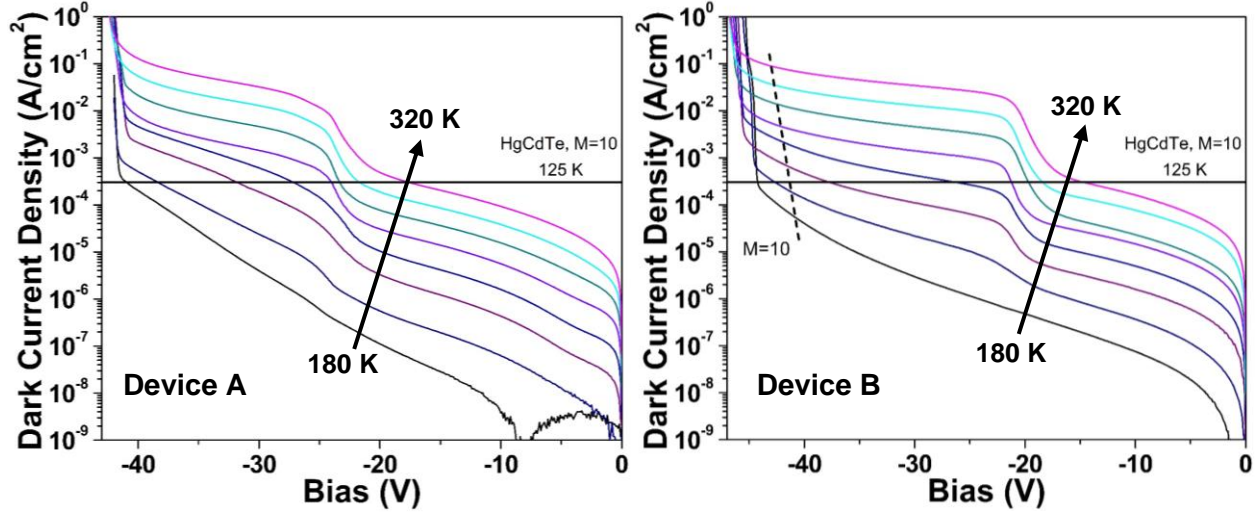


Figure 4-10: Dark current density of device A and B as a function of temperature. That of state-of-the-art HgCdTe APDs is also included.⁷⁹

As discussed in section 2, APDs of common materials systems have been characterized by the temperature dependence of the avalanche breakdown voltage.⁴⁰ This is an important figure of merit for devices operating under varying ambient conditions, as a lower breakdown voltage temperature coefficient $\Delta V_{bd}/\Delta T$ is characteristic of a device requiring less temperature feedback control. For SACM architectures, this value is best plotted as a function of the ratio of the full depletion width to the multiplication layer thickness, since the device thickness can no longer be represented by the multiplication layer alone. The $\Delta V_{bd}/\Delta T$ of device B has been characterized under 2- μm illumination from 240 to 300 K. Figure 4-11 shows this work alongside various other SAM APDs as a function of the depletion-width-multiplication-layer-thickness ratio. For a ratio of 3.56 (this work), $\text{Al}_x\text{In}_{1-x}\text{As}_y\text{Sb}_{1-y}$ displays a $\Delta V_{bd}/\Delta T$ less than two-fifths that of InAlAs ^{40,68,88,89} and less than one-sixth that of InP .^{40,90,91}

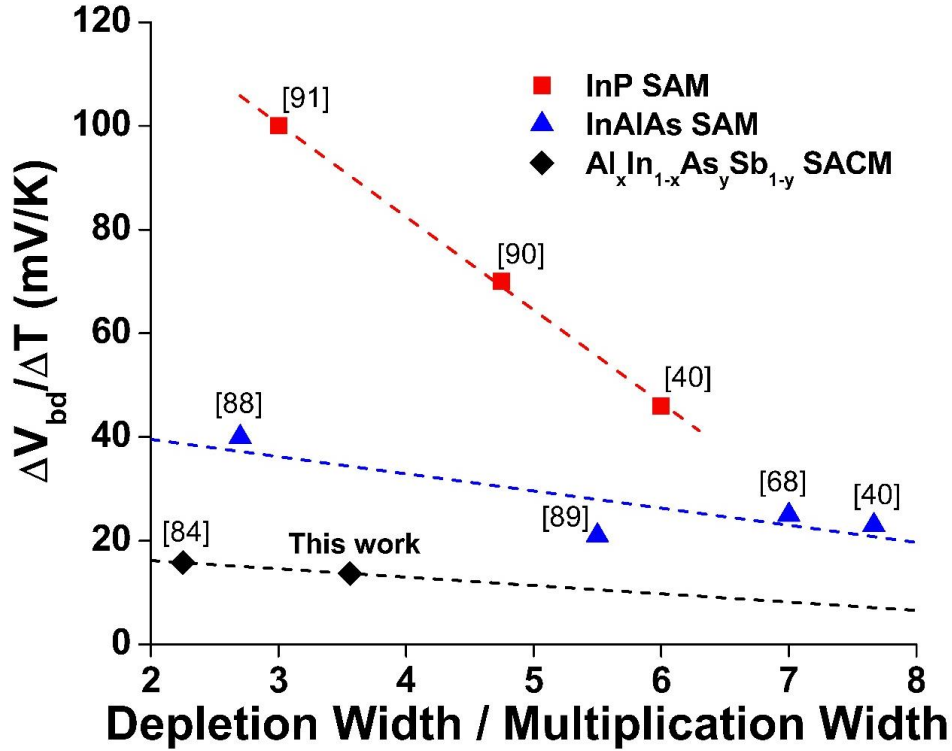


Figure 4-11: $\Delta V_{bd}/\Delta T$ as a function of depletion width / multiplication layer thickness for InP SAM (red squares), InAlAs SAM (blue triangles), and $\text{Al}_x\text{In}_{1-x}\text{As}_y\text{Sb}_{1-y}$ SACM (black diamonds) APDs. A linear best-fit curve is included for each materials system. References are included above data points.

In this chapter, I have demonstrated low-noise, 2- μm SACM APDs based on the $\text{Al}_x\text{In}_{1-x}\text{As}_y\text{Sb}_{1-y}$ materials system with comparable J_{dark} to HgCdTe at a 75 to 95 K higher operating temperature.⁷⁹ Under 2- μm illumination, gains > 100 and external quantum efficiencies of ~20% at punch through without AR enhancement have been achieved. The low-noise characteristics, temperature stability, and bandgap tunability of the $\text{Al}_x\text{In}_{1-x}\text{As}_y\text{Sb}_{1-y}$ materials system make it a promising candidate for highly sensitive detectors across the near and mid-infrared spectrum with less dependence on cryogenic cooling than other materials systems traditionally used for mid-infrared detection. These characteristics are highly desirable for LIDAR, night vision, and thermal imaging applications in scenarios where bulky cryogenic systems are impractical.

5 $\text{Al}_x\text{In}_{1-x}\text{As}_y\text{Sb}_{1-y}$ Staircase APDs

Before the advent of solid-state APDs, photomultiplier tubes (PMTs) served as the primary means for detecting and amplifying optical signals. These devices operate by converting incident photons to electrons via a photocathode and multiplying these electrons through a series of dynodes onto a final anode. The arrival of an electron triggers the release of additional electrons by each dynode, resulting in high gain which scales with the number of dynodes and the voltage across them. PMTs are still used in some applications, primarily as a result of their high sensitivity. Unfortunately, PMTs are bulky and fragile and operate at hundreds or even thousands of volts, making them non-ideal or prohibitive in many applications.

In 1982, Federico Capasso and his collaborators proposed a novel APD model mimicking the functionality of a PMT.²⁹ As shown in Figure 5-1 (a), this design used a series of discontinuities within the band structure known as “steps” to mirror the functionality of the PMT dynodes.⁹² At sufficient reverse bias, the graded bandgap regions flatten, allowing photogenerated carriers to drift across the discontinuities, as illustrated in Figure 5-1 (b).²⁹ The abrupt energy change at the discontinuities, ΔE , induces impact ionization of the photogenerated carriers at each step. The staircase APD as it became known, hailed as a solid-state replacement for the PMT, offering the lower-bias gain of a traditional APD with greatly reduced excess noise due to spatially-deterministic single-carrier impact ionization.³⁰ Ideally, each carrier would impact ionize at each step, but in practice, impact ionization at each step is represented by a probability, P , resulting in the total gain for an n -step staircase given by

$$M = (1 + P)^n \quad (5.1)$$

From this equation it is clear that if all carriers impact ionize, 1, 2, and 3-step staircase APDs would provide gains of 2, 4, and 8, respectively.

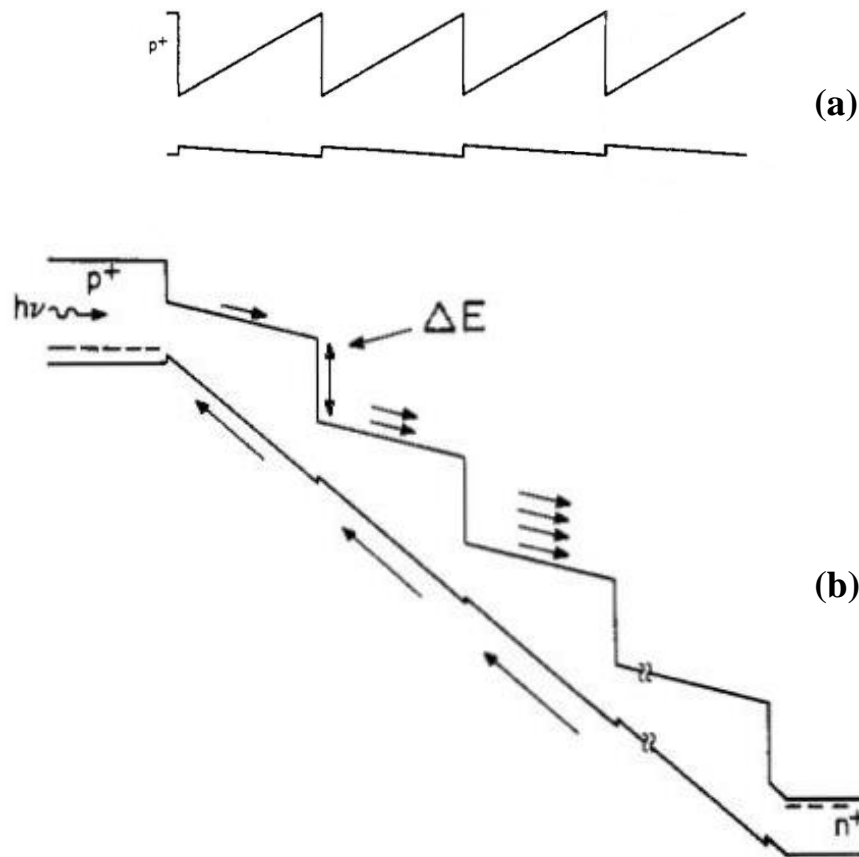


Figure 5-1: Band diagram of a staircase APD under zero bias (a) and low reverse bias (b).²⁹

One of the many challenges in designing a staircase APD lay in identifying a material system that offered band discontinuities adequate to induce carrier impact ionization. Not only is the magnitude of ΔE important, but the ratio of ΔE to the narrow-bandgap energy at the bottom of the step is also critical. Capasso originally concentrated on the use of AlGaAs/GaAs, but this combination proved unable to provide band discontinuities with sufficient ΔE for impact ionization compared to the bandgap of GaAs.^{93,94} Other materials systems were also investigated

but were unable to demonstrate gain resulting from the device band structure rather than traditional impact ionization at higher bias.^{95,96}

Finally, in 2016, the first successful one-step staircase APD was demonstrated in the $\text{Al}_x\text{In}_{1-x}\text{As}_y\text{Sb}_{1-y}$ materials system, as it was able to provide sufficient ΔE in the conduction band to induce impact ionization.⁹⁷ The photoresponse of the staircase structure was compared to that of a simple PIN “control” structure of the same wide-bandgap material, resulting in a photocurrent ratio, or gain, of 1.8 ± 0.2 . By equation (5.1), this gain corresponds to an average impact ionization probability of 0.8. At that time, staircase APDs with $n > 1$ were unsuccessful, likely as a result of unaccounted-for background doping.

5.1 Multi-Step Staircase APDs

My research sought to demonstrate multi-step staircase APDs, both to further prove the capability of the $\text{Al}_x\text{In}_{1-x}\text{As}_y\text{Sb}_{1-y}$ materials system for band engineering applications and to demonstrate the viability of staircase APDs. While a promising proof of concept, a 1-step staircase APD is less practical than a $n > 1$ device, as higher gains naturally increase sensitivity.

After multiple iterations of growth, fabrication and testing, we demonstrated the first 2 and 3-step staircase APDs. The band structures of these devices are shown in Figure 5-2 alongside the 1-step design.⁹⁷ As before, these devices were characterized by comparing their photocurrent to that of control PIN structures with identical layer thicknesses but without the compositionally graded steps. Care was taken in the epitaxial design to allow for ~100% optical absorption prior to the staircase region, as absorption in the narrow-bandgap region of the steps could indicate an increased photocurrent without multiplication gain. All staircase devices

included a 30-nm p-type GaSb cap layer, a 100-nm p-type $\text{Al}_{0.7}\text{In}_{0.3}\text{As}_y\text{Sb}_{1-y}$ contact layer, and a 503-nm undoped $\text{Al}_{0.7}\text{In}_{0.3}\text{As}_y\text{Sb}_{1-y}$ absorber before the staircase region, ensuring full photoabsorption. The absorption characteristics of the staircase devices were determined through spectroscopic ellipsometry measurements, as shown in Figure 5-3. These calculations reveal that > 99.99% of the incident 543-nm light is absorbed before the staircase region. Additionally, in order to mitigate differences in surface reflectivity, the p-type GaSb capping layer was not modified after growth.

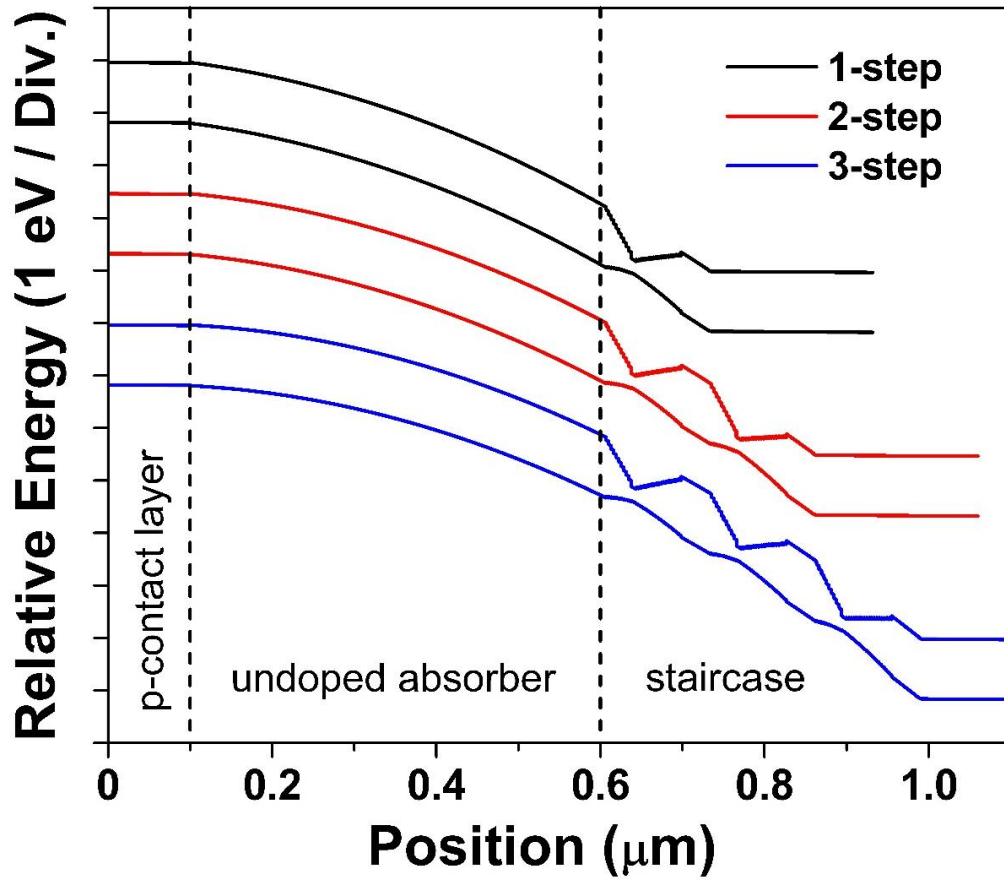


Figure 5-2: 1, 2, and 3-step staircase band structures under 4, 5, and 6 V reverse bias, respectively.

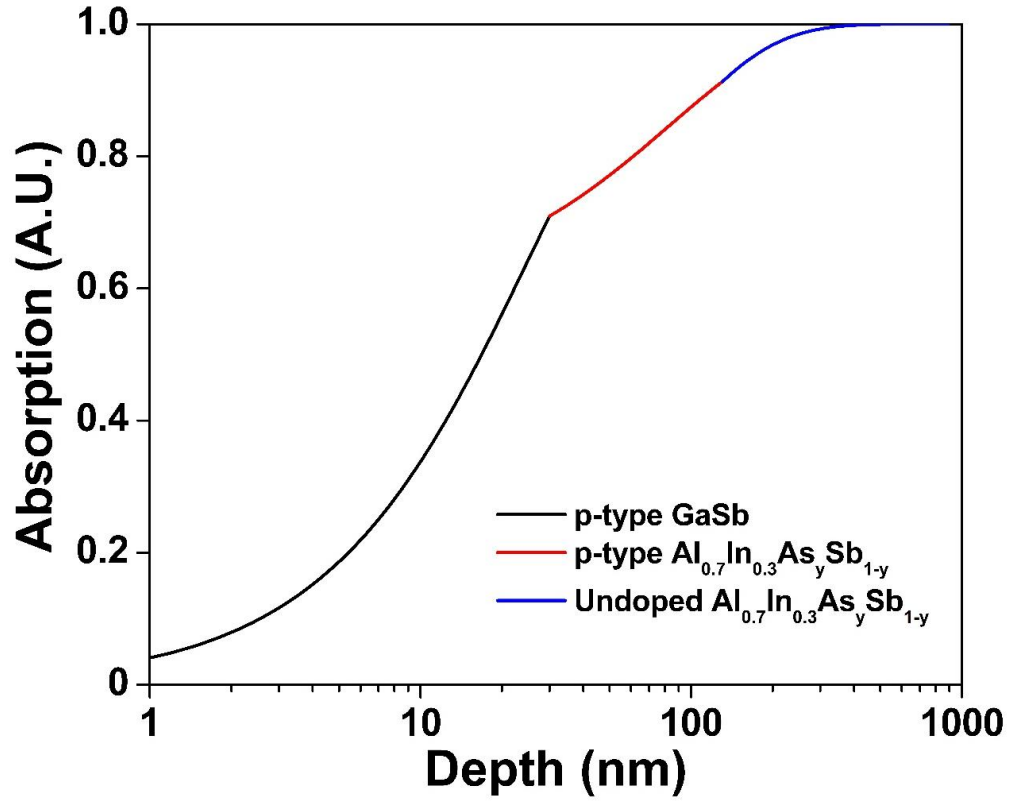


Figure 5-3: 543-nm photoabsorption within the staircase APD layer structure.

The I-V curve comparison of a 2-step staircase to its control PIN device is shown in Figure 5-4. The photoresponse of the control device remains relatively constant, as the applied bias is insufficient to induce impact ionization. From this plot, it can be seen that the staircase turn-on voltage is between -1 and -2 V, and traditional impact ionization sets in between -5 and -6 V.

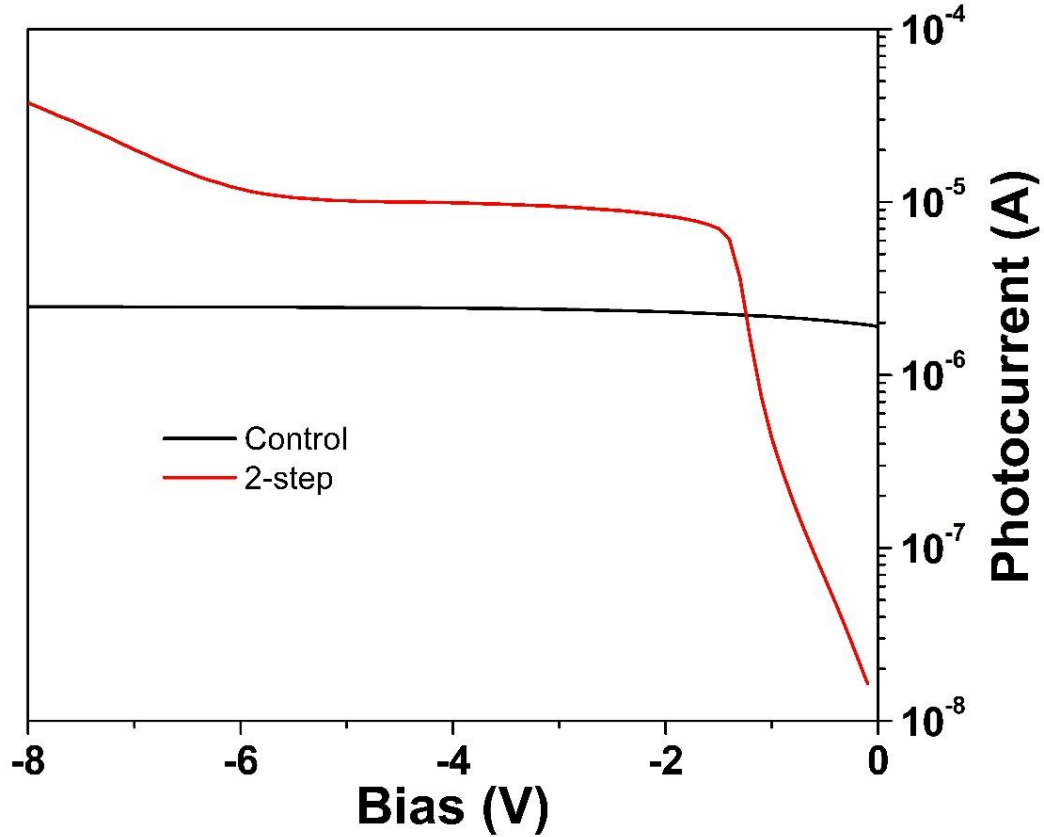


Figure 5-4: Photocurrent of 2-step staircase and 2-step control APDs under 543-nm illumination.

Figure 5-5 shows the gain curve comparison of the 1,⁹⁷ 2, and 3-step staircase APDs, which is the ratio of the staircase APD photocurrent to the control device photocurrent. These curves indicate the turn-on voltage as well as the onset of tunneling gain, as indicated by the rapid gain increase at higher reverse bias. By equation (5.1), the probability of impact ionization can be calculated for each staircase APD, as shown in Figure 5-6.

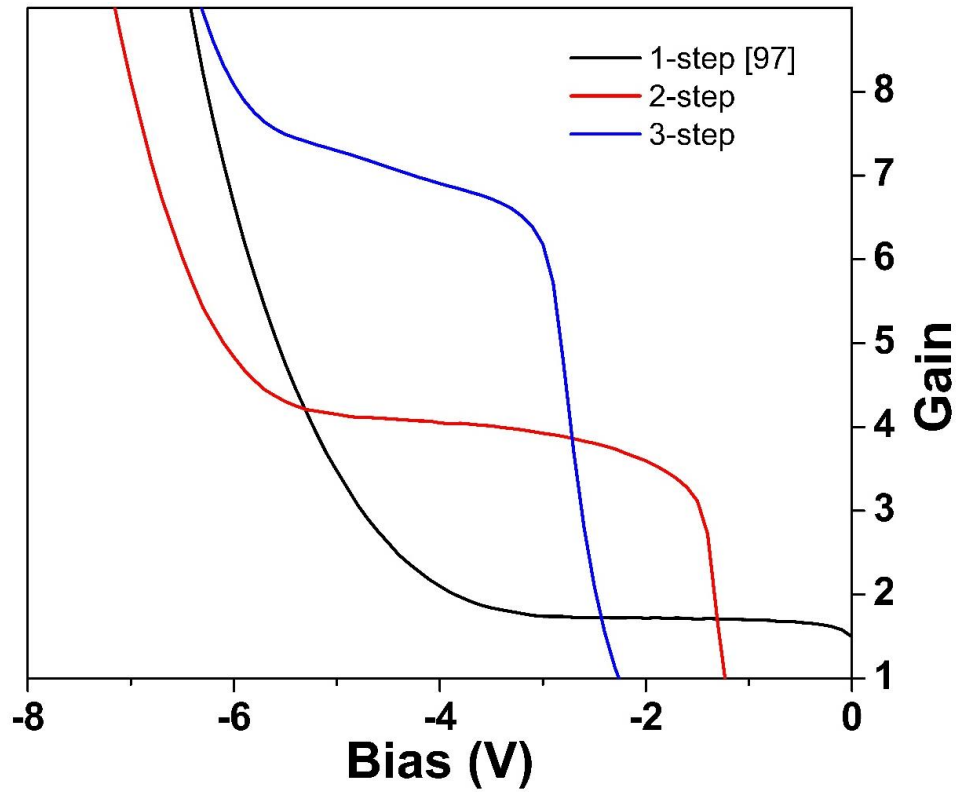


Figure 5-5: Gain curve comparison of 1, 2, and 3-step staircase APDs under 543-nm illumination.

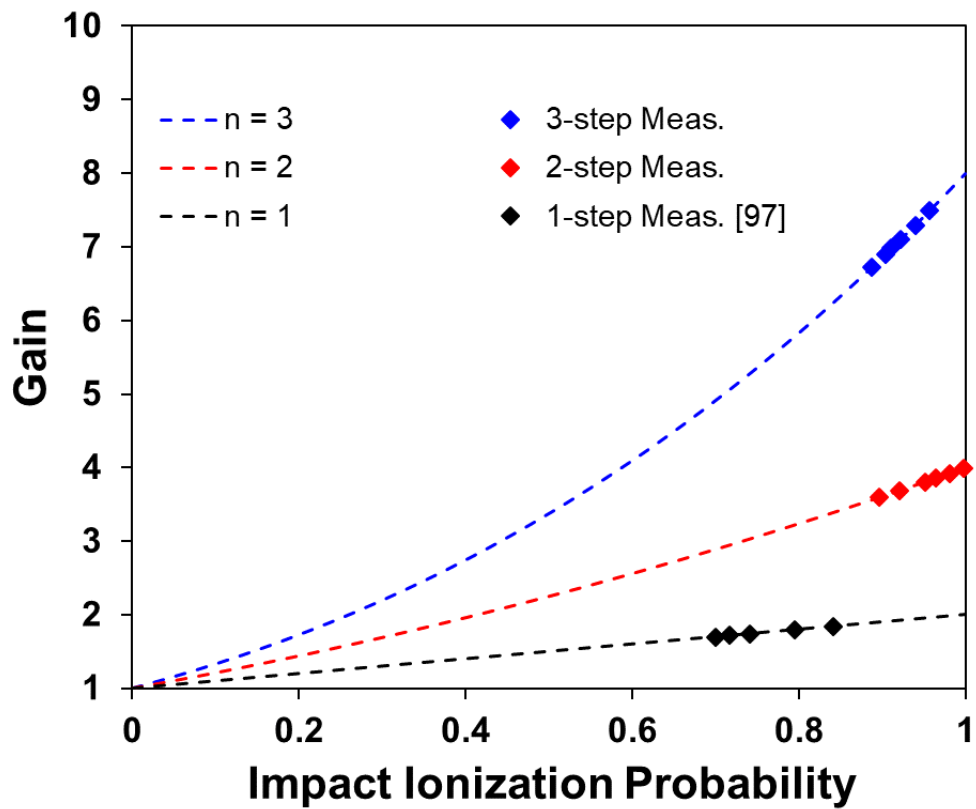


Figure 5-6: Comparison of impact ionization probability for 1, 2, and 3-step staircase APDs based on equation (5.1).

Figure 5-7 shows the C-V curves of the 2 and 3-step staircase APDs. The rapid capacitance decrease as the devices reach their turn-on voltages is characteristic of device depletion. However, as reverse bias is increased above the turn-on voltage, the capacitance increases again. This is likely due to charge trapping within the steps, finally to be relieved at higher bias with the onset of band-to-band tunneling. This behavior suggests a complex interaction between background doping and carrier transport within staircase devices, which will be the subject of future study.

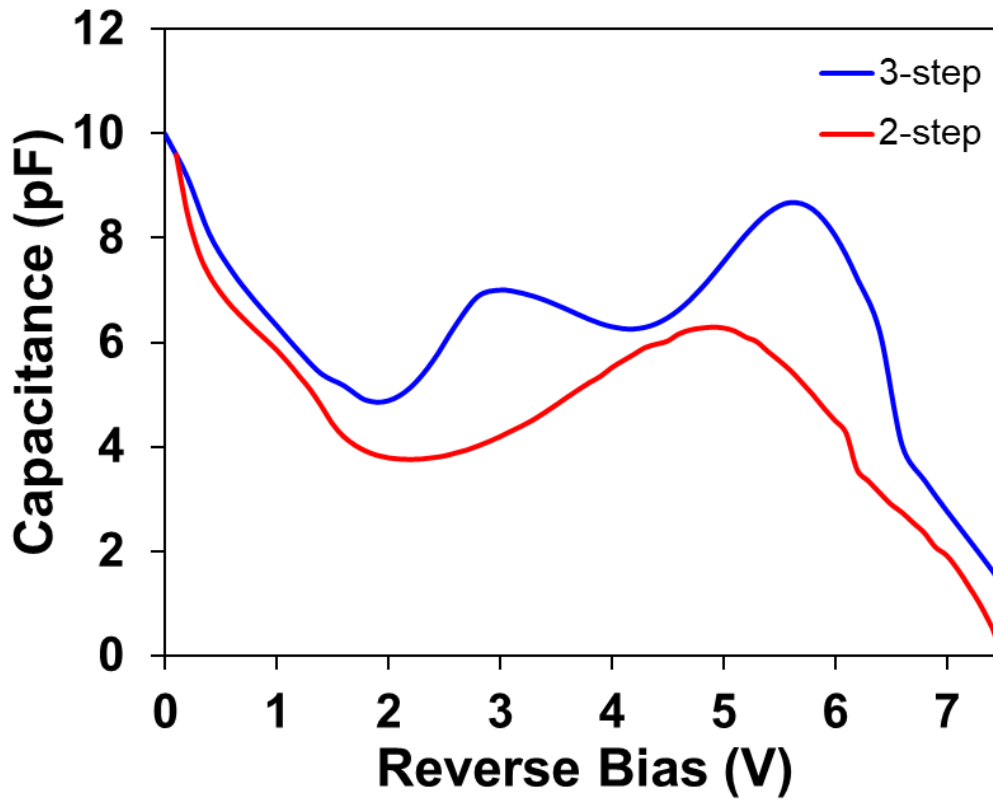


Figure 5-7: C-V curves for 2 and 3-step staircase APDs.

The dark current density (J_{dark}) of the 2 and 3-step staircase APDs was characterized as a function of temperature in 20-K increments in order to determine the onset of band-to-band tunneling within the devices. Figure 5-8 indicates that for both the 2-step and 3-step devices, band-to-band tunneling begins between -5 and -6 V, which is consistent with the gain curves in

Figure 5-5. The temperature dependent J_{dark} characteristics of the 1-step staircase APD are reported elsewhere.⁹⁷

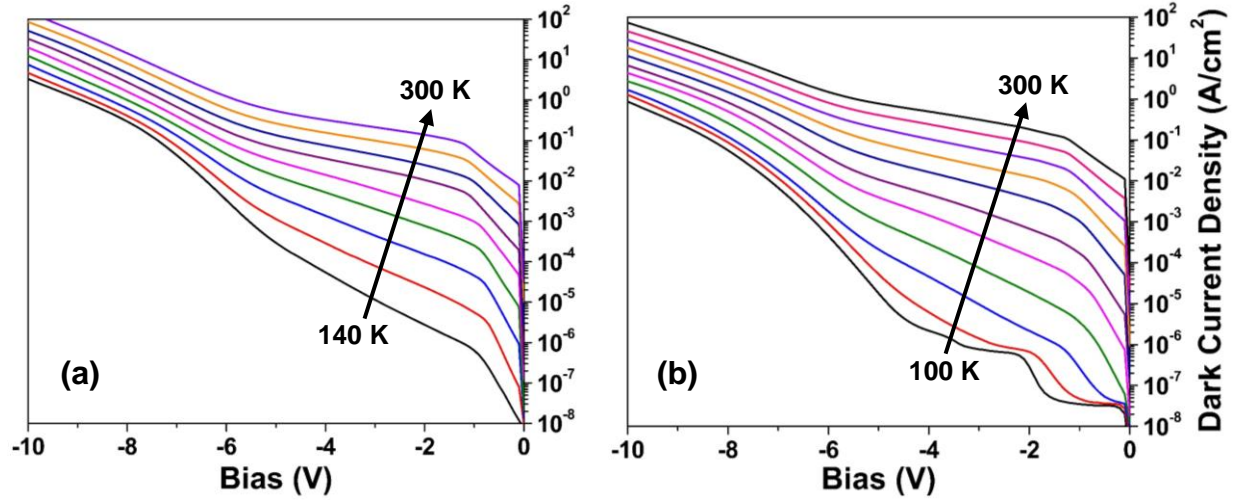


Figure 5-8: Dark current density of 2-step (a) and 3-step (b) staircase APDs as a function of temperature.

The table below summarizes the performance characteristics of the staircase APDs.

Staircase APD characteristics

n -step device	Gain	Impact ionization probability	Turn-on V (approx.)	Tunneling V (approx.)
1 ⁹⁷	1.6 - 1.8	~ 70 - 84%	-0.1 V	-3.5 V
2	3.6 - 4	~ 90 - 100%	-2 V	-5.2 V
3	6.7- 7.6	~ 83 - 96%	-3 V	-5.7 V

5.2 Improved Dark Current

Due to the presence of a narrow-bandgap region at the base of the step, staircase APDs are susceptible to band-to-band tunneling and high dark current. This is observed in our designs as a result of the 0%-Al InAlAs region.⁹⁷ In the beginning of their operating range, the 1, 2, and

3-step staircase APDs have shown dark current densities of approximately 0.01, 0.12, and 0.27 A/cm² at room temperature, respectively.

Wider-bandgap regions at the bottom of the step would undoubtedly reduce this high dark current. This improvement will, however, reduce the ΔE across the step, thereby lowering the impact ionization probability. Through extensive modeling at the University of Texas at Austin, it has been predicted that the widest permissible narrow-bandgap material is $\text{Al}_{0.13}\text{In}_{0.87}\text{As}_y\text{Sb}_{1-y}$, corresponding to $\Delta E = 0.775$ eV. This means that fully graded steps from $x = 0.7$ to 0 are perhaps unnecessary for inducing impact ionization.

To test this theory, a 1-step device with an $\text{Al}_{0.07}\text{In}_{0.93}\text{As}_y\text{Sb}_{1-y}$ narrow-bandgap region was grown and fabricated. From the wide-bandgap $\text{Al}_{0.7}\text{In}_{0.3}\text{As}_y\text{Sb}_{1-y}$ to the bottom of the step corresponds to $\Delta E = 0.839$ eV. Simulations suggest that this design should have an impact ionization probability of approximately 80%. While tests failed to produce measurable gain, this was likely the result of misplaced doping at the bottom of the step. However, this device indicated several performance improvements over the original 1-step design. First, the onset of band-to-band tunneling was delayed until approximately -7 V bias compared to approximately -3.5 V for the original design.⁹⁷ Secondly, as shown in Figure 5-9, the J_{dark} was also improved to approximately 20 to 80 times lower than the original 1-step device at room temperature between -0.1 and -2.8 V bias.⁹⁷

The J_{dark} of this design was also characterized as a function of temperature in 20-K increments, as shown in Figure 5-10. This design shows a marked improvement in dark current density at all temperature ranges compared to the original 1-step staircase design.⁹⁷

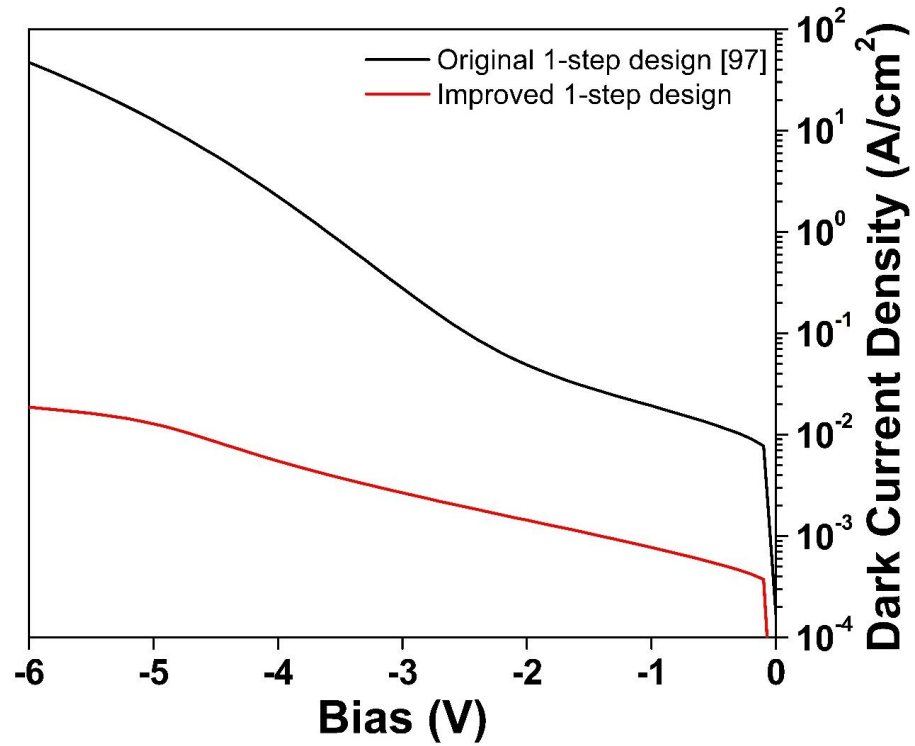


Figure 5-9: Room-temperature dark current density comparison of 1-step staircase APD designs.

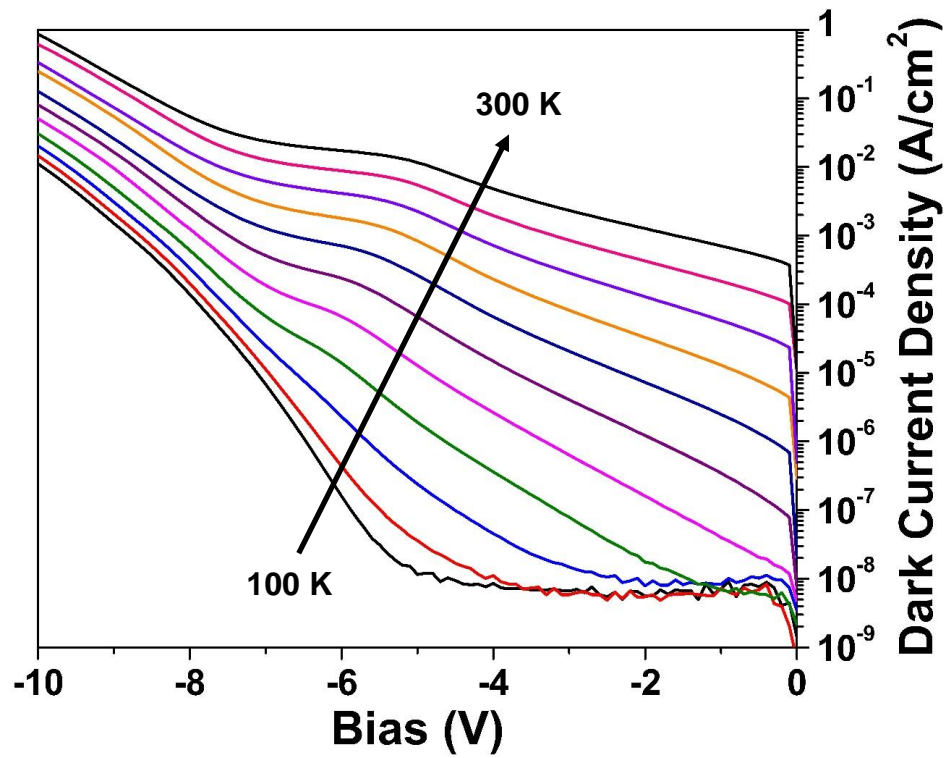


Figure 5-10: Dark current density of a 1-step staircase design with a 7%-Al narrow-bandgap region as a function of temperature.

5.3 Staircase APD Noise

By design, staircase APDs are intended to only cause the impact ionization of electrons.

With this in mind, k would intuitively be zero and $F(M)$ should reduce to

$$F(M) = 2 - \frac{1}{M} \quad (5.2)$$

meaning that for very high gain, the excess noise factor will approach 2. However, the excess noise is predicted to be much more complex than that of an APD with $k = 0$, as the APD structure has fundamentally changed.³⁰ It is necessary to consider the statistics behind the impact ionization at the steps to uncover the true nature of staircase APD noise.

Capasso's theory suggested that the excess noise should be

$$F(n, \delta) = 1 + \frac{\delta[1 - (2 - \delta)^{-n}]}{(2 - \delta)} \quad (5.3)$$

where n is the number of steps and δ is the portion of electrons that do not impact ionize.³⁰ In terms of the impact ionization probability, P , the excess noise can be expressed as

$$F(n, P) = 1 + \left(\frac{1 - P}{1 + P} \right) [1 - (1 + P)^{-n}] \quad (5.4)$$

which is the same result.⁹⁸ Taking the impact ionization probability into account, additional theory suggests the excess noise factor could be rewritten as

$$F(n, M) = M^{-1} + 2M^{-\frac{1}{n}} - 2M^{-1-\frac{1}{n}} \quad (5.5)$$

where M is the mean gain from the total number of steps (n).¹⁴

Calculating the excess noise from equation (5.5) for the 1,⁹⁷ 2, and 3-step staircase APDs and plotting as a function of gain yields Figure 5-11, which indicates that in each case, the excess noise factor is slightly > 1 . Furthermore, by using these excess noise values and solving equation (5.4) for P , the total impact ionization probability of our staircase APDs can be calculated, as shown in Figure 5-12.

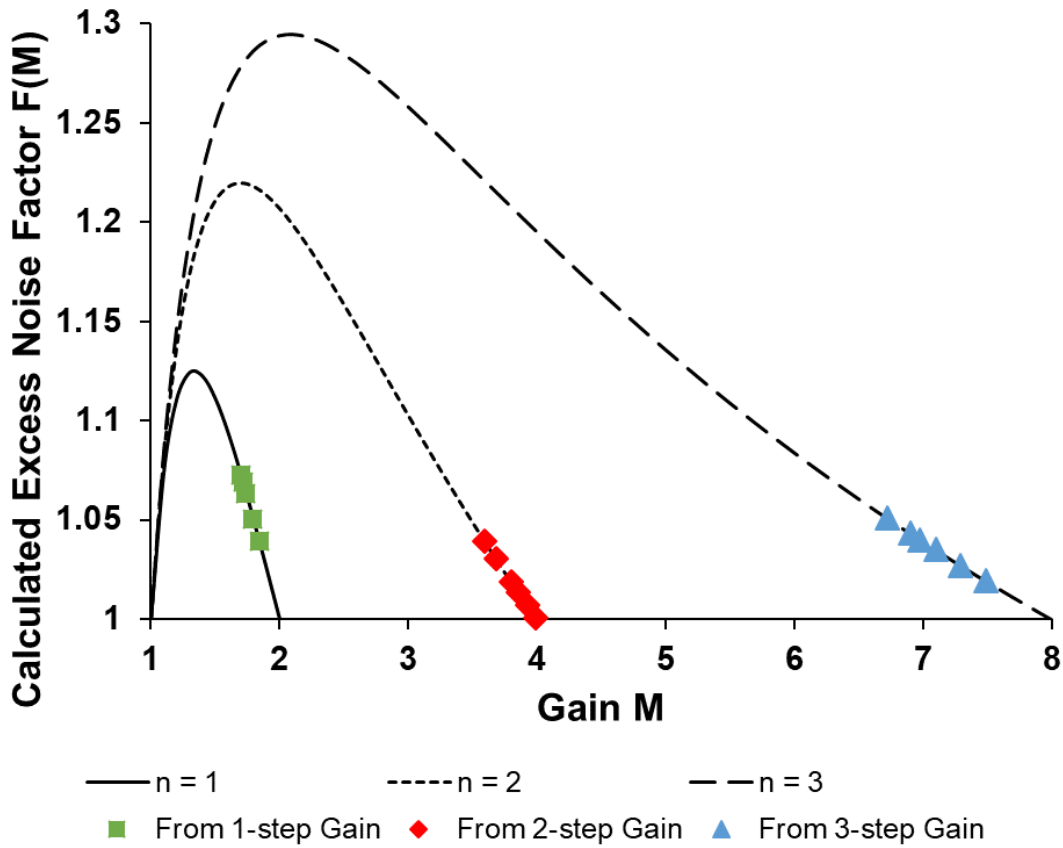


Figure 5-11: Calculated excess noise factor of 1, 2, and 3-step staircase APDs as a function of gain.

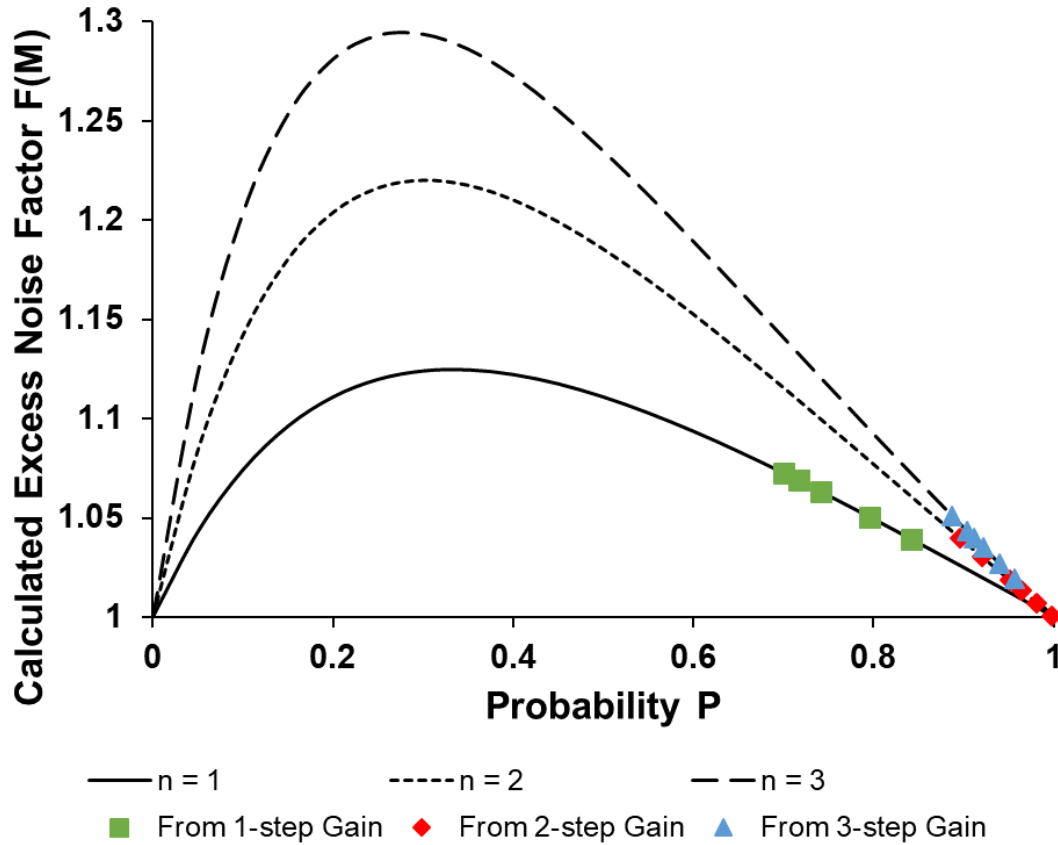


Figure 5-12: Calculated excess noise factor of 1, 2, and 3-step staircase APDs as a function of impact ionization probability.

These approaches for determining the excess noise factor in staircase APDs share the common assumption that the Burgess variance theorem can be applied to the impact ionization variability:

$$\text{var}N_M = \langle M \rangle^2 \text{var}N + \langle N \rangle \text{var}M \quad (5.6)$$

Here, N is the total number of carriers and N_M is the total number of carriers after multiplication. This model is appropriate for a traditional impact ionization process, since each carrier will impact ionize at relatively disperse locations throughout the device, leading to a variance in the gain. This assumption no longer holds, however, for a staircase APD, as the impact ionization events at subsequent steps are inherently linked to the previous steps. Simply put, applying the

traditional APD noise models to the staircase design treats the impact ionization at the steps as separate events, while in fact, they are innately connected.

The resistance-normalized noise power spectral density $S(f)$ of a traditional APD can be expressed as

$$S(f) = 2q\langle M \rangle^2 F(M) I_0 \quad (5.7)$$

where $\langle M \rangle$ is the averaged gain and I_0 is the photocurrent at unity gain, indicating that $S(f)$ is proportional to the gain squared.³⁰ This equation is also applicable to PMTs.⁹⁹ As mentioned, this relation is derived from the random spatial and temporal distribution of impact ionization events within the APD. To the contrary, in a staircase APD, a set number (according to the steps) of impact ionization events are forced to occur at fixed positions and times. Previous theories for excess noise in staircase APDs only consider the effects of the fixed number of maximum impact ionization events on reducing the gain variance.^{14,30,98} However, the spatial and temporal restrictions on the impact ionization events must also be considered, similarly to the noise reductions resulting from impact-ionization-inducing heterojunctions.^{21,26}

When these additional factors are considered in the noise power derivation,^{*} $S(f)$ can be expressed as a function of impact ionization probability for an n -step staircase as

$$S(f) = 2q[1 + (2^n - 1)P]I_0 \quad (5.8)$$

^{*} This new theory behind the staircase APD noise was derived in large by Yuan Yuan and Keye Sun at the University of Virginia. The full derivation will be submitted for future publication.

Since the gain of an n -step staircase APD can be expressed as a function of the impact ionization probability by equation (5.1), for staircases with high impact ionization probabilities ($P \approx 1$), equations (5.1) and (5.8) can be respectively simplified:

$$M = (1 + P)^n \xrightarrow{P=1} M = 2^n \quad (5.9)$$

$$S(f) = 2q[1 + (2^n - 1)P]I_0 \xrightarrow{P=1} S(f) = 2q(2^n)I_0 \quad (5.10)$$

In contrast to equation (5.7), equation (5.10) indicates that for staircase APDs, $S(f)$ is proportional to the gain rather than the gain squared, indicating an exponential difference between staircase and traditional APD noise, accentuated by increased gain.

Because staircase APDs are not expected to perform according to the local field model,¹⁵ their noise must be compared to that of a control structure, as described in section 5.1. The ratio of the noise power of the staircase APD to the control APD should scale according to equation (5.10). This behavior was first characterized with the 1-step staircase device.^{97,100} Similar behavior has since been measured for the 2 and 3-step staircase APDs. Figure 5-13 shows the staircase noise power normalized to control noise power for the 1 (a), 2 (b), and 3-step (c) staircase APDs. As indicated, the measured results increase proportionally to gain, which agrees with this model (equation (5.10)).

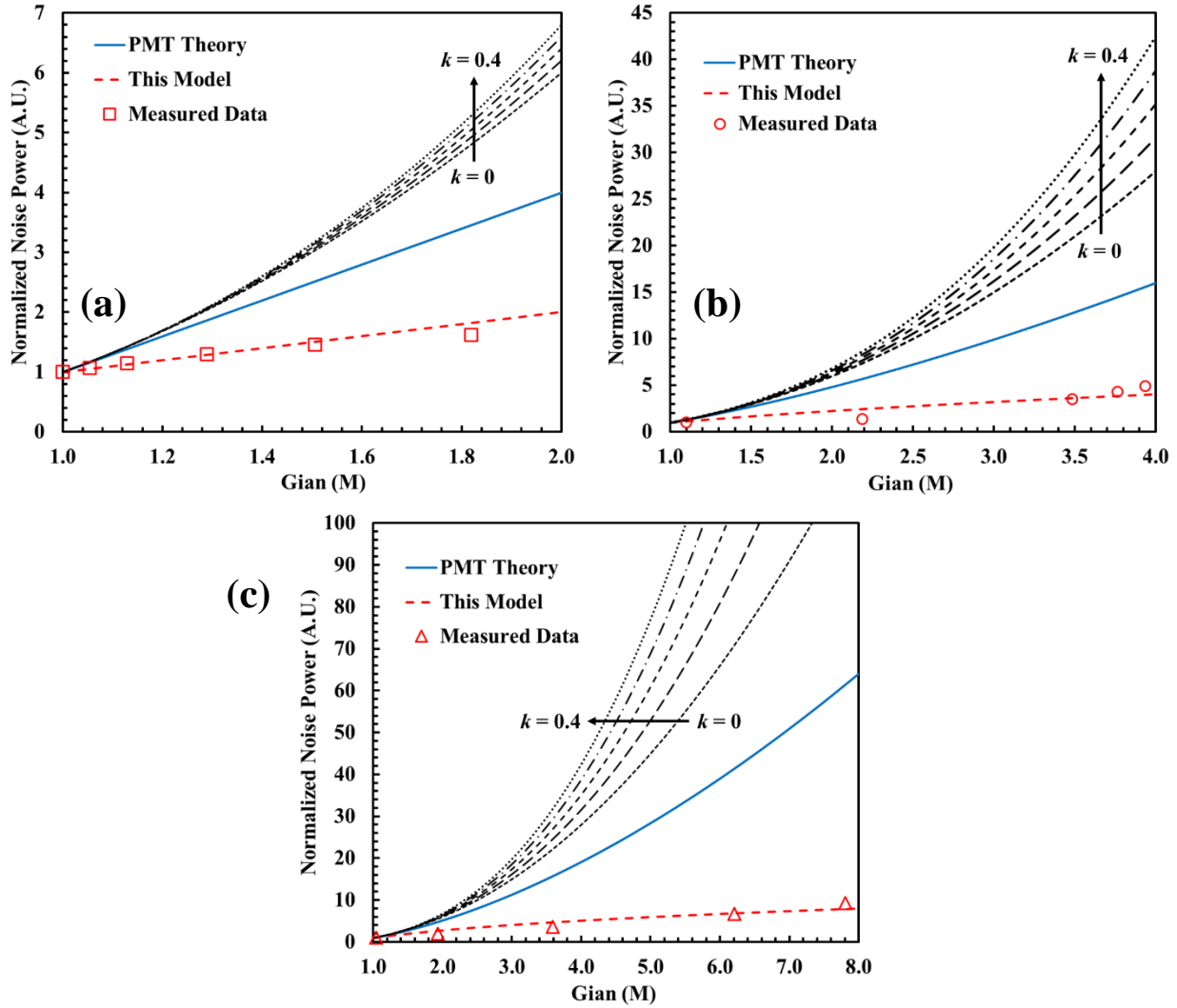


Figure 5-13: Noise power ratio of staircase to control APDs as a function of gain for 1 (a), 2 (b), and 3-step (c) devices.

To corroborate the above noise theory further, Stephen March at the University of Texas at Austin performed Monte Carlo simulations of the impact ionization events in the staircase APD structures. These simulations tracked the gain variation of individual electrons within the device structures and solved for the excess noise by equation (1.1). The noise power was then extracted by using the same bandwidth and frequency at which the noise power measurements were taken. The simulated results of 10,000 trials are compared to the theoretical and measured results above and plotted as a function of gain for each of the staircase devices. Figure 5-14

shows excellent agreement between the measured, theoretical, and simulated noise power for each staircase structure. The agreement between these results lends additional credibility to the impressively low-noise characteristics of staircase APDs.

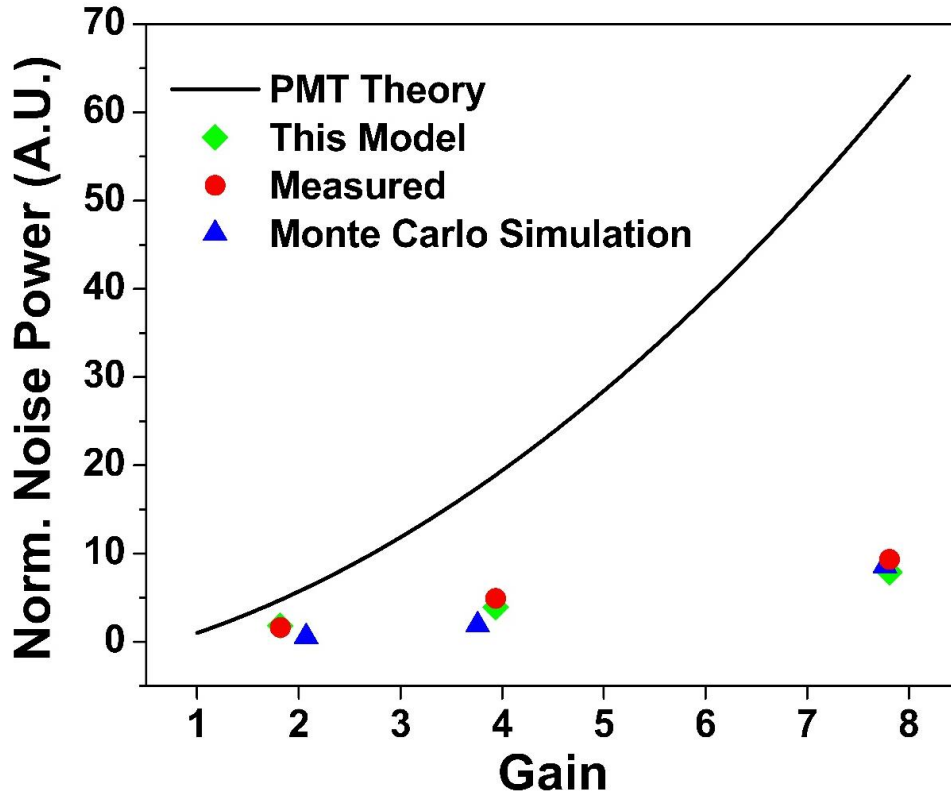


Figure 5-14: Normalized noise power comparison of 1, 2, and 3-step staircase APDs to PMT noise theory, the model described above, and Monte Carlo simulation results.

In this chapter, I have demonstrated 2 and 3-step $\text{Al}_x\text{In}_{1-x}\text{As}_y\text{Sb}_{1-y}$ staircase APDs with impact ionization probabilities $> 95\%$. These devices operated in the region of 5 V reverse bias and indicated reducible J_{dark} through cryogenic cooling. Unprecedented low-noise characteristics were demonstrated, which were corroborated by an analytical model as well as Monte Carlo simulations. The conduction band tunability of $\text{Al}_x\text{In}_{1-x}\text{As}_y\text{Sb}_{1-y}$ has thus far rendered it the only materials system capable of realizing true staircase APDs. These impressive characteristics establish $\text{Al}_x\text{In}_{1-x}\text{As}_y\text{Sb}_{1-y}$ staircase APDs as a framework for innovative photodetection capabilities.

6 Future Work

This chapter lists possible next-step investigations into $\text{Al}_x\text{In}_{1-x}\text{As}_y\text{Sb}_{1-y}$ APD designs. Since I will remain at the University of Virginia for postdoctoral research after my completion of this degree, I hope to explore some of these ideas myself.

6.1 $\text{Al}_x\text{In}_{1-x}\text{As}_y\text{Sb}_{1-y}$ MWIR SACM APDs

As of the writing of this document, only the aforementioned 2- μm SACM APDs have been demonstrated. Due to the scaling of the $\text{Al}_x\text{In}_{1-x}\text{As}_y\text{Sb}_{1-y}$ bandgap with Al content, the logical progression is toward increasingly narrow-bandgap absorbers with $x < 0.3$. The next planned structure is for a 3- μm SACM APD, corresponding to an $\text{Al}_{0.15}\text{In}_{0.85}\text{As}_y\text{Sb}_{1-y}$ absorber. While the first iteration of this structure has been tested and punch-through observed, the devices consistently broke down prior to significant multiplication gain. Figure 6-1 shows this measured I-V characteristic under 2- μm illumination. Based on a responsivity calculation from the laser power, this device demonstrates ~43% external quantum efficiency at punch through, which is approximately double that of the SACM APD discussed in section 4.2. This improvement is consistent with the expected absorption coefficient increase of a narrower-bandgap material.

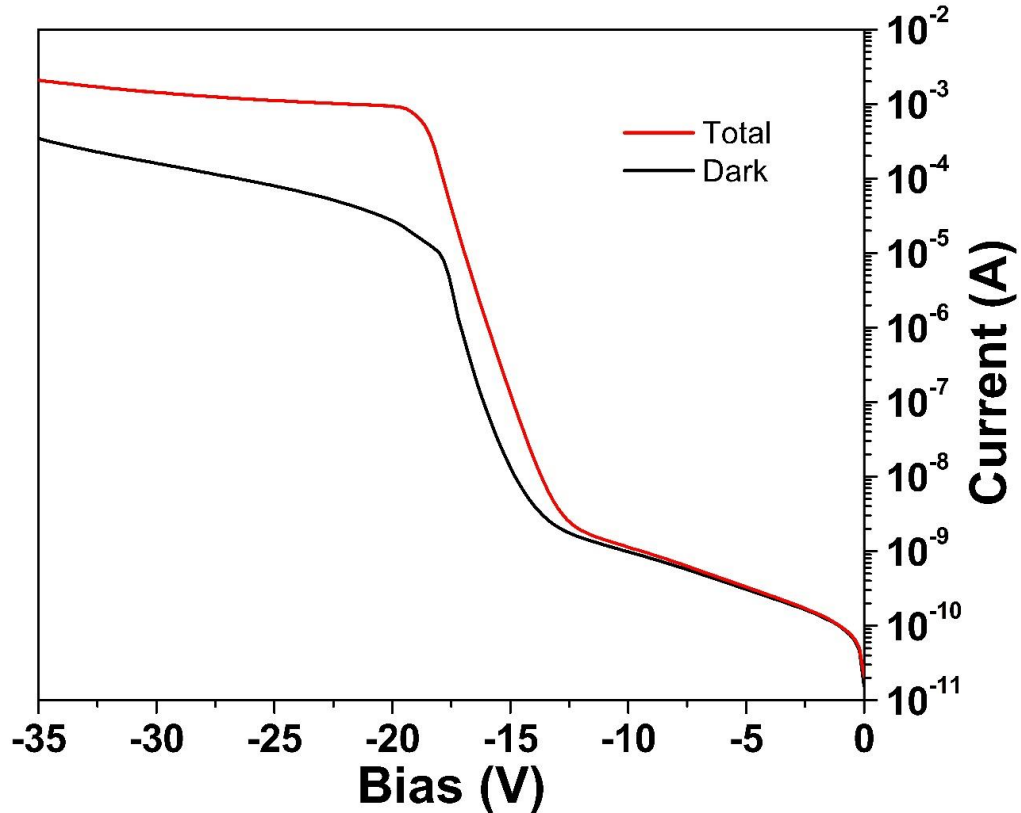


Figure 6-1. I-V characteristic of a potential 3- μm SACM APD.

Moving forward, the doping level in the charge layer should be increased in order to reduce the electric field magnitude in the absorber, thereby preventing breakdown and enabling greater impact ionization in the multiplication region. Based on the initial results and these changes, I believe a 3- μm $\text{Al}_x\text{In}_{1-x}\text{As}_y\text{Sb}_{1-y}$ SACM APD should be achievable.

Ultimately, the absorber material in this design could be reduced to InAsSb ($x = 0$), which corresponds to an optical cutoff wavelength of approximately 5 μm . The difficulty of this concept is that while sufficient electric field must remain in the $x = 0.7$ multiplication region, the bandgap of InAsSb is so narrow (0.247 eV) that it is highly susceptible to tunneling, even under low electric field magnitudes. The challenge then, will be in obtaining an ideal charge layer doping while maintaining an InAsSb absorber with as low a background doping as possible in order to minimize change in energy across the absorber. This balance is exacerbated by the need

to lower the large conduction band offset between the absorption and multiplication regions. While multiple iterations of this 5- μm SACM structure have been attempted, so far, all have shown either immediate tunneling when the electric field reaches the InAsSb absorber or have broken down before the charge and grading layers have fully depleted.

6.2 $\text{Al}_x\text{In}_{1-x}\text{As}_y\text{Sb}_{1-y}$ nBn Detectors

In the last fifteen years, the nBn structure was demonstrated for long and mid-wavelength detector applications¹⁰¹ and has gained considerable interest. This structure utilizes a wide-bandgap “barrier” layer between two narrow-bandgap n-doped regions to eliminate dark current contributions from Shockley-Reed-Hall recombination. While not an APD, the nBn architecture enables the photodetection of infrared light at higher temperatures due to both the barrier design and the low operating voltage. The use of superlattice materials in this architecture has demonstrated impressive detection capabilities.^{102–104}

Due to its high temperature stability and bandgap tunability, $\text{Al}_x\text{In}_{1-x}\text{As}_y\text{Sb}_{1-y}$ may be ideally suited for MWIR nBn structures. The conduction-band-dominated tunability of $\text{Al}_x\text{In}_{1-x}\text{As}_y\text{Sb}_{1-y}$ ³⁹ lends itself to achievable barrier designs. Although the nBn structure is a hole-exclusive device, it does not require impact ionization. The effects of the hole transport within nBn detectors on the temperature stability of $\text{Al}_x\text{In}_{1-x}\text{As}_y\text{Sb}_{1-y}$ is yet to be investigated.

6.3 Improved $\text{Al}_x\text{In}_{1-x}\text{As}_y\text{Sb}_{1-y}$ Staircase APDs

Although staircases with up to three steps have been demonstrated, additional steps and feasible gains > 8 would certainly provide additional benefit. Furthermore, due to the newly observed noise characteristics described in section 5.3, higher gains offer a larger difference in the noise power between staircase and traditional APDs or PMTs.

The addition of wider narrow-bandgap $\text{Al}_{0.07}\text{In}_{0.93}\text{As}_y\text{Sb}_{1-y}$ regions would serve to improve the multi-step staircase designs by reducing the overall dark current, as demonstrated with a 1-step design in section 5.2. It may be necessary however, to modify these regions individually for each step, meaning the use of slightly different narrow-bandgap compositions depending on the spatial location of the steps. Like a PMT, the overall gain of the staircase APD is highly affected by the region of initial multiplication, which follows from the Friis relation of cascaded amplifier noise.¹⁰⁵ For this reason, I believe it may be necessary to retain the “0%” InAsSb narrow-bandgap region in the first step of multi-step staircase APDs.

6.4 Extended Staircase APDs

Since the heretofore demonstrated staircase APDs are only applicable for wavelengths that can be absorbed by the wide-bandgap $\text{Al}_{0.7}\text{In}_{0.3}\text{As}_y\text{Sb}_{1-y}$ material, which shows an optical cutoff between 1 and 1.1 μm , further research must be directed toward applying the staircase methodology to longer wavelength applications. Due to its low-voltage operation and superior noise characteristics, a staircase APD functioning at longer wavelengths could revolutionize the

capabilities of manifold optical receivers. There are several potential methods for extending the operating wavelength of the staircase APD design.

At this time, all the successfully demonstrated staircase APDs have been illuminated with short (543-nm) wavelengths in order to ensure full absorption of the incident photons before the first step where the bandgap narrows and the absorption coefficient increases. Using the current design with an $\text{Al}_{0.7}\text{In}_{0.3}\text{As}_y\text{Sb}_{1-y}$ wide-bandgap material, the thickness of the pre-step region could be increased in order to ensure near-total absorption of photons closer to the cutoff wavelength. Based on a measured absorption coefficient of 7688 cm^{-1} at 850 nm, which is a common VCSEL wavelength, this region would need to be increased to $3.9\text{ }\mu\text{m}$ for 95% absorption. The drawbacks of this approach are the uncertainty of adequate carrier lifetimes, the achievability of the required background doping levels, and the necessarily increased operating voltage due to the device thickness.

A design proposed by the University of Texas at Austin involved a pre-step region which was gradually increased from a narrow-bandgap region up to the wide-bandgap material at the top of the step. This approach has the added advantage of increased absorption at the top of the absorber while being more resilient to the high tunneling currents which are commonplace in narrow-bandgap materials. In this case, background doping could add an advantage of lowering the conduction band edge of the graded absorber to improve electron mobility. One such design has been tested and proved unsuccessful, although there is some likelihood this failure was due to either dissimilarities between the staircase and the control or adverse effects from delta doping at the bottom of the step.

Materials such as InGaAs, which have been traditionally used for telecommunications in the C and O bands (1.31 and $1.55\text{ }\mu\text{m}$), experienced the typical setbacks associated with narrow-

bandgap PIN-junction APDs. Chief among these is the limited gain that can be achieved before tunneling overwhelms the photocurrent as a result of the narrow bandgap. As discussed in section 4, the SAM/SACM structures were the first major breakthrough in enabling the use of APDs for longer wavelength applications by separating the narrow-bandgap absorber from a wide-bandgap multiplication region. As a superior low-noise multiplication “region,” the staircase structure could ultimately be applied to the SACM architecture to allow the coupling of a narrow-bandgap absorber to this design adjacent to a charge/grading region. This design is illustrated in Figure 6-2. The $\text{Al}_x\text{In}_{1-x}\text{As}_y\text{Sb}_{1-y}$ materials system conveniently offers multiple narrow-bandgap absorber options that remain lattice matched to the staircase structure and the GaSb substrate. Furthermore, the staircase structure may prove simpler to use with an MWIR absorber than a traditional wide-bandgap multiplication region due to its low-voltage operation.

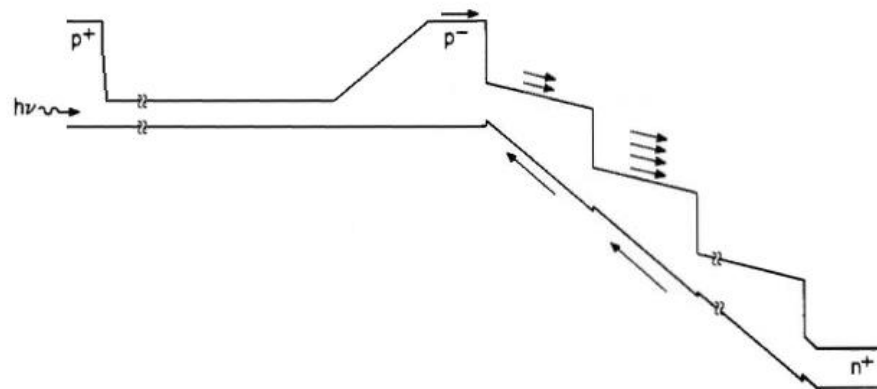


Figure 6-2: Conceptual design of an SACM staircase APD.

Publications

Journals

1. **A. H. Jones**, S. D. March, S. R. Bank, and J. C. Campbell, "Low-noise, high-temperature AlInAsSb/GaSb avalanche photodiodes for 2- μ m applications," *Nature Photonics*, accepted for publication, (2020).
2. J. Zheng, S. Ahmed, Y. Yuan, **A. H. Jones**, Y. Tan, A. K. Rockwell, S. R. Bank, A. W. Ghosh, and J. C. Campbell, "Full band Monte Carlo simulation of AlInAsSb digital alloys," *InfoMat*, 1-5, (2020).
3. N. Zhang, **A. H. Jones**, Z. Deng, and B. Chen, "Defect characterization of AlInAsSb digital alloy avalanche photodetectors with low frequency noise spectroscopy," *Optics Express*, 28 (8), 11682-11691, (2020).
4. D. R. Fink, S. Lee, S. H. Kodati, V. Rogers, T. J. Ronningen, M. Windlow, C. H. Grein, **A. H. Jones**, J. C. Campbell, J. F. Klem, and S. Krishna, "Determination of background doping polarity of unintentionally doped semiconductor layers," *Applied Physics Letters*, 116 (7), 072103, (2020).
5. Y. Shen, **A. H. Jones**, Y. Yuan, J. Zheng, Y. Peng, B. VanMil, K. Olver, A. V. Sampath, C. Parker, E. Opila, and J. C. Campbell, "Near ultraviolet enhanced 4H-SiC Schottky diode," *Applied Physics Letters*, 115 (26), 261101, (2019).
6. S. Lee, H. J. Jo, S. Mathews, J. A. Simon, T. J. Ronningen, S. H. Kodati, D. R. Fink, J. S. Kim, M. Winslow, C. H. Grein, **A. H. Jones**, J. C. Campbell, and S. Krishna, "Investigation of carrier localization in InAs/AlSb type-II superlattice material system," *Applied Physics Letters*, 115 (12), 211601, (2019).
7. **A. H. Jones**, A. K. Rockwell, S. D. March, Y. Yuan, S. R. Bank, and J. C. Campbell, "High gain, low dark current Al_{0.8}In_{0.2}As_{0.23}Sb_{0.77} avalanche photodiodes," *Photonics Technology Letters*, 31 (24), 1948-1951, (2019).
8. H. Y. Zhao, **A. H. Jones**, R.-L. Chao, Z. Ahmad, J. C. Campbell, and J. W. Shi, "High-speed avalanche photodiodes with wide dynamic range performance," *Journal of Lightwave Technology*, 37 (23), 5945-5952, (2019).
9. J. Zheng, **A. H. Jones**, Y. Tan, A. K. Rockwell, S. D. March, S. Z. Ahmen, C. A. Dukes, A. W. Ghosh, S. R. Bank, and J. C. Campbell, "Characterization of band offsets in Al_xIn_{1-x}As_ySb_{1-y} alloys with varying Al composition," *Applied Physics Letters*, 115 (12), 122105, (2019).
10. Y. Yuan, D. Jung, K. Sun, J. Zheng, **A. H. Jones**, J. E. Bowers, and J. C. Campbell, "III-V on Silicon avalanche photodiodes by heteroepitaxy," *Optics Letters*, 44 (14), 3538-3541, (2019).

11. Y. Yuan, A. K. Rockwell, Y. Peng, J. Zheng, S. D. March, **A. H. Jones**, M. Ren, S. R. Bank, and J. C. Campbell, "Comparison of different period digital alloy Al_{0.7}InAsSb avalanche photodiodes," *Journal of Lightwave Technology*, 37(14), 3647-3654, (2019).
12. Y. Yuan, J. Zheng, K. Sun, **A. H. Jones**, A. K. Rockwell, S. D. March, Y. Shen, S. R. Bank, and J. C. Campbell, "Stark-localization-limited Franz-Keldysh effect in InAlAs digital alloys," *Physica Status Solidi Rapid Research Letters*, 1900272, (2019).
13. A. K. Rockwell, M. Ren, M. E. Woodson, **A. H. Jones**, S. D. March, Y. Tan, Y. Yuan, Y. Sun, R. Hool, S. J. Maddox, M. L. Lee, A. W. Ghosh, J. C. Campbell, and S. R. Bank, "Toward deterministic construction of low noise avalanche photodetector materials," *Applied Physics Letters*, 113 (10), 102106, (2018).
14. A. K. Rockwell, Y. Yuan, **A. H. Jones**, S. D. March, S. R. Bank, and J. C. Campbell, "Al_{0.8}In_{0.2}As_{0.23}Sb_{0.77} Avalanche Photodiodes," *Photonics Technology Letters*, 30 (11), 1048-1051, (2018).
15. **A. H. Jones**, Y. Yuan, M. Ren, S. J. Maddox, S. R. Bank, and J. C. Campbell, "Al_xIn_{1-x}As_ySb_{1-y} photodiodes with low avalanche breakdown temperature dependence," *Optics Express*, 25 (20), 24340-24345, (2017).
16. H. D. Schreiber, **A. H. Jones**, C. M. Lariviere, K. M. Mayhew, and J. B. Cain, "Role of aluminum in red-to-blue color changes in *Hydrangea macrophylla* sepals," *BioMetals*, 24 (6), 1005-1015, (2011).

Conferences & Abstracts

1. **A. H. Jones**, S. D. March, S. R. Bank, and J. C. Campbell, "Al_xIn_{1-x}As_ySb_{1-y} separate absorption, charge, and multiplication, avalanche photodiode for 2- μ m detection," *Proc. of the 32nd conf. of the IEEE Photonics Society*, Post-deadline, San Antonio, TX, USA, Sept. 29 - Oct. 3, (2019).
2. J. W. Shi, H. Y. Zhao, N. Nassem, **A. H. Jones**, and J. C. Campbell, "High-speed and wide dynamic range avalanche photodiode for coherent Lidar application," *Proc. of the 32nd conf. of the IEEE Photonics Society*, San Antonio, TX, USA, Sept. 29 - Oct. 3, (2019).
3. Y. Yuan, D. Jung, K. Sun, J. Zheng, **A. H. Jones**, J. E. Bowers, and J. C. Campbell, "III-V Compound Avalanche Photodiodes on Silicon," *Integrated Photonics Research, Silicon and Nanophotonics*, Burlingame, CA, USA, July 29 - Aug. 1, (2019).
4. A. K. Rockwell, M. Ren, M. E. Woodson, **A. H. Jones**, S. D. March, Y. Tan, Y. Yuan, S. J. Maddox, A. Ghosh, J. C. Campbell, and S. R. Bank, "Band structure influence on noise properties of III-V digital alloys," *Proc. of the 61st Electronic Materials Conference*, Ann Arbor, MI, USA, June 26-28, (2019).

5. S. D. March, **A. H. Jones**, A. K. Rockwell, M. Ren, M. E. Woodson, S. J. Maddox, J. C. Campbell, and S. R. Bank, "Modeling and measurement of carrier trapping and tunneling in $\text{Al}_x\text{In}_{1-x}\text{As}_y\text{Sb}_{1-y}$ digital alloys," *Proc. of the 61st Electronic Materials Conference*, Ann Arbor, MI, USA, June 26-28, (2019).
6. K. M. McNicholas, R. El-Jaroudi, J. Kopaczek, **A. H. Jones**, D. J. Ironside, R. Kudrawiec, J. C. Campbell, and S. R. Bank, "Progress towards B-III-V optoelectronic devices on silicon," *Proc. of the 61st Electronic Materials Conference*, Ann Arbor, MI, USA, June 26-28, (2019).
7. S. R. Bank, J. C. Campbell, S. J. Maddox, A. K. Rockwell, M. E. Woodson, M. Ren, **A. H. Jones**, S. D. March, J. Zheng, and Y. Yuan, "Digital alloy growth of low-noise avalanche photodiodes," *IEEE Research and Applications of Photonics in Defense Conference, RAPID 2018*, Miramar Beach, FL, USA, Aug. 22-24, (2018).
8. S. Lee, A. Kazemi, S. H. Kodati, S. Mathews, T. J. Ronningen, M. Winslow, C. H. Grein, N. Ye, **A. H. Jones**, J. C. Campbell, and S. Krishna, "InAs/AlSb type II superlattice avalanche photodiodes," *Proc. SPIE 10637, Laser Technology for Defense and Security XIV*, May 4, (2018).
9. M. Ren, Y. Yuan, **A. H. Jones**, S. J. Maddox, M. E. Woodson, S. R. Bank, and Joe C. Campbell, "Operation stability study of AlInAsSb avalanche photodiodes," *Proc. of the 30th conf. of the IEEE Photonics Society*, Orlando, FL, USA, Oct. 1-5, (2017).

Works Cited

1. Campbell, J. C. Recent Advances in Avalanche Photodiodes. *J. Light. Technol.* **34**, 278–285 (2016).
2. Forrest, S. R. Chapter 4 Sensitivity of Avalanche Photodetector Receivers for High-Bit-Rate Long-Wavelength Optical Communication Systems. in *Semiconductors and Semimetals* vol. 22 329–387 (Elsevier, 1985).
3. Bertone, N. & Clark, W. APD ARRAYS - Avalanche photodiode arrays provide versatility in ultrasensitive applications. *Laser Focus World* vol. 43 69–73 (2007).
4. Kasper, B. & Campbell, J. Multigigabit-per-second avalanche photodiode lightwave receivers. *J. Light. Technol.* **5**, 1351–1364 (1987).
5. Campbell, J. C. Advances in photodetectors. in *Optical Fiber Telecommunications V A* 221–268 (Elsevier, 2008). doi:10.1016/B978-0-12-374171-4.00008-3.
6. Huang, Z. *et al.* 25 Gbps low-voltage waveguide Si–Ge avalanche photodiode. *Optica* **3**, 793 (2016).
7. Lecomte, R., Martel, C. & Carrier, C. Status of BGO-avalanche photodiode detectors for spectroscopic and timing measurements. *Nucl. Instrum. Methods Phys. Res. Sect. Accel. Spectrometers Detect. Assoc. Equip.* **278**, 585–597 (1989).
8. Dunai, D., Zoletnik, S., Sárközi, J. & Field, A. R. Avalanche photodiode based detector for beam emission spectroscopy. *Rev. Sci. Instrum.* **81**, 103503 (2010).
9. Albota, M. A. *et al.* Three-dimensional imaging laser radar with a photon-counting avalanche photodiode array and microchip laser. *Appl. Opt.* **41**, 7671 (2002).
10. Aull, B. F. *et al.* Large-Format Geiger-Mode Avalanche Photodiode Arrays and Readout Circuits. *IEEE J. Sel. Top. Quantum Electron.* **24**, 1–10 (2018).

11. Jiang, X. *et al.* InP-Based Single-Photon Detectors and Geiger-Mode APD Arrays for Quantum Communications Applications. *IEEE J. Sel. Top. Quantum Electron.* **21**, 5–16 (2015).
12. Kardynał, B. E., Yuan, Z. L. & Shields, A. J. An avalanche-photodiode-based photon-number-resolving detector. *Nat. Photonics* **2**, 425–428 (2008).
13. Emmons, R. B. Avalanche-Photodiode Frequency Response. *J. Appl. Phys.* **38**, 3705–3714 (1967).
14. Matsuo, K., Teich, M. & Saleh, B. Noise properties and time response of the staircase avalanche photodiode. *J. Light. Technol.* **3**, 1223–1231 (1985).
15. McIntyre, R. J. Multiplication noise in uniform avalanche diodes. *IEEE Trans. Electron Devices* **ED-13**, 164–168 (1966).
16. Cartier, E., Fischetti, M. V., Eklund, E. A. & McFeely, F. R. Impact ionization in silicon. *Appl. Phys. Lett.* **62**, 3339–3341 (1993).
17. Capasso, F., Tsang, W. T., Hutchinson, A. L. & Williams, G. F. Enhancement of electron impact ionization in a superlattice: A new avalanche photodiode with a large ionization rate ratio. *Appl. Phys. Lett.* **40**, 38–40 (1982).
18. Capasso, F. Band-gap engineering via graded gap, superlattice, and periodic doping structures: Applications to novel photodetectors and other devices. *J. Vac. Sci. Technol. B Microelectron. Nanometer Struct.* **1**, 457 (1983).
19. Kagawa, T., Kawamura, Y. & Iwamura, H. InGaAsP/InAlAs superlattice avalanche photodiode. *IEEE J. Quantum Electron.* **28**, 1419–1423 (1992).

20. Jwo, S.-C., Wu, M.-T., Chen, J.-K., Hong, J.-W. & Chang, C.-Y. Amorphous silicon/silicon carbide superlattice avalanche photodiodes. *IEEE Trans. Electron Devices* **35**, 1279–1283 (1988).
21. Saleh, M. A. *et al.* Impact-ionization and noise characteristics of thin III-V avalanche photodiodes. *IEEE Trans. Electron Devices* **48**, 2722–2731 (2001).
22. Ong, D. S. *et al.* A Monte Carlo investigation of multiplication noise in thin p+-i-n+ GaAs avalanche photodiodes. *IEEE Trans. Electron Devices* **45**, 1804–1810 (1998).
23. Yuan, P. *et al.* A new look at impact ionization-Part II: Gain and noise in short avalanche photodiodes. *IEEE Trans. Electron Devices* **46**, 1632–1639 (1999).
24. Nada, M., Yamada, Y. & Matsuzaki, H. Responsivity-Bandwidth Limit of Avalanche Photodiodes: Toward Future Ethernet Systems. *IEEE J. Sel. Top. Quantum Electron.* **24**, 1–11 (2018).
25. Zhao, H.-Y. *et al.* High-Speed Avalanche Photodiodes With Wide Dynamic Range Performance. *J. Light. Technol.* **37**, 5945–5952 (2019).
26. Campbell, J. C. Low-noise, high-speed avalanche photodiodes. in *Device Research Conference. Conference Digest (Cat. No.01TH8561)* 9–13 (IEEE, 2001).
doi:10.1109/DRC.2001.937851.
27. Yuan, P. *et al.* Avalanche photodiodes with an impact-ionization-engineered multiplication region. *IEEE Photonics Technol. Lett.* **12**, 1370–1372 (2000).
28. Chia, C. K. *et al.* Impact ionization in Al_xGa_{1-x}As/GaAs single heterostructures. *J. Appl. Phys.* **84**, 4363–4369 (1998).
29. Williams, G. F., Capasso, F. & Tsang, W. T. The graded bandgap multilayer avalanche photodiode: A new low-noise detector. *IEEE Electron Device Lett.* **3**, 71–73 (1982).

30. Capasso, F., Won-Tien Tsang & Williams, G. F. Staircase solid-state photomultipliers and avalanche photodiodes with enhanced ionization rates ratio. *IEEE Trans. Electron Devices* **30**, 381–390 (1983).
31. Sun, M. J. *et al.* Gallium arsenide electroabsorption avalanche photodiode waveguide detectors. *Appl. Opt.* **17**, 1568 (1978).
32. Kinsey, G. S., Campbell, J. C. & Dentai, A. G. Waveguide avalanche photodiode operating at 1.55 μm with a gain-bandwidth product of 320 GHz. *IEEE Photonics Technol. Lett.* **13**, 842–844 (2001).
33. Kato, K. Ultrawide-band/high-frequency photodetectors. *IEEE Trans. Microw. Theory Tech.* **47**, 1265–1281 (1999).
34. Maddox, S. J., March, S. D. & Bank, S. R. Broadly Tunable AlInAsSb Digital Alloys Grown on GaSb. *Cryst. Growth Des.* **16**, 3582–3586 (2016).
35. Bank, S. R. *et al.* Avalanche Photodiodes Based on the AlInAsSb Materials System. *IEEE J. Sel. Top. Quantum Electron.* **24**, 1–7 (2018).
36. Jones, A. H. *et al.* Al_xIn_{1-x}As_ySb_{1-y} photodiodes with low avalanche breakdown temperature dependence. *Opt. Express* **25**, 24340 (2017).
37. Jones, A. H. *et al.* High Gain, Low Dark Current Al_{0.8}In_{0.2}As_{0.23}Sb_{0.77} Avalanche Photodiodes. *IEEE Photonics Technol. Lett.* **31**, 1948–1951 (2019).
38. Ren, M. *et al.* Characteristics of Al_xIn_{1-x}As_ySb_{1-y} (x:0.3-0.7) Avalanche Photodiodes. *J. Light. Technol.* **35**, 2380–2384 (2017).
39. Zheng, J. *et al.* Characterization of band offsets in Al_xIn_{1-x}As_ySb_{1-y} alloys with varying Al composition. *Appl. Phys. Lett.* **115**, 122105 (2019).

40. Tan, L. J. J. *et al.* Temperature Dependence of Avalanche Breakdown in InP and InAlAs. *IEEE J. Quantum Electron.* **46**, 1153–1157 (2010).
41. Massey, D. J., David, J. P. R. & Rees, G. J. Temperature Dependence of Impact Ionization in Submicrometer Silicon Devices. *IEEE Trans. Electron Devices* **53**, 2328–2334 (2006).
42. Susa, N., Nakagome, H., Mikami, O., Ando, H. & Kanbe, H. New InGaAs/InP avalanche photodiode structure for the 1-1.6 μm wavelength region. *IEEE J. Quantum Electron.* **16**, 864–870 (1980).
43. Zhou, X. *et al.* Thin $\text{Al}_{1-x}\text{Ga}_x\text{As}_{0.56}\text{Sb}_{0.44}$ diodes with extremely weak temperature dependence of avalanche breakdown. *R. Soc. Open Sci.* **4**, 170071 (2017).
44. Shiyu Xie & Chee Hing Tan. AlAsSb Avalanche Photodiodes With a Sub-mV/K Temperature Coefficient of Breakdown Voltage. *IEEE J. Quantum Electron.* **47**, 1391–1395 (2011).
45. Giri, A. *et al.* Experimental Evidence of Suppression of Subterahertz Phonons and Thermal Conductivity in GaAs/AlAs Superlattices Due to Extrinsic Scattering Processes. *J. Phys. Chem. C* **122**, 29577–29585 (2018).
46. Ravichandran, J. *et al.* Crossover from incoherent to coherent phonon scattering in epitaxial oxide superlattices. *Nat. Mater.* **13**, 168–172 (2014).
47. Rockwell, A.-K. *et al.* $\text{Al}_{0.8}\text{In}_{0.2}\text{As}_{0.23}\text{Sb}_{0.77}$ Avalanche Photodiodes. *IEEE Photonics Technol. Lett.* **30**, 1048–1051 (2018).
48. Yuan, Y. *et al.* AlInAsSb Impact Ionization Coefficients. *IEEE Photonics Technol. Lett.* **31**, 315–318 (2019).

49. Green, M. A. Self-consistent optical parameters of intrinsic silicon at 300K including temperature coefficients. *Sol. Energy Mater. Sol. Cells* **92**, 1305–1310 (2008).
50. Ng, J. S., Tan, C. H., David, J. P. R., Hill, G. & Rees, G. J. Field dependence of impact ionization coefficients in In_{0.53}Ga_{0.47}As. *IEEE Trans. Electron Devices* **50**, 901–905 (2003).
51. Yuan, Y. *et al.* Comparison of Different Period Digital Alloy Al_{0.7}InAsSb Avalanche Photodiodes. *J. Light. Technol.* **37**, 3647–3654 (2019).
52. Nishida, K., Taguchi, K. & Matsumoto, Y. InGaAsP heterostructure avalanche photodiodes with high avalanche gain. *Appl. Phys. Lett.* **35**, 251–253 (1979).
53. Matsushima, Y., Sakai, K. & Noda, Y. New type InGaAs/InP heterostructure avalanche photodiode with buffer layer. *IEEE Electron Device Lett.* **2**, 179–181 (1981).
54. Campbell, J. C., Dentai, A. G., Holden, W. S. & Kasper, B. L. High-performance avalanche photodiode with separate absorption ‘grading’ and multiplication regions. *Electron. Lett.* **19**, 818 (1983).
55. Capasso, F., Cho, A. Y. & Foy, P. W. Low-dark-current low-voltage 1.3–1.6 μm avalanche photodiode with high-low electric field profile and separate absorption and multiplication regions by molecular beam epitaxy. *Electron. Lett.* **20**, 635 (1984).
56. Nie, H. *et al.* Resonant-cavity separate absorption, charge and multiplication avalanche photodiodes with high-speed and high gain-bandwidth product. *IEEE Photonics Technol. Lett.* **10**, 409–411 (1998).
57. Park, C. Y. *et al.* High-performance InGaAs/InP avalanche photodiode for a 2.5 Gb s⁻¹ optical receiver. *Opt. Quantum Electron.* **27**, 553–559 (1995).
58. Hasnain, G. *et al.* Buried-mesa avalanche photodiodes. *IEEE J. Quantum Electron.* **34**, 2321–2326 (1998).

59. Itzler, M. A., Loi, K. K., McCoy, S., Codd, N. & Komaba, N. Manufacturable planar bulk-InP avalanche photodiodes for 10 Gb/s applications. in *1999 IEEE LEOS Annual Meeting Conference Proceedings. LEOS'99. 12th Annual Meeting. IEEE Lasers and Electro-Optics Society 1999 Annual Meeting (Cat. No.99CH37009)* vol. 2 748–749 (IEEE, 1999).
60. Campbell, J. C., Tsang, W. T., Qua, G. J. & Johnson, B. C. High-speed InP/InGaAsP/InGaAs avalanche photodiodes grown by chemical beam epitaxy. *IEEE J. Quantum Electron.* **24**, 496–500 (1988).
61. Yasuoka, N., Kuwatsuka, H., Makiuchi, M., Uchida, T. & Yasaki, A. Large multiplication-bandwidth products in APDs with a thin InP multiplication layer. in *The 16th Annual Meeting of the IEEE Lasers and Electro-Optics Society, 2003. LEOS 2003.* vol. 2 999–1000 (IEEE, 2003).
62. Clark, W. R. *et al.* Reliable, high gain-bandwidth product InGaAs/InP avalanche photodiodes for 10 Gb/s receivers. in *OFC/IOOC . Technical Digest. Optical Fiber Communication Conference, 1999, and the International Conference on Integrated Optics and Optical Fiber Communication* 96–98 (IEEE, 1999). doi:10.1109/OFC.1999.767804.
63. Franco, D. S. *et al.* High-performance InGaAs-InP APDs on GaAs. *IEEE Photonics Technol. Lett.* **17**, 873–874 (2005).
64. Li, N. *et al.* InGaAs/InAlAs avalanche photodiode with undepleted absorber. *Appl. Phys. Lett.* **82**, 2175–2177 (2003).
65. Nada, M., Muramoto, Y., Yokoyama, H., Ishibashi, T. & Matsuzaki, H. Triple-mesa Avalanche Photodiode With Inverted P-Down Structure for Reliability and Stability. *J. Light. Technol.* **32**, 1543–1548 (2014).

66. Yagyu, E. *et al.* Recent Advances in AlInAs Avalanche Photodiodes. in *OFC/NFOEC 2007 - 2007 Conference on Optical Fiber Communication and the National Fiber Optic Engineers Conference* 1–3 (IEEE, 2007). doi:10.1109/OFC.2007.4348674.
67. Nakata, T. *et al.* An ultra high speed waveguide avalanche photodiode for 40-Gb/s optical receiver. in *Proceedings 27th European Conference on Optical Communication (Cat. No.01TH8551)* vol. 4 564–565 (IEEE, 2001).
68. Rouvie, A. *et al.* High Gain X Bandwidth Product Over 140-GHz Planar Junction AlInAs Avalanche Photodiodes. *IEEE Photonics Technol. Lett.* **20**, 455–457 (2008).
69. Assefa, S., Xia, F. & Vlasov, Y. A. Reinventing germanium avalanche photodetector for nanophotonic on-chip optical interconnects. *Nature* **464**, 80–84 (2010).
70. Kang, Y. *et al.* Monolithic germanium/silicon avalanche photodiodes with 340 GHz gain–bandwidth product. *Nat. Photonics* **3**, 59–63 (2009).
71. Vines, P. *et al.* High performance planar germanium-on-silicon single-photon avalanche diode detectors. *Nat. Commun.* **10**, 1086 (2019).
72. Duan, N., Liow, T.-Y., Lim, A. E.-J., Ding, L. & Lo, G. Q. 310 GHz gain-bandwidth product Ge/Si avalanche photodetector for 1550 nm light detection. *Opt. Express* **20**, 11031 (2012).
73. Huang, M. *et al.* 56GHz waveguide Ge/Si avalanche photodiode. in *Optical Fiber Communication Conference W4D.6* (OSA, 2018). doi:10.1364/OFC.2018.W4D.6.
74. Kang, Y. *et al.* High Performance Ge/Si Avalanche Photodiodes Development in Intel. in *Optical Fiber Communication Conference/National Fiber Optic Engineers Conference 2011 OWZ1* (OSA, 2011). doi:10.1364/OFC.2011.OWZ1.

75. Frehlich, R., Hannon, S. & Henderson, S. Performance of a 2- μm Coherent Doppler Lidar for Wind Measurements. *J. Atmospheric Ocean. Technol.* **11**, 1517–1528 (1994).
76. Scholle, K., Lamrini, S., Koopmann, P. & Fuhrberg, P. 2 μm Laser Sources and Their Possible Applications. in *Frontiers in Guided Wave Optics and Optoelectronics* (ed. Pal, B.) (InTech, 2010). doi:10.5772/39538.
77. Maddox, S. J. *et al.* Enhanced low-noise gain from InAs avalanche photodiodes with reduced dark current and background doping. *Appl. Phys. Lett.* **101**, 151124 (2012).
78. Abautret, J. *et al.* Characterization of midwave infrared InSb avalanche photodiode. *J. Appl. Phys.* **117**, 244502 (2015).
79. Gravrand, O. *et al.* HgCdTe Detectors for Space and Science Imaging: General Issues and Latest Achievements. *J. Electron. Mater.* **45**, 4532–4541 (2016).
80. Norton, P. HgCdTe infrared detectors. *Opto-Electron. Rev.* **10**, 159–174 (2002).
81. Mallick, S. *et al.* Ultralow noise midwave infrared InAs–GaSb strain layer superlattice avalanche photodiode. *Appl. Phys. Lett.* **91**, 241111 (2007).
82. Banerjee, K. *et al.* Midwave infrared InAs/GaSb strained layer superlattice hole avalanche photodiode. *Appl. Phys. Lett.* **94**, 201107 (2009).
83. Ramirez, D. A., Shao, J., Hayat, M. M. & Krishna, S. Midwave infrared quantum dot avalanche photodiode. *Appl. Phys. Lett.* **97**, 221106 (2010).
84. Ren, M. *et al.* AlInAsSb separate absorption, charge, and multiplication avalanche photodiodes. *Appl. Phys. Lett.* **108**, 191108 (2016).
85. Muñoz Uribe, M. *et al.* Near-band-gap refractive index of GaSb. *Mater. Sci. Eng. B* **38**, 259–262 (1996).

86. Liu, H.-D. *et al.* Avalanche photodiode punch-through gain determination through excess noise analysis. *J. Appl. Phys.* **106**, 064507 (2009).
87. Woodson, M. E. *et al.* Low-noise AlInAsSb avalanche photodiode. *Appl. Phys. Lett.* **108**, 081102 (2016).
88. Goh, Y. L. *et al.* InAlAs avalanche photodiode with type-II absorber for detection beyond 2 μm . in 729837 (2009). doi:10.1117/12.819818.
89. Ishimura, E. *et al.* Degradation Mode Analysis on Highly Reliable Guardring-Free Planar InAlAs Avalanche Photodiodes. *J. Light. Technol.* **25**, 3686–3693 (2007).
90. Hyun, K.-S. & Park, C.-Y. Breakdown characteristics in InP/ InGaAs avalanche photodiode with p-i-n multiplication layer structure. *J. Appl. Phys.* **81**, 974–984 (1997).
91. Sidhu, R. *et al.* 2.4 μm cutoff wavelength avalanche photodiode on InP substrate. *Electron. Lett.* **42**, 181 (2006).
92. Capasso, F. Avalanche Photodiodes with Enhanced Ionization Rates Ratio: Towards a Solid State Photomultiplier. *IEEE Trans. Nucl. Sci.* **30**, 424–428 (1983).
93. Ripamonti, G. *et al.* Realization of a staircase photodiode: Towards a solid-state photomultiplier. *Nucl. Instrum. Methods Phys. Res. Sect. Accel. Spectrometers Detect. Assoc. Equip.* **288**, 99–103 (1990).
94. Toivonen, M., Salokatve, A., Hovinen, M. & Pessa, M. GaAs/AlGaAs delta-doped staircase avalanche photodiode with separated absorption layer. *Electron. Lett.* **28**, 32–34 (1992).
95. Tsuji, M., Watanabe, I., Makita, K. & Taguchi, K. InAlGaAs Staircase Avalanche Photodiodes. *Jpn. J. Appl. Phys.* **33**, L32–L34 (1994).

96. Lambert, B. *et al.* Feasibility of 1.5 μm staircase solid state photomultipliers in the AlGaSb/GaInAsSb system. *Semicond. Sci. Technol.* **11**, 226–230 (1996).
97. Ren, M. *et al.* AlInAsSb/GaSb staircase avalanche photodiode. *Appl. Phys. Lett.* **108**, 081101 (2016).
98. van der Ziel, A., Yu, Y. J., Bosman, G. & Van Vliet, C. M. Two simple proofs of Capasso's excess noise factor FN of an ideal N-stage staircase multiplier. *IEEE Trans. Electron Devices* **33**, 1816–1817 (1986).
99. Rose, A. *Concepts in photoconductivity and allied problems*. (Krieger, 1978).
100. Ren, M. *et al.* Low excess noise AlInAsSb staircase avalanche photodiode. in *2015 73rd Annual Device Research Conference (DRC)* 1–2 (IEEE, 2015).
doi:10.1109/DRC.2015.7175563.
101. Maimon, S. & Wicks, G. W. nBn detector, an infrared detector with reduced dark current and higher operating temperature. *Appl. Phys. Lett.* **89**, 151109 (2006).
102. Ting, D. Z.-Y. *et al.* A high-performance long wavelength superlattice complementary barrier infrared detector. *Appl. Phys. Lett.* **95**, 023508 (2009).
103. Kim, H. S. *et al.* Long-wave infrared nBn photodetectors based on InAs/InAsSb type-II superlattices. *Appl. Phys. Lett.* **101**, 161114 (2012).
104. Soibel, A. *et al.* Mid-wavelength infrared InAsSb/InSb nBn detector with extended cut-off wavelength. *Appl. Phys. Lett.* **109**, 103505 (2016).
105. Friis, H. T. Noise Figures of Radio Receivers. *Proc. IRE* **32**, 419–422 (1944).

Appendix 1: Crosslight Code

This appendix contains the code for APSYS Crosslight which I developed for the $\text{Al}_x\text{In}_{1-x}\text{As}_y\text{Sb}_{1-y}$ materials system and the 2- μm (30%-Al absorber) SACM APDs.

1.1 $\text{Al}_x\text{In}_{1-x}\text{As}_y\text{Sb}_{1-y}$ Material Macro

The following is the material macro for the $\text{Al}_x\text{In}_{1-x}\text{As}_y\text{Sb}_{1-y}$ materials system. It was developed by modifying the existing AlGaAsSb macro and substituting material parameters of GaAs and GaSb for InAs and InSb respectively. This macro should be appended to the user's crosslight.mac file located on the local disk.

```

$$$$$$$$$$$$$$$$$$$$$$$$$$$$$$$$$$$$$$$$$$$$$$$$$$$$$$$$$$$$$$$$$$$$$$$$$$$$$$$$
$ *****
$ macro : algaassb_mod (modified for alinassb)
$ Bulk Al (1-x) Ga (x) As (y) Sb (1-y)
$ [free-style]
$ May be regarded as linear combination of
$ GaAs (xy) + AlSb (1-x) (1-y) + AlAs ( (1-x) y) + GaSb (x (1-y) )
$ Typical use:
$   load_macro name=algaassb_mod var1=#x var2=#y mater=#m &&
$   var_symbol1=x var_symbol2=y
$ Contributor: Yet-zen Liu
$ Revised 2005 (Ken U.)
$
$ parameter_range x=[0 1]
$ parameter_range y=[0 1]
$ parameter_range total_doping=[1.e20 1.e27]
$ parameter_range net_doping=[-1.e26 1.e26]
$ parameter_range doping_n=[1.e20 1.e26]
$ parameter_range doping_p=[1.e20 1.e26]
$ parameter_range trap_1=[1.e18 1.e24]
$*****
begin_macro algaassb_mod
material type=semicond band_valleys=(1 1) &&
    el_vel_model=n.gaas hole_vel_model=beta
$
$$$ adding lattice constant???
$lattice_constant value=6.09593
$
dielectric_constant variation=function
function(x,y)
GaAs=15.15;
GaSb=16.8;

```

```

AlSb=10.3;
AlAs=10.1;
GaAs*x*y+AlSb*(1-x)*(1-y)+AlAs*(1-x)*y+GaSb*x*(1-y)
end_function
$
electron_mass_variation=function
function(x,y)
GaAs=0.023;
GaSb=0.0135;
AlSb=0.23;
AlAs=0.15;
GaAs*x*y+AlSb*(1-x)*(1-y)+AlAs*(1-x)*y+GaSb*x*(1-y)
end_function
$
$$$$ Not Sure if these values are correct
hole_mass_variation=function
function(x,y)
GaAs=0.642;
$GaAs=0.41;
$^InAs
$GaSb=0.4116566;
GaSb=0.262;
$GaSb=0.43;
$^InSb
mvhh_alsb=0.728;
mvlh_alsb=0.14;
AlSb=( mvhh_alsb**(3/2)+mvlh_alsb**(3/2) )**(2/3);
g1_alas=3.45 ;
g2_alas=0.68 ;
mvhh_alas=1./(g1_alas-2.*g2_alas) ;
mvlh_alas=1./(g1_alas+2.*g2_alas) ;
AlAs=( mvhh_alas**(3/2)+mvlh_alas**(3/2) )**(2/3);
GaAs*x*y+AlSb*(1-x)*(1-y)+AlAs*(1-x)*y+GaSb*x*(1-y)
end_function
$
band_gap_variation=function
function(x,y)
GaAs=0.355;
GaSb=0.1737;
AlSb=2.3;
AlAs=3.0;
GaAs*x*y+AlSb*(1-x)*(1-y)+AlAs*(1-x)*y+GaSb*x*(1-y)
end_function
$
affinity_variation=function
function(x,y)
GaAs=4.9;
GaSb=4.59;
AlSb=3.65;
AlAs=3.5;
GaAs*x*y+AlSb*(1-x)*(1-y)+AlAs*(1-x)*y+GaSb*x*(1-y)
end_function
$
electron_mobility_variation=function
function(x,y,total_doping)
GaAs=0.4;
GaSb=0.77;

```


1.2 $\text{Al}_x\text{In}_{1-x}\text{As}_y\text{Sb}_{1-y}$ Material Macro Parameters

There are two variables related to the composition of the above $\text{Al}_x\text{In}_{1-x}\text{As}_y\text{Sb}_{1-y}$ material macro, identified as var1 (x) and var2 (y). It should be noted that these are not the same x and y values as the coefficients denoted in $\text{Al}_x\text{In}_{1-x}\text{As}_y\text{Sb}_{1-y}$. x and y are here related to the material macro by

$$\text{Al}(1 - x)\text{In}(x)\text{As}(y)\text{Sb}(1 - y) \quad \text{or}$$

$$\text{InAs}(xy) + \text{AlSb}(1 - x)(1 - y) + \text{AlAs}[(1 - x)y] + \text{InSb}[(1 - y)x]$$

as denoted in the macro header text. The use of var1 and var2 for the $\text{Al}_x\text{In}_{1-x}\text{As}_y\text{Sb}_{1-y}$ materials system was determined through extensive simulations comparing the resulting bandgap energy to that given in reference 34 by

$$E_g(x) = 0.247 + 0.97x + 0.47x^2 \quad \text{eV}$$

where x in the above equation corresponds to the Al fraction in $\text{Al}_x\text{In}_{1-x}\text{As}_y\text{Sb}_{1-y}$. The table below lists the value of var1 to be used for various Al compositions (bandgap energies) of $\text{Al}_x\text{In}_{1-x}\text{As}_y\text{Sb}_{1-y}$. The value of var2 should be limited to 0.61, although it has been found that retaining this value for 0%-Al InAsSb leads to an inaccurate bandgap and valence band discontinuity.

Al fraction (x) of $\text{Al}_x\text{In}_{1-x}\text{As}_y\text{Sb}_{1-y}$	Bandgap energy (eV)	Material macro var1
0.07	0.3172	0.9865
0.15	0.4031	0.951
0.30	0.5803	0.879
0.34	0.6311	0.86
0.44	0.7648	0.80
0.50	0.8495	0.77
0.53	0.8931	0.75
0.59	0.9829	0.70
0.70	1.1563	0.64

1.3 $\text{Al}_x\text{In}_{1-x}\text{As}_y\text{Sb}_{1-y}$ 2- μm 30-50-70 SACM .layer File

The following is the Crosslight .layer file for the 2- μm 30-50-70 $\text{Al}_x\text{In}_{1-x}\text{As}_y\text{Sb}_{1-y}$ SACM APD (device A in section 4.1). This design uses a 30%-Al absorber and a 70%-Al multiplication layer. There is both a charge layer and an intermediate bandgap “grading” layer between these two. For this design, the grading layer is 50% Al.

```
$ 30-50-70 2-um SACM APD
$
column column_num=1 w=50. mesh_num=4 r=1.
$
bottom_contact column_num=1 from=0 to=50 contact_num=1 contact_type=ohmic
$
$ 70% contact layer
layer_mater macro_name=algaassb_mod var_symbol1=x var1=0.64 &&
    var_symbol2=y var2=0.61 column_num=1 n_doping=5.e+24
layer d=.4 n=10 r=1
$
$ 70% multiplication
layer_mater macro_name=algaassb_mod var_symbol1=x var1=0.64 &&
    var_symbol2=y var2=0.61 column_num=1
layer d=.5 n=10 r=1
$
$charge
layer_mater macro_name=algaassb_mod var_symbol1=x var1=0.64 &&
    var_symbol2=y var2=0.61 column_num=1 p_doping=1.e+23
layer d=.08 n=20 r=1
$
$ 50% grading Layer
layer_mater macro_name=algaassb_mod var_symbol1=x var1=0.77 var_symbol2=y &&
    var2=0.61 column_num=1 p_doping=6.e+22
layer d=.2 n=30 r=1
$
$ 30% Absorber
layer_mater macro_name=algaassb_mod var_symbol1=x var1=0.879 var_symbol2=y &&
    var2=0.61 column_num=1 p_doping=1.e+22
layer d=1. n=30 r=1
$
$ 30% top p-Layer
layer_mater macro_name=algaassb_mod var_symbol1=x var1=.879 var_symbol2=y &&
    var2=0.61 column_num=1 p_doping=1.e+24
layer d=0.1 n=30 r=1
$
top_contact column_num=1 from=0 to=50 contact_num=2 contact_type=ohmic
$
end_layer
```

1.4 $\text{Al}_x\text{In}_{1-x}\text{As}_y\text{Sb}_{1-y}$ 2- μm Graded SACM .layer File

The following is the Crosslight .layer file for the 2- μm graded $\text{Al}_x\text{In}_{1-x}\text{As}_y\text{Sb}_{1-y}$ SACM APD (device B in section 4.1). This design uses a 30%-Al absorber and a 70%-Al multiplication layer. There is both a charge layer and a grading layer between these two. For this design, the grading layer is linearly graded between 30% and 70% Al.

```
$ Graded 2-um SACM APD
$
column column_num=1 w=50. mesh_num=4 r=1.
$
bottom_contact column_num=1 from=0 to=50 contact_num=1 contact_type=ohmic
$
$ 70% contact layer
layer_mater macro_name=algaassb_mod var_symbol1=x var1=0.64 &&
    var_symbol2=y var2=0.61 column_num=1 n_doping=5.e+24
layer d=.4 n=10 r=1
$
$ 70% multiplication
layer_mater macro_name=algaassb_mod var_symbol1=x var1=0.64 &&
    var_symbol2=y var2=0.61 column_num=1
layer d=.5 n=10 r=1
$
$charge
layer_mater macro_name=algaassb_mod var_symbol1=x var1=0.64 &&
    var_symbol2=y var2=0.61 column_num=1 p_doping=1.e+23
layer d=.08 n=20 r=1
$
$ AlInAsSb grading Layer
layer_mater macro_name=algaassb_mod var_symbol1=x grade_var=1 &&
    grade_from=0.64 grade_to=0.879 var_symbol2=y var2=0.61 &&
    column_num=1 p_doping=6.e+22
layer d=.2 n=30 r=1
$
$ 30% Absorber
layer_mater macro_name=algaassb_mod var_symbol1=x var1=0.879 var_symbol2=y &&
    var2=0.61 column_num=1 p_doping=1.e+22
layer d=1. n=30 r=1
$
$ 30% top p-Layer
layer_mater macro_name=algaassb_mod var_symbol1=x var1=.879 var_symbol2=y &&
    var2=0.61 column_num=1 p_doping=1.e+24
layer d=0.1 n=30 r=1
$
top_contact column_num=1 from=0 to=50 contact_num=2 contact_type=ohmic
$
end_layer
```

Appendix 2: Fabrication Recipes

This appendix contains recipes commonly used for fabrication processes.

2.1 Photolithography

All spin times are 30s except SU-8 2000.5, which should be spun for 40s. All exposure times assume a UV lamp intensity of 7 mW/cm².

2.1.1 HMDS

Spin Speed	Pre Bake	Exposure Time	Post Bake Time	Developer Soln.	Development Time
4000 RPM	30s @ 90° C	N/A	N/A	N/A	N/A

2.1.2 AZ5214 Positive Photoresist

Spin Speed	Pre Bake	Exposure Time	Post Bake Time	Developer Soln.	Development Time
4000 RPM	1m @ 100° C	60 s	N/A	AZ 300 MIF	~25 s

2.1.3 nLoR 2020 Negative Photoresist

Spin Speed	Pre Bake	Exposure Time	Post Bake Time	Developer Soln.	Development Time
3000 RPM	1m @ 110° C	10 s	1m @ 110° C	AZ 300 MIF	~2 m

2.1.4 AZ4330 Positive Photoresist

Spin Speed	Pre Bake	Exposure Time	Developer Soln.	Development Time	Post Develop Bake Time
2500 RPM	2m @ 110° C	100 s	1:4 AZ 400K:DI	~2 m	10m @ 110° C

This recipe is suitable as a hard mask for dry etching (RIE/ICP). Sample corner/edge scraping is recommended before alignment.

2.1.5 Lift-off Resist (LOR) 10B

Spin Speed	Pre Bake	Exposure Time	Post Bake Time	Developer Soln.	Development Time
4000 RPM	5m @ 180° C	With top PR	N/A	AZ 300 MIF	With top PR

As a lift-off resist, LOR 10B is useful for metal lift off with small feature sizes. After the lift-off process, the LOR 10B must be removed in AZ 300 MIF.

2.1.6 SU-8 2000.5

Spin Speed	Pre Bake	Exposure Time	Post Bake Time	Developer Soln.	Development Time
5000 RPM	70s @ 90° C	6-7 s	70s @ 90° C	SU-8 developer	~1 m

This SU-8 recipe is commonly used for sidewall passivation and results in a ~400-nm thin film. Developer should be quenched in isopropyl alcohol for ~10s and then DI water.

2.2 Etching

Etching is arguably the most critical step in the processing of top-illuminated devices. This is the source of sidewall damage, which is often the dominant mechanism responsible for device dark current. Chemical etchants attack different materials in different ways, which can result in isotropic etches. If this isotropy is unaccounted for, it can result in contact failure and device shorts. H_2O_2 is commonly used in etching solutions to oxidize the semiconductor material, enabling the acid to then remove it. For this reason, and due to its relative quantities in solution, H_2O_2 is often the limiting agent in the reaction.

2.2.1 Hydrochloric Acid - HCl

HCl solutions are extremely versatile in their material etching abilities, however, they are often the most destructive. For this reason, other etching methods should be pursued if possible, and HCl etching should primarily be used for proof-of-concept fabrication runs. Commonly used

are 5:1:5 and 10:1:10 solutions of HCl:H₂O₂:DI. Do not use steel tweezers in these solutions, as the iron will react with the HCl and turn the solution green with iron chloride. These solutions should be briefly stirred after mixing and will bubble profusely. Experimentally, an approximately steady etch rate can be reached after the solution has rested for ~1 hour. As with all chemical etchants, the etch rate will decrease with time.

2.2.2 Phosphoric Acid - H₃PO₄

Phosphoric acid is less destructive and less dangerous than HCl. A common solution is 1:1:10 of H₃PO₄:H₂O₂:DI. This has proven to be effective in etching InAlAs and AlGaAs. Stirring the H₃PO₄ and the DI prior to the addition of H₂O₂ is recommended to ensure uniformity.

2.2.3 Sulfuric Acid - H₂SO₄

Sulfuric acid is less destructive than HCl but equally as dangerous. A common solution is 1:8:80 of H₂SO₄:H₂O₂:DI. This has proven to be effective in etching InAlAs. The drawback of this solution is its relatively short lifetime compared to the others listed.

2.2.4 Citric Acid - C₆H₈O₇

Citric acid is the least destructive and least dangerous of the acids listed. It is recommended for use whenever possible for these reasons. In my studies, citric acid in conjunction with phosphoric acid was the primarily used etchant for Al_xIn_{1-x}As_ySb_{1-y}. It is also useful for etching AlGaAs. A commonly used solution for a fixed volume is 20g C₆H₈O₇ / 15 mL H₃PO₄ / 120 mL DI / 5 mL H₂O₂. For older solutions of H₂O₂, 6 to 7 mL is recommended. This solution will etch Al_xIn_{1-x}As_ySb_{1-y} with some isotropy, the amount of which is directly related to the Al content (e.g. $x = 0.8$ will etch faster and more isotropic with this etchant than $x = 0.3$). An alternate solution reduces the H₃PO₄ to 5 mL, which somewhat reduces the isotropy as well as the etch rate. It should be noted that this solution is also highly effective for etching GaSb. For

preparation, the citric acid should be stirred in the DI and H_3PO_4 for approximately 30 minutes prior to addition of the H_2O_2 . Continuous stirring at approximately 100 RPM is recommended during the etching process.

2.2.5 Bromine - Br

Bromine is an extremely caustic substance that will etch through many materials. Unfortunately, bromine will also attack photoresist, causing mesas to gradually deform. For this reason, attempting mesa etching with this chemical is not recommended unless specifically advocated in literature. Extremely dilute solutions of bromine-methanol are very effective in smoothing mesa sidewalls, specifically after dry etching processes. This can reduce surface damage and lower dark current. The recommended dilution is 1 drop of bromine per 80 mL of methanol, into which the sample should be submerged for 1-2 seconds.

2.2.6 Developer

Developer is known to etch GaSb at a slow rate.¹⁰⁶ AZ 300 MIF as well as 1:1 AZ 400K:DI can be used for this process, specifically for removing GaSb capping layers as an optical window. Care must be taken to avoid damaging the material beneath the GaSb.

2.2.7 Reactive Ion Etching with Inductively Coupled Plasma - RIE/ICP

RIE/ICP is effective for making anisotropic etches, which is useful when tight tolerances and/or deep etches are required. This technique is recommended for small devices ($< 80\text{-}\mu\text{m}$ diameter) and thicker SACM structures. For $\text{Al}_x\text{In}_{1-x}\text{As}_y\text{Sb}_{1-y}$, the use of RIE/ICP is recommended for etches deeper than $\sim 1.2\mu\text{m}$. Since the RIE/ICP process attacks both the mask pattern and the target device material unlike chemical etchants, a hard mask is required. This is typically composed of SiO_2 , however due to accessibility and/or heating concerns, photoresist can also be used (see section 2.1.4 of this appendix).

The RIE/ICP recipe used for III-V materials in this document is as follows. Ar has been occasionally substituted for N₂ in this recipe, although the etching rates increase.

Temperature	Cl flow	N ₂ flow	RIE Power	ICP Power
50° C	8 sccm	20 sccm	115 W	300 W

The photoresist-based hard mask described in section 2.1.4 of this appendix will etch at an approximate rate of 4.3 nm/s using the above recipe.

2.3 Passivation

Passivation is a vitally important area of research for improving APD functionality as well as that of other semiconductor devices. Since the epitaxially grown device material is inherently damaged by the etching process, passivation attempts to repair this damage as well as prevent further damage from occurring.¹⁰⁷ Exposed mesa sidewalls are highly susceptible to damage from oxygen and water vapor, some materials more so than others. Al, for instance, has a high affinity for oxidation.

Passivation methods include the deposition of SiO₂,¹⁰⁸ SiN,¹⁰⁹ AlN,¹¹⁰ Al₂O₃,^{111,112} and many other films. Other approaches involve sample submersion in ammonium sulfide,¹¹³ cadmium sulfide,¹¹⁴ or thioacetamide,¹¹⁵ ion implantation,¹¹⁶ plasma treatment,¹¹⁷ and the addition of spin-on coatings. In this work, all passivation involved the SU-8 coating process detailed above. So far, this method has provided the most consistency in reducing dark current. While preliminary findings suggest that this could be due in part to the low-temperature nature of the process, tightly controlled experimentation is needed to assess the performance of additional techniques. A strong and effective passivation process could greatly improve the overall

performance of $\text{Al}_x\text{In}_{1-x}\text{As}_y\text{Sb}_{1-y}$ APDs, as many have demonstrated surface-dominated dark current mechanisms.

2.4 Contacts

For most APDs, ohmic contacts are preferred, as they pose the least resistance for electrons moving into and out of the semiconductor device. Reducing the contact resistance is important, as this reduces the overall series resistance of the device, thereby improving the RC-limited bandwidth.

While gold is a common material for the surface of the contact due to its noncorrosive nature and high conductivity, the bottom of the contact must also be considered to avoid high resistance and ensure permanence. Titanium is commonly used as a “sticking” agent for other metals onto the semiconductor. However, this material can easily oxidize and should be limited to thin (≤ 10 -nm) layers to avoid the unintentional addition of contact resistance. Additionally, when using electron-beam evaporation methods, the deposition rate of titanium should be considered in reducing the oxygen content. Literature suggests that faster titanium deposition rates result in decreased oxygen content.¹¹⁸ Further reduction of the contact resistance can be achieved through annealing, typically in an RTA.¹¹⁹ If this is desired, an additional layer of platinum should be deposited between the titanium and gold to prevent the gold from “spiking” through the titanium and deep into the semiconductor. Extensive studies have investigated the use of other metals for low-resistance contacts as well.^{120–123}

An additional method for reducing contact resistance is by removing oxide on the device contact surfaces. If the contacts are deposited by electron beam-evaporation, this can be easily accomplished by “milling” the surfaces with an argon plasma prior to deposition. Studies have

also suggested that the deposition of a thick (≥ 100 -nm) gold layer aids in reducing contact resistance, although this is not fully understood.

Appendix Works Cited

106. Dier, O., Lin, C., Grau, M. & Amann, M.-C. Selective and non-selective wet-chemical etchants for GaSb-based materials. *Semicond. Sci. Technol.* **19**, 1250–1253 (2004).
107. Ma, Y. *et al.* Impact of etching on the surface leakage generation in mesa-type InGaAs/InAlAs avalanche photodetectors. *Opt. Express* **24**, 7823 (2016).
108. Zheng, X. G. *et al.* A 12×12 In_{0.53}Ga_{0.47}As-In_{0.52}Al_{0.48}As avalanche photodiode array. *IEEE J. Quantum Electron.* **38**, 1536–1540 (2002).
109. Limb, J. B. *et al.* GaN ultraviolet avalanche photodiodes grown on 6H-SiC substrates with SiN passivation. *Electron. Lett.* **44**, 313 (2008).
110. Zhang, K. *et al.* Effect of AlN passivation on mesa structured PIN InGaAs detector. *Infrared Laser Eng.* **3**, 7 (2009).
111. Chen, A. *et al.* Significant suppression of surface leakage in GaSb/AlAsSb heterostructure with Al₂O₃ passivation. *Jpn. J. Appl. Phys.* **58**, 090907 (2019).
112. Salihoglu, O. *et al.* Atomic layer deposited Al₂O₃ passivation of type II InAs/GaSb superlattice photodetectors. *J. Appl. Phys.* **111**, 074509 (2012).
113. Gin, A. *et al.* Ammonium sulfide passivation of Type-II InAs/GaSb superlattice photodiodes. *Appl. Phys. Lett.* **84**, 2037–2039 (2004).
114. Chavan, A., Chandola, A., Sridaran, S. & Dutta, P. Surface passivation and capping of GaSb photodiode by chemical bath deposition of CdS. *J. Appl. Phys.* **100**, 064512 (2006).
115. Salesse, A. *et al.* Surface passivation of GaInAsSb photodiodes with thioacetamide. *Phys. Status Solidi C* **4**, 1508–1512 (2007).

116. Zhou, Q., McIntosh, D., Liu, H.-D. & Campbell, J. C. Proton-Implantation-Isolated Separate Absorption Charge and Multiplication 4H-SiC Avalanche Photodiodes. *IEEE Photonics Technol. Lett.* **23**, 299–301 (2011).
117. Callegari, A., Hoh, P. D., Buchanan, D. A. & Lacey, D. Unpinned gallium oxide/GaAs interface by hydrogen and nitrogen surface plasma treatment. *Appl. Phys. Lett.* **54**, 332–334 (1989).
118. Olson, D. H., Freedy, K. M., McDonnell, S. J. & Hopkins, P. E. The influence of titanium adhesion layer oxygen stoichiometry on thermal boundary conductance at gold contacts. *Appl. Phys. Lett.* **112**, 171602 (2018).
119. Stareev, G. Formation of extremely low resistance Ti/Pt/Au ohmic contacts to *p*-GaAs. *Appl. Phys. Lett.* **62**, 2801–2803 (1993).
120. Lin, J. C., Yu, S. Y. & Mohny, S. E. Characterization of low-resistance ohmic contacts to n- and p-type InGaAs. *J. Appl. Phys.* **114**, 044504 (2013).
121. Lai, J. & Lee, J. Y. Pd/Ge ohmic contacts to n-type GaAs formed by rapid thermal annealing. *Appl. Phys. Lett.* **64**, 229–231 (1994).
122. Vogt, A. *et al.* Ohmic contact formation mechanism of the PdGeAu system on n-type GaSb grown by molecular beam epitaxy. *J. Appl. Phys.* **83**, 7715–7719 (1998).
123. Ikossi, K., Goldenberg, M. & Mittereder, J. Metallization options and annealing temperatures for low contact resistance ohmic contacts to n-type GaSb. *Solid-State Electron.* **46**, 1627–1631 (2002).